



Real-time Ultra Short Horizon extension MPC for the control of a Formula Student Drive

Israel Melo Sother

Thesis to obtain the Master of Science Degree in
Electrical and Computer Engineering

Supervisor(s): Prof. Sónia Maria Nunes dos Santos Paulo Ferreira Pinto
Egn. Pedro Miguel Batista de Sousa Correia da Costa

Examination Committee

Chairperson: Prof. Célia Maria Santos Cardoso de Jesus
Supervisor: Prof. Sónia Maria Nunes dos Santos Paulo Ferreira Pinto
Member of the Committee: Prof. Miguel Cabral Ferreira Chaves

May 2024

Dedicated to my family.

Declaration

I declare that this document is an original work of my own authorship and that it fulfills all the requirements of the Code of Conduct and Good Practices of the Universidade de Lisboa.

Acknowledgments

First and foremost, I would like to express my gratitude to my supervisors, Prof. Sónia Pinto and Eng. Pedro Costa. I am extremely grateful to Prof. Sónia for her constant support and belief in me. She graciously accepted to supervise me under unusual academic circumstances, navigating the complexities of my double degree program with its confusing regulations. Words cannot express my gratitude to Eng. Pedro Costa, our numerous discussions went beyond academic mentoring; he not only introduced me to new concepts and directed my research but also provided crucial advice on balancing the transition out of the Formula Student life. I am deeply thankful for his technical expertise and the personal sacrifices he made to continue mentoring me.

Special thanks to Guilherme and Sergio for welcoming me to their day-to-day work in the office and for the countless hours spent discussing diverse topics.

I would like to express my heartfelt gratitude to my friends for their support throughout my work. They endured my constant focus on my research with steadfast companionship and encouragement, helping me remember the importance of setting aside time to clear my head, which was invaluable during this journey. Thanks also to Nuti and Mística for introducing me to the Formula Student world and to my group of friends from USP — Major, Comum, Y, and Soja — for all the moments together. Thank you for sharing with me some of the best years of my life.

To the FST11 and FST12 teams, your passionate dedication, tireless efforts, and countless late-night shifts were exhilarating. Together, we conquered numerous challenges and celebrated historic victories. It was an absolute pleasure to work side by side with some of the best engineers I have ever known. The memories we created together will always hold a special place in my heart and serve as a source of inspiration throughout my journey. I would like to extend my sincere thanks to a few members who became my closest friends during this period, Bruno, Duarte, Zé, Pedro, and Luis, your partnership and willingness to entertain all the crazy ideas we discussed were heartwarming, you made me feel welcome in a foreign country. Thank you all for making these years an unforgettable and extraordinary experience.

Lastly, I would be remiss in not mentioning my deepest gratitude to my family for their unwavering support and the sacrifices they made to enable me to study abroad. Choosing to pursue my education here meant greater physical distance between us, and I missed them every moment. I also want to acknowledge their understanding and patience during my Formula Student years, knowing that I dedicated far less time to them than I should have. Despite this, they supported me and embraced my passion for those cars, recognizing the lost time as an investment in something I love, and in turn, they learned to love it too. A special thank you to my sister, who consistently checked in on me and cared for my well-being, providing the much-needed boost when the days and nights of work blended into one. To my parents, thank you for being my role models and for always encouraging me to pursue my dreams wherever they led. Completing this degree is a testament to the values and education you instilled in me.

None of this would be possible without these incredible people. I am fortunate to have had their support and encouragement throughout my dissertation journey, and for that, I am deeply grateful.

Resumo

Este trabalho apresenta o desenvolvimento de uma estratégia de controlo para os motores da Equipe de Fórmula Estudantil do Instituto Superior Técnico. A estratégia de controlo foi desenvolvida para melhorar a resposta dinâmica do torque do motor e a eficiência do sistema. O motor foi caracterizado experimentalmente e um ambiente de simulação foi criado para testar diferentes estratégias de controlo. O MPC explícito foi selecionado como a estratégia mais adequada devido à sua resposta rápida e baixa variação de corrente. Uma nova técnica de extensão de horizonte foi proposta para reduzir os erros na previsão, o que deu nome ao controlador: Real-time Ultra Short Horizon extension MPC (RUSH MPC). A estratégia de controlo foi implementada numa FPGA e foi desenvolvida uma bancada de testes. Os resultados experimentais mostraram uma correspondência próxima com os resultados da simulação, validando a estimativa de torque, as medições de corrente e a estratégia de controlo. A eficiência do sistema foi melhorada devido à redução na THD de corrente e a resposta de torque foi melhorada em ordens de magnitude em comparação com a solução atual.

Palavras-chave: MPC Explícito, Controlo de Motores, Veículos Elétricos, Fórmula Estudantil, Extensão de Horizonte

Abstract

This work presents the development of a control strategy for the motors of the Formula Student Team of Instituto Superior Técnico. The control strategy was developed with the main goal of improving the dynamic response of the motor torque and the system efficiency. The motor was experimentally characterized and a simulation environment was created to test different control strategies. The explicit MPC was selected as the most suitable strategy due to its fast response and low current ripple. A novel horizon extension technique was proposed to reduce model mismatch, which gave the name of the controller: Real-time Ultra Short Horizon extension MPC (RUSH MPC). The control strategy was implemented in an FPGA and a test bench setup was developed. The experimental results showed a close match with the simulation results, validating the torque estimation, the current measurements, and the control strategy. The system efficiency was improved due to the reduction in current THD and the torque response was improved by orders of magnitude compared to the current solution.

Keywords: Explicit MPC, Motor Control, Electric Vehicle, Formula Student, Horizon Extension

Contents

Acknowledgments	iv
Resumo	v
Abstract	vi
List of Tables	x
List of Figures	xi
Nomenclature	xiii
Glossary	xv
1 Introduction	1
1.1 Motivation	1
1.2 Control Methods Overview	2
1.3 Thesis Objectives	3
1.4 Thesis Outline	3
2 Theoretical Background and PMSM Model	5
2.1 Formula Student	5
2.2 Two Level Voltage Source Inverter	8
2.2.1 Space Vector Modulation	9
2.3 PMSM model	11
2.3.1 PMSM in ABC coordinates	11
2.3.2 dq0 Transformation	13
2.3.3 PMSM in dq0 coordinates	14
2.3.4 Discretization of the PMSM model	16
2.4 Control Methods State of the Art	18
2.4.1 Field Oriented Control	18
2.4.2 Direct Torque Control	19
2.4.3 Model Predictive Control	20
3 Machine Characterization and Control Methodology	21
3.1 Motor characterization	21
3.1.1 Phase resistance	22
3.1.2 Flux Linkage	22

3.1.3	Machine direct and quadrature inductances	23
3.1.3.1	Method 1	23
3.1.3.2	Method 2	26
3.2	Current References	30
3.2.1	Constraints with limited input voltage	31
3.2.2	Inductance Curves	34
3.3	Load profile	35
3.4	Control Methods Development	36
3.4.1	Finite Set MPC	37
3.4.2	Finite Set with Null Vector MPC	37
3.4.3	Non-Linear Continuous Set MPC	38
3.4.4	RUSH MPC	38
3.4.4.1	Horizon Extension	40
3.4.4.2	Speed Control	41
4	Simulation and Experimental Results	45
4.1	Simulation	45
4.1.1	Baseline Step	46
4.1.2	Current THD	48
4.1.3	Robustness	49
4.1.4	Acceleration Event	50
4.2	Experimental Results	51
5	Conclusions	59
5.1	Achievements	60
5.2	Future Work	60
Bibliography		62
A Amplitude invariant dq0 PMSM model		66
B Technical Datasheets		67
B.1	AMK Motor Datasheet	68
B.2	AMK Inverter Datasheet	70
C Current Reference using characterized inductances		71
D Inverter Design		73
D.1	Efficiency Equation Formulation	73
D.1.1	Motor and Controller parameters	74
D.2	Operation Points	75
D.3	Diode Selection	76

D.4	MOSFET Module Selection	77
D.5	Gate Driver Design	79
D.6	Current and Voltage Measurement	81
D.7	PCB Design	81
D.8	Inverter Schematics and Layers	83
D.8.1	Half Bridge Board Schematic	84
D.8.2	Half Bridge Board Layers	85
D.8.3	Gate Driver Board Schematic	86
D.8.4	Gate Driver Board Layers	95
D.8.5	Current Sensor Board Schematic	96
D.8.6	Current Sensor Board Layers	101
D.8.6.1	Top Layer	101
D.8.6.2	Bottom Layer	101

List of Tables

2.1	FST13 Powertrain Specifications	7
2.2	Switching combinations and space vectors for a 2-level three-phase inverter	8
4.1	Simulation Parameters	46
4.2	Control Method Current THD comparison. THD is calculated until the Nyquist frequency, that is 250kHz and 40kHz for the controllers running at 50kHz and 8kHz respectively. . .	48
D.1	List of possible diodes for the new inverter design compared to the solution used on the current design.	77
D.2	List of possible MOSFET modules for the new inverter design compared to the discrete solution used on the current design.	78
D.3	Efficiency comparison of the possible MOSFETs modules for the new inverter design. . .	78

List of Figures

1.1 FST12 Team at Formula Student Germany Competition.	2
2.1 Formula Student Germany Tracks.	6
2.2 2-Level Voltage source Inverter arrangement.	8
2.3 Space vector for a 2-level three-phase inverter.	9
2.4 Delta-wound PMSM.	12
2.5 Field Oriented Control - from Texas Instruments [27].	18
2.6 Direct Torque Control - from El Ouanjli et al. [33].	19
3.1 Flux Linkage characterization.	23
3.2 Inductance measurement setup schematic.	23
3.3 Inductance measurement setup.	24
3.4 Inductance measurement oscilloscope output.	25
3.5 L_d in function of i_d	25
3.6 Quadrature Inductance measurement alignment pulse setup.	26
3.7 L_q in function of i_q	26
3.8 Identification voltage pulses - from Stumberger et al. [40].	27
3.9 Quadrature Flux linkage @ $i_d = -5A$	28
3.10 Flux linkage with different currents on a perpendicular axis.	28
3.11 Flux Linkage exponential fit.	29
3.12 Maximum Torque per Ampere curve without constraints.	32
3.13 Constrained Maximum Torque per Ampere curve at minimum, nominal, and maximum voltages. Reference currents are shown for 0, 13000 and 2000 RPMs.	33
3.14 Manufacturer inductance curves.	35
3.15 FSMPc Diagram.	37
3.16 Finite Set with Null Vector MPC Diagram.	38
3.17 Implicit Continuous Set MPC Diagram.	39
3.18 Explicit Continuous Set MPC Diagram.	39
3.19 Horizon extension by one timestep.	40
3.20 Horizon Extension by control time.	41

3.21 Horizon extension comparison, on top the measured and predicted voltages. The bottom lines are the computed control action and the applied control action	41
3.22 Speed control diagram.	42
3.23 Root locus plot for the closed loop system.	44
4.1 Simulink Models, Motor and Inverter.	46
4.2 Control methods comparison in a torque step.	47
4.3 Monte Carlo Robustness Analysis.	49
4.4 Parameter correlation coefficient with performance metrics.	50
4.5 Control methods comparison on an Acceleration event.	51
4.6 Testbench setup.	52
4.7 Torque estimation vs Measured. In the bottom the percentual error between the measured and estimated torques is shown.	53
4.8 Line currents measurements at steady state. Torque reference at $7Nm$ and rotor speed stable at $169RPMs$	53
4.9 Line Current measurements with a reference torque step from 0 to $7Nm$ at $0.02s$	54
4.10 Torque reference following with a step from 0 to $7Nm$	55
4.11 Comparison of torque step response between the proposed method and the currently implemented method.	55
4.12 Torque step response for different reference torque values.	56
4.13 RPM step from standstill to $2500RPMs$	57
4.14 Pedal torque profile.	58
C.1 Constrained Maximum Torque per Ampere curve at minimum, nominal, and maximum voltages. Reference currents are shown for 0, 13000 and 2000 RPMs.	72
D.1 Motor power factor and current THD maps as a function of the motor speed and torque. .	74
D.2 Motor operation points for the 2023 Germany Endurance Event. The color represents the number of points in each bin on a logarithmic scale.	75
D.3 Combined motor operation points for the 2023 Germany Endurance Event. The color represents the number of points in each bin on a logarithmic scale.	76
D.4 Render of the PCBs used in the new inverter design.	79
D.5 Desaturation protection circuit (adapted from [5]).	80
D.6 Render of the PCBs used in the new inverter design.	82
D.7 Render of the final leg module.	83
D.8 Half Bridge Board Layers.	85
D.9 Gate Driver Board Layers.	95

Nomenclature

Greek symbols

η	Efficiency
λ	Lagrange Multiplier
ω	Rotor velocity
ω_{wheels}	Wheel rotational velocity
ω_e	Rotor electrical velocity
ψ_x	Flux linkage
ρ	Air density
τ	Time Constant
θ	Rotor position
θ_e	Rotor electrical position

Roman symbols

A_r	Car frontal reference area
C_d	Drag coefficient
C_r	Rolling resistance coefficient
\mathcal{C}_{soft}	MPC soft constraint
E_x	Back EMF
G_r	Transmission Gear Ratio
h	Sampling time
i_x	Current
\mathcal{J}	MPC cost function
J	Rotational Inertia

k	Discrete time index
k_i	PI integral gain
k_p	PI proportional gain
K_t	Torque Constant
K_v	Voltage Constant
L_x	Phase self inductance
m	Modulation index
M_{xy}	Phase mutual inductance
m_{car}	Car mass
p	Number of pole pairs
r_x	Phase resistance
r_{tire}	Tire radius
s_x	MPC cost gains
T_e	Electromagnetic torque
T_{load}	Load reaction torque
T_{loss}	Losses equivalent torque
u_x	Voltage
v	Car Velocity
V_{ref}	Voltage reference vector

Subscripts

$d, q, 0$	Direct axis, quadrature axis, and zero-sequence components
f, r	Front and Rear axle
A, B, C	Line values
a, b, c	Phase values
PM	Permanent Magnet component

Superscripts

\cdot	Time derivative
T	Transpose

Chapter 1

Introduction

Contents

1.1 Motivation	1
1.2 Control Methods Overview	2
1.3 Thesis Objectives	3
1.4 Thesis Outline	3

1.1 Motivation

With the increasing regulation efforts to reduce carbon footprints, an upward trend of investments in the mobility sector for the development of electric and hybrid powertrains has emerged. This field has received considerable interest for not only hardware improvements [1] but also new software alternatives with several new control strategies being proposed. From one side the advancing processing power available in microcontrollers has enabled the use of real-time predictive control strategies [2], while the use of wide bandgap semiconductors results in a substantial efficiency improvement [3].

Formula Student is an engineering competition that challenges students to design, manufacture, and test a formula-style race car inside a given set of regulations. Similarly to the industry trend, the competition has pushed teams towards electrification, encouraging students to seek solutions that are lightweight, powerful, and efficient. The Formula Student Team of Técnico Lisboa (FST Lisboa) was funded in 2001, and since then has built 12 prototypes, from the fourth model (FST04) onward they have an electric powertrain, with the last 3 having autonomous racing mode, with the last one shown in Figure 1.1.

A major advance in the power converter field was the use of wide bandgap semiconductors, which has allowed the development of more efficient converters with a higher power density. As a relatively new technology, there aren't many off-the-shelf solutions that fulfill the specifications required for a Formula Student prototype, thus some of the top teams started to develop their own motor drive solutions. FST Lisboa started working on a fully self-developed powertrain in 2017 with the motor development by Sarrico [4], and inverter development by Costa [5]. This development aligns with the fundamental

objectives of Formula Student, which is empowering technical and practical knowledge to better prepare students. Additionally, the development of the entire powertrain system can result in a more efficient platform, creating a system optimized for each prototype. Unfortunately, the motor prototype is not ready to be used in the car, and the inverter is missing a system able to control the currently used motors. This work intends to fill a critical gap which is the absence of adequate control for a Permanent Magnet Synchronous Motor (PMSM). By developing and implementing a control strategy that enables the use of an in-house developed inverter with the commercial motor solution, this work not only addresses the identified bottleneck in the powertrain section but also shifts the performance envelope standards, improving the overall capabilities of the next prototypes.

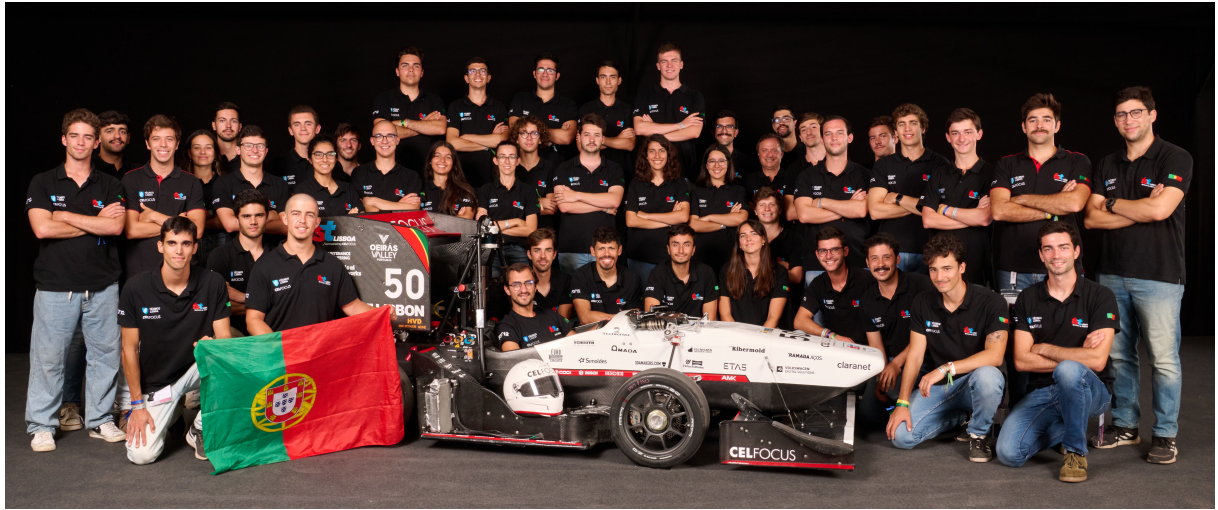


Figure 1.1: FST12 Team at Formula Student Germany Competition, © FSG - Axel Grobe.

1.2 Control Methods Overview

Through the years, several approaches have been proposed to control synchronous machines using a 2-level three-phase inverter. Regarding the control methods, several solutions have been presented in the literature with the most common being Field Oriented Control (FOC) and Direct Torque Control (DTC), with Model Predictive Control (MPC) [6] being introduced more recently, seeking a compromise between the advantages of FOC and DTC. Some approaches require a modulator such as Space Vector Modulation (SVM) [7], while others can directly output the semiconductor trigger signals [8].

The use of FOC and DTC have dominated the market for many years due to their simple implementation, but each of them has downsides. FOC combined with current control PID is known for having a slow dynamic response when compared to DTC, while in steady-state behavior and disturbance rejection, FOC shows better results [9–11]. DTC has a faster dynamic response, with the compromise of a higher torque ripple and a higher current Total Harmonic Distortion (THD). MPC has been proposed as a combination of the two, exhibiting a good dynamic response while being able to maintain low current and torque ripple.

Technical advances in the microprocessor industry have allowed the increasing use of MPC in power

converters and drives [8]. This non-linear control scheme provides easy constraint integration while optimizing the control action in real time and is adaptable to different types of electric machines being controlled. The main downside of this strategy is the increased computational cost, which is offset by the decreased cost of computational power.

MPC in power systems is usually divided in two categories: Continuous Set Model Predictive Control (CS-MPC) and Finite Set Model Predictive Control (FS-MPC) [12], depending on their output signals. The first type calculates the best possible voltage vector and then uses a modulator like SVM to compose it, while FS-MPC exploits the fact that a motor drive usually has a limited number of possible voltage combinations and thus predicts the currents for each of those vectors to evaluate the best option. The second approach usually doesn't need a modulator as it only considers the finite set of all possible converter states, although some variations have tried to increase the search space by introducing synthetic vectors that are created from a combination of the native ones. This technique of subdivision and refining vectors can be used to create a quasi-continuous set MPC [13], which, when combined with reducing the search area to the most probable sector, can improve the torque and current ripple without a prohibitive increase in computational cost.

1.3 Thesis Objectives

This work targets to develop a nonlinear control strategy that allows the use of the existing high-efficiency inverter [5] with the commercial motors currently used by the team [14]. This control method must be able to achieve a faster dynamic response than the current inverter used by the team while maintaining or improving the same steady-state performance, and with a sampling time smaller than 20 μ s to allow a switching frequency of at least 50kHz.

While the improved control method will enhance the performance, not all the gains will come from that, but also the use of an inverter with Silicon Carbide (SiC) mosfets greatly increases the efficiency. The increase in switching frequency shall bring a reduction in the currents THD resulting in further efficiency improvements. Lastly, the use of an inverter designed specifically for this motor will reduce the system mass, improving the power-to-weight ratio.

Summing up, this work aims to increase the dynamic response and the efficiency of the powertrain system using wide bandgap semiconductors and nonlinear control methods. This will be verified in simulations, and wherever possible with a prototype in a test bench, where the control method shall be compared with the Original Equipment Manufacturer (OEM) system. A revised version of the inverter will also be made, to improve the measurement robustness to Electromagnetic Interference (EMI) and to increase the maximum current limit of the semiconductors to match the motor's maximum current.

1.4 Thesis Outline

Chapter 2 starts with an overview of formula student competitions, followed by an introduction to two-level inverters. Then a mathematical model for a PMSM is developed, laying the ground for the proposal

of the control methods. The chapter ends with a brief review of the control methods state of the art.

In Chapter 3 the motor characterization methodology is defined and the current reference generation is presented. A load profile that represents the car is also defined, and the controllers studied in this work are proposed.

Chapter 4 presents simulations comparing the control methods and validation of the simulation model with experimental tests.

In Chapter 5 the conclusions are made, analyzing which objectives were fulfilled and proposing topics for future research.

Chapter 2

Theoretical Background and PMSM Model

Contents

2.1 Formula Student	5
2.2 Two Level Voltage Source Inverter	8
2.2.1 Space Vector Modulation	9
2.3 PMSM model	11
2.3.1 PMSM in ABC coordinates	11
2.3.2 d _q 0 Transformation	13
2.3.3 PMSM in d _q 0 coordinates	14
2.3.4 Discretization of the PMSM model	16
2.4 Control Methods State of the Art	18
2.4.1 Field Oriented Control	18
2.4.2 Direct Torque Control	19
2.4.3 Model Predictive Control	20

This chapter covers some fundamentals used to develop this work. It starts with a brief overview of Formula Student competitions and the current powertrain system used by FST Lisboa. After this, it presents the basics on Voltage Source Inverter (VSI) and modulation techniques before developing a mathematical model for the used motors and later converting it to discrete time. Lastly, a quick overview of the literature control methods is done before introducing the proposed strategy.

2.1 Formula Student

In a formula student competition, two types of evaluation exist, the first category is comprised of static events where the design, cost, and business model of the prototype are analyzed. In the dynamic category, each prototype is evaluated through 5 different events: Skidpad, Acceleration, AutoX, Endurance,

and Efficiency (evaluated in the Endurance track), as shown in figure Figure 2.1. To be able to compete in dynamic events each prototype needs to pass a series of safety and rule compliance inspections, a process which starts even before competition with the documentation analysis and finishes with on-site scrutineering.

The Skidpad event is the least relevant for this study as it is designed to test the cornering ability of the vehicle. It is comprised of two circles of radius 9.125m, where the vehicle performs an adaptation first lap and then the lap time is measured on the second lap, when the car is at steady state cornering. As it is a tight and steady course, the power consumption is low not reaching the regulations limit of 80kW, thus the dynamic response and efficiency of the motors have almost no relevance to the performance.

The acceleration event consists of a standing start 75m straight acceleration, with the maximum battery power limited to 80kw, as it is for all Formula Student events. For this event, the key factors from a powertrain point of view are the torque dynamic response, and how efficiently the powertrain system can deliver power to the ground. The AutoX is a 1km track with several corners and straights mixed.

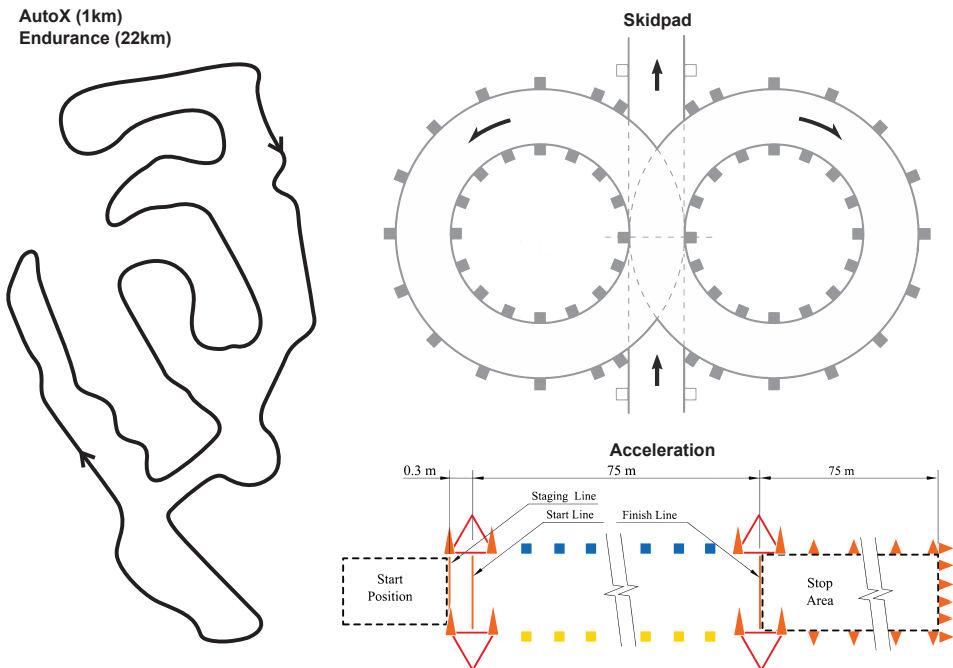


Figure 2.1: Formula Student Germany Tracks, adapted from [15].

In this test, an increased dynamic response can delay the braking zone, and the efficiency allows it to reach higher velocities using the same amount of power. Lastly, the endurance event is similar to the AutoX, with enough laps to complete 22km. In this event, although improved dynamics can be beneficial, efficiency is the key factor as it results in more available energy to complete the 22km track while also scoring points in the Efficiency category.

For the autonomous part of the competition, there are very similar events, with the Skidpad and Acceleration being the same as in the manual mode. The driverless AutoX needs to be a little different, with a smaller distance for the Autonomous System Responsible (ASR) to be able to see the car throughout the entire track and press the emergency button if necessary. The Endurance event driver-

less analogous is the TrackDrive event, usually being on the same track as the AutoX, but with fixed 10 laps. Currently, the points performance in the driverless events is mostly dictated by how good the autonomous software is, but as the teams evolve, the cars will play a major role in the results, the same way as it is in the manual category.

Since the FST07, FST Lisboa has used AMK motors and inverters [14, 16] (datasheets shown in Appendix B), this set is a good solution for teams switching to a four-motor setup as it is already paired and has good documentation. However, as the team evolves, it is natural to look for improvements, and the AMK inverters were deemed one of the prototypes' current bottlenecks. The use of Insulated-Gate Bipolar Transistor (IGBT) as the switching component, means that this inverter is capped in its switching frequency, using only 8kHz. This low switching frequency reduces powertrain efficiency and increases the set's weight. Another drawback of this solution is the control method as it uses a simple FOC, thus having a low dynamic response and further reducing efficiency by not using Maximum Torque per Ampere (MTPA) strategies. A brief outline of the current specification of FST Lisboa's prototype is shown in Table 2.1.

Table 2.1: FST13 Powertrain Specifications

Parameter	Value
Battery Voltage Min	420 V
Battery Voltage Maximum	609 V (limited at 600 V by regulations)
Battery Voltage Nominal	532 V
Maximum Power	147 kW (limited at 80 kW by regulations)
Number of Motors	4
Maximum Power per Motor	36.75 kW
Typical Average Power	30 kW
Maximum Average Power (1 min)	60 kW
Maximum Current DC	160 A
Maximum motor current RMS (1,24s)	105 A
AMK Inverter Switching Frequency	8 kHz
Rotating magnetic field at Maximum Speed	1.6 kHz
Rated Motor Current	41 Arms
Rated Motor Voltage	350 V
Maximum Speed	20000 RPM
Motor Number of Poles	10
Quadrature Axis Inductance,	0.12 mH
Direct Axis Inductance	0.24 mH
Rotor time constant	0.01 s
Maximum Torque	21 Nm
Torque constant	0.26 Nm/Arms
Voltage constant	18.8 V/kRPM

2.2 Two Level Voltage Source Inverter

The usual hardware used to control synchronous machines is a 2-level Voltage Source Inverter. Such equipment is composed of six switches organized in three legs, where each pair of switches is connected to a motor terminal, as shown in Figure 2.2.

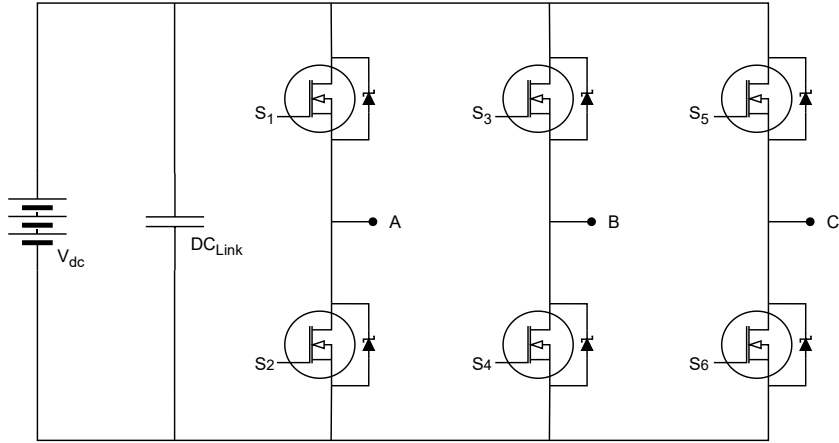


Figure 2.2: 2-Level Voltage source Inverter arrangement.

Usually, each switch in an inverter leg is operated with the inverse logic of the other switch in the leg, and this arrangement allows for 8 different switching combinations where 2 of them result in null voltages. That gives 7 possible voltage vectors, as detailed in Table 2.2 and Figure 2.3. In Table 2.2 the Vector column denotes the top switches states (S_1, S_2 , and S_3), where a 1 means the top switch is the conducting state with the bottom switch is on a cut-off state and a 0 the opposite. The α and β components which define the state space vectors are as defined by the Concordia transformation, shown in Equation (2.1).

$$Co = \sqrt{\frac{2}{3}} \begin{bmatrix} 1 & 0 & \frac{1}{\sqrt{2}} \\ -\frac{1}{2} & \frac{\sqrt{3}}{2} & \frac{1}{\sqrt{2}} \\ -\frac{1}{2} & -\frac{\sqrt{3}}{2} & \frac{1}{\sqrt{2}} \end{bmatrix} \quad (2.1)$$

Table 2.2: Switching combinations and space vectors for a 2-level three-phase inverter

Switch State	Vector	V_{AB}	V_{BC}	V_{CA}	V_α	V_β
0	000	0	0	0	0	0
1	001	V_{DC}	0	$-V_{DC}$	$\sqrt{\frac{2}{3}}V_{DC}$	0
2	010	$-V_{DC}$	V_{DC}	0	$\frac{1}{\sqrt{6}}V_{DC}$	$\frac{1}{\sqrt{2}}V_{DC}$
3	011	0	V_{DC}	$-V_{DC}$	$-\frac{1}{\sqrt{6}}V_{DC}$	$\frac{1}{\sqrt{2}}V_{DC}$
4	100	0	$-V_{DC}$	V_{DC}	$-\sqrt{\frac{2}{3}}V_{DC}$	0
5	101	V_{DC}	$-V_{DC}$	0	$-\frac{1}{\sqrt{6}}V_{DC}$	$\frac{1}{\sqrt{2}}V_{DC}$
6	110	$-V_{DC}$	0	V_{DC}	$\frac{1}{\sqrt{6}}V_{DC}$	$\frac{1}{\sqrt{2}}V_{DC}$
7	111	0	0	0	0	0

Despite the number of discrete voltage states, using some modulation techniques it is possible to synthesize a resultant vector if it is inside the attainable region denoted by the hexagon in Figure 2.3.

The current inverter used by FST Lisboa uses this structure, but the switches are silicon IGBTs, which when compared to SiC MOSFETs has a higher switching loss, leading to lower switching frequencies being used [17]. The lower switching frequencies cause higher distortions in the current waveforms, decreasing motor efficiency. The lower switching frequency system also needs a higher capacitance on the DC Link, while the lower efficiency of silicon semiconductors requires a bigger heatsink, leading to a higher volume and mass inverter, decreasing the power density of the solution.

2.2.1 Space Vector Modulation

Several modulation techniques have been proposed in the literature like Sinusoidal Pulse-Width Modulation (SPWM), Selective Harmonic Elimination (SHE) [18], SVM [7]. The most common method of modulation in digital motor control is SVM, as it is a robust, easy-to-implement technique, and allows higher voltage ratio.

Figure 2.3 shows a 2D representation of the space vector for a 2-level three-phase inverter. The basic voltage vectors (previously defined on Table 2.2) are shown pointing to the hexagon corners. Connecting the basic vectors produces the hexagon of possible voltage states.

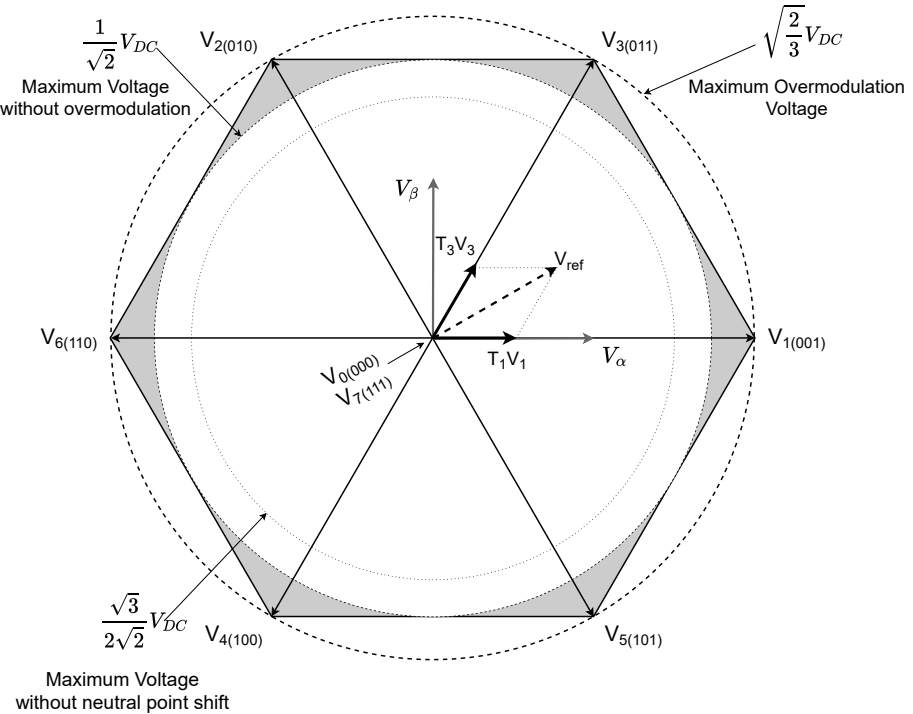


Figure 2.3: Space vector for a 2-level three-phase inverter.

Using SVM it is possible to modulate any vector inside the hexagon shown in Figure 2.3, but if a pure sinusoidal output is desired, the vectors should be constrained to the inscribed circle, that has a radius of $\frac{1}{\sqrt{2}} V_{DC}$. The reason behind this is to keep the reference vector locus inside the hexagon, avoiding distortions in the output. Note that although it is possible to generate waveforms with higher RMS value, it is not possible to modulate a peak higher than $\frac{1}{\sqrt{2}} V_{DC}$ for every vector angle. If a higher

RMS value is requested the generated voltage will be saturated on the sides of the hexagon while near the corners it will achieve the requested value, thus those waveforms become more and more distorted as the amplitude approaches $\sqrt{\frac{2}{3}}V_{DC}$. To modulate a sinusoidal output the vector should develop a circular trajectory, but in the overmodulation region the voltage constrains it to the voltage hexagon, and thus the difference between the intended and the effectively applied vector increases.

To simplify the analysis of those vectors, a modulation index (m) is defined as shown in Equation (2.2). The output is free of distortion if $m \leq \frac{2}{\sqrt{3}}$, and increasing the modulation index further will result in diminishing returns in wave amplitude, while the output approaches a six-step commutation, greatly increasing the THD [19]. This area of operation is called overmodulation, and several approaches have been proposed [20, 21] to minimize the distortions.

$$m = \frac{2\sqrt{2}}{\sqrt{3}} \frac{|V_{ref}|}{V_{DC}} \quad m \in \left[0, \frac{4}{3}\right] \quad (2.2)$$

To modulate a voltage vector that is not exactly one of the basic voltage vectors a modulation technique is needed. When using the SVM method to compose a given reference vector V_{ref} , the algorithm first detects the sector on which the reference vector lays. With the sector identified a ratio between the adjacent basic vectors and a null vector is selected so that the average vector is equal to the reference vector. This ratio is calculated as shown in Equation (2.3).

For example, let's consider the reference vector shown in Figure 2.3. According to SVM, this vector can be modulated by using V_1 for half of the active time and V_3 for the other half of the active time. The active time refers to the duration when the vector amplitude is non-zero, while the null time refers to the duration when a null vector is used to reduce the output amplitude. This modulation can be expressed by Equation (2.3), where $T_1 + T_3$ represents the active time and T_{null} represents the null time.

$$V_{ref} = \frac{T_{null}V_{null} + T_1V_1 + T_3V_3}{h} \quad (2.3)$$

In the hardware implementation, the voltage reference is generated in the rotor reference frame (dq0) and then the inverse dq0 transformation is applied to obtain the phase voltages directly, without selecting a sector to know which vectors to use. These phase voltages are then divided by the DC link voltage to obtain the duty cycle of the switches. Note that this does not account though for the neutral point shift. This simplification results in the same switching times for the active vectors as the geometric approach of calculating which sector the reference vector is and then decomposing the reference vector in the two adjacent vectors. The null vector distribution between V_0 and V_7 will dictate the neutral point shifting method.

Several approaches have been proposed to accomplish this shift and they all rely on injecting a variable offset voltage on the neutral point that has a strong third harmonic component. Although a pure third harmonic sine wave can be used it is computationally expensive when compared with other methods such as top, mid, or bottom clamp. This technique of mid-clamp aims to center the neutral point between the DC link terminals, while the top clamp shifts the neutral point to the maximum voltage and the bottom clamp to the minimum voltage. The main advantage of a top or bottom clamp is the reduced

number of switching events when compared with a mid-clamp.

The chosen approach is defined by Equation (2.4), where K_{shift} is the shift factor, and V_{AN}, V_{BN} , and V_{CN} are the phase voltages referenced to a virtual neutral point that is the average of the phase voltages with respect to the DC link negative terminal. The value of K_{shift} dictates the shift method used, when it is equal to 1 the top-clamp method is used, if it is 0.5 then the mid-clamp is used, and 0 results in the bottom-clamp method. Microchip [22] has a visualization tool with the main methods shown. The calculated shift voltage is then summed to the desired phase voltages, and the modulation technique is applied as usual. In the implementation, this results in the MOSFETs duty cycle being shifted to center at the value of K_{shift} .

$$V_{shift} = K_{shift} - K_{shift} \max(V_{AN}, V_{BN}, V_{CN}) - (1 - K_{shift}) \min(V_{AN}, V_{BN}, V_{CN}) \quad (2.4)$$

2.3 PMSM model

As the proposed work is to improve the dynamic response and efficiency of the motor and motor drive currently used by FST Lisboa, it is necessary to first develop a model to represent this machine, a PMSM with delta-arranged windings.

2.3.1 PMSM in ABC coordinates

The stator voltages of the considered electrical machine can be given by Equation (2.5), with a graphical representation in Figure 2.4.

$$\begin{bmatrix} u_{AB} \\ u_{BC} \\ u_{CA} \end{bmatrix} = \begin{bmatrix} r_a & 0 & 0 \\ 0 & r_b & 0 \\ 0 & 0 & r_c \end{bmatrix} \begin{bmatrix} i_a \\ i_b \\ i_c \end{bmatrix} + \frac{d}{dt} \begin{bmatrix} \psi_a \\ \psi_b \\ \psi_c \end{bmatrix} \quad (2.5)$$

In this equation, u_{xy} represents the measured voltage between terminal x and y , i_x is the current flowing on each phase, r_x is the phase resistance, and ψ_x is the flux linkage of each coil. Combining this in a matrix representation we can define the variables in Equation (2.6).

$$\mathbf{R}_{abc} = \begin{bmatrix} r_a & 0 & 0 \\ 0 & r_b & 0 \\ 0 & 0 & r_c \end{bmatrix} \quad (2.6a) \quad \mathbf{i}_{abc} = \begin{bmatrix} i_a \\ i_b \\ i_c \end{bmatrix} \quad (2.6b) \quad \mathbf{u}_{abc} = \begin{bmatrix} u_{AB} \\ u_{BC} \\ u_{CA} \end{bmatrix} \quad (2.6c)$$

Regarding the flux linkage, it can be defined as in Equation (2.7a), where ψ_{PM} is the permanent magnet flux linkage, and θ_e is the rotor electrical position. Additionally, the L_{abc} matrix is the inductance matrix as later defined in Equation (2.9). With this definition, the Equation (2.5) can be expanded into Equation (2.8), where E_x is the back EMF as defined in Equation (2.7b).

$$\psi_{abc} = \mathbf{L}_{abc} \mathbf{i}_{abc} + \psi_{PM} \begin{bmatrix} \cos(\theta_e) \\ \cos(\theta_e - \frac{4\pi}{3}) \\ \cos(\theta_e + \frac{4\pi}{3}) \end{bmatrix} \quad (2.7a)$$

$$\mathbf{E}_{abc} = \begin{bmatrix} E_a \\ E_b \\ E_c \end{bmatrix} = \psi_{PM} \dot{\theta}_e \begin{bmatrix} -\sin(\theta_e) \\ -\sin(\theta_e - \frac{4\pi}{3}) \\ -\sin(\theta_e + \frac{4\pi}{3}) \end{bmatrix} \quad (2.7b)$$

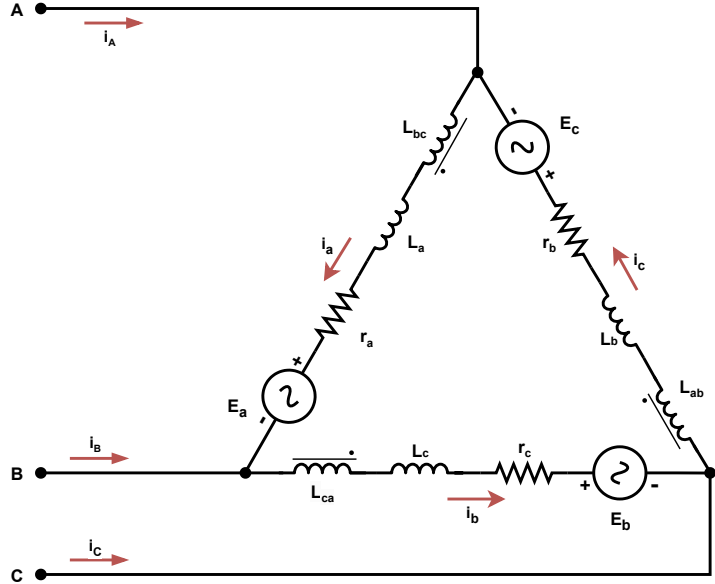


Figure 2.4: Delta-wound PMSM

The expanded form results in Equation (2.8).

$$\mathbf{u}_{abc} = \mathbf{R}_{abc} \mathbf{i}_{abc} + \mathbf{L}_{abc} \frac{d\mathbf{i}_{abc}}{dt} + \frac{d\mathbf{L}_{abc}}{dt} \mathbf{i}_{abc} + \mathbf{E}_{abc} \quad (2.8)$$

Note that the inductances are not constant, but they change regarding the rotor electrical position θ_e . This variation exists because the selected machine has a spoke magnet arrangement on the rotor, thus creating magnetic paths with different reluctances depending on the rotor angle. According to Marques [23], this variation is a sum of even harmonics of a cosine function, but usually, it is enough to consider up to the second one, resulting in the inductance matrix shown in Equation (2.9), where $L_{x_1}, L_{x_2}, M_{xy_1}$, and M_{xy_2} are constants and define the coefficients for the self inductances and the mutual inductances.

$$\mathbf{L}_{abc} = \begin{bmatrix} L_{a_1} + L_{a_2} \cos(2\theta_e) & M_{ab_1} + M_{ab_2} \cos(2\theta_e + \frac{4\pi}{3}) & M_{ac_1} + M_{ac_2} \cos(2\theta_e - \frac{4\pi}{3}) \\ M_{ba_1} + M_{ba_2} \cos(2\theta_e + \frac{4\pi}{3}) & L_{b_1} + L_{b_2} \cos(2\theta_e - \frac{4\pi}{3}) & M_{bc_1} + M_{bc_2} \cos(2\theta_e) \\ M_{ca_1} + M_{ca_2} \cos(2\theta_e - \frac{4\pi}{3}) & M_{cb_1} + M_{cb_2} \cos(2\theta_e) & L_{c_1} + L_{c_2} \cos(2\theta_e + \frac{4\pi}{3}) \end{bmatrix} \quad (2.9)$$

Is important to explain that the Equation (2.9) is derived assuming the 3 phases are separated by 120 electrical degrees and that the windings have a sinusoidal magnetomotive force distribution.

For comprehensive understanding, the self inductances L_x and the mutual inductances L_{xy} depicted in Figure 2.4 are as defined in Equation (2.10).

$$L_{ab} = M_{ab_1} + M_{ab_2} \cos\left(2\theta_e + \frac{4\pi}{3}\right) \quad (2.10a) \quad L_{ac} = M_{ac_1} + M_{ac_2} \cos\left(2\theta_e - \frac{4\pi}{3}\right) \quad (2.10b)$$

$$L_{ba} = M_{ba_1} + M_{ba_2} \cos\left(2\theta_e + \frac{4\pi}{3}\right) \quad (2.10c) \quad L_{bc} = M_{bc_1} + M_{bc_2} \cos(2\theta_e) \quad (2.10d)$$

$$L_{ca} = M_{ca_1} + M_{ca_2} \cos\left(2\theta_e - \frac{4\pi}{3}\right) \quad (2.10e) \quad L_{cb} = M_{cb_1} + M_{cb_2} \cos(2\theta_e) \quad (2.10f)$$

$$L_a = L_{a_1} + L_{a_2} \cos(2\theta_e) \quad (2.10g) \quad L_b = L_{b_1} + L_{b_2} \cos(2\theta_e) \quad (2.10h)$$

$$L_c = L_{c_1} + L_{c_2} \cos(2\theta_e) \quad (2.10i)$$

2.3.2 dq0 Transformation

To simplify the mathematical models, some transformations were proposed. The most common is the dq0 transformation, which is a combination of the Concordia and the Blondel-Park transformations. The Concordia transformation converts a three-phase system into an equivalent two-phase system, where the two phases are orthogonal to each other, they are called α and β components. This transformation has two main versions, the amplitude invariant, and the power invariant. The power invariant version, initially presented in Equation (2.1), is shown again in Equation (2.11a) for easier reference.

The Blondel-Park transformation is a rotating referential transformation, where the referential is synchronous with the rotor position. The transformation matrix is shown in Equation (2.11b). Note that throughout this work the alignment of the transformation is always the d component with the phase a . The dq0 transformation is a combination of the Concordia transformation, and the Park referential change, it produces a biphasic equivalent system with a synchronous rotating referential. The transformation matrix is shown in Equation (2.12).

$$\mathbf{Co} = \sqrt{\frac{2}{3}} \begin{bmatrix} 1 & 0 & \frac{1}{\sqrt{2}} \\ -\frac{1}{2} & \frac{\sqrt{3}}{2} & \frac{1}{\sqrt{2}} \\ -\frac{1}{2} & -\frac{\sqrt{3}}{2} & \frac{1}{\sqrt{2}} \end{bmatrix} \quad (2.11a) \quad \mathbf{Bl}_{(\theta_e)} = \begin{bmatrix} \cos(\theta_e) & -\sin(\theta_e) & 0 \\ \sin(\theta_e) & \cos(\theta_e) & 0 \\ 0 & 0 & 1 \end{bmatrix} \quad (2.11b)$$

$$\mathbf{T}_{(\theta_e)} = \mathbf{Co} \mathbf{Bl}_{(\theta_e)} = \sqrt{\frac{2}{3}} \begin{bmatrix} \cos(\theta_e) & -\sin(\theta_e) & \frac{1}{\sqrt{2}} \\ \cos(\theta_e - \frac{2\pi}{3}) & -\sin(\theta_e - \frac{2\pi}{3}) & \frac{1}{\sqrt{2}} \\ \cos(\theta_e - \frac{4\pi}{3}) & -\sin(\theta_e - \frac{4\pi}{3}) & \frac{1}{\sqrt{2}} \end{bmatrix} \quad (2.12)$$

The power invariant transformation has the advantage of being an orthogonal matrix, thus $\mathbf{T}^{-1} = \mathbf{T}^T$. If the amplitude invariant form is used, as in Equation (2.13), then orthogonality is lost.

$$\mathbf{T}_{(\theta_e)}^* = \begin{bmatrix} \cos(\theta_e) & -\sin(\theta_e) & 1 \\ \cos(\theta_e - \frac{2\pi}{3}) & -\sin(\theta_e - \frac{2\pi}{3}) & 1 \\ \cos(\theta_e - \frac{4\pi}{3}) & -\sin(\theta_e - \frac{4\pi}{3}) & 1 \end{bmatrix} \quad (2.13a)$$

$$\mathbf{T}_{(\theta_e)}^*{}^{-1} = \frac{2}{3} \begin{bmatrix} \cos(\theta_e) & \cos(\theta_e - \frac{2\pi}{3}) & \cos(\theta_e - \frac{4\pi}{3}) \\ -\sin(\theta_e) & -\sin(\theta_e - \frac{2\pi}{3}) & -\sin(\theta_e - \frac{4\pi}{3}) \\ \frac{1}{2} & \frac{1}{2} & \frac{1}{2} \end{bmatrix} \quad (2.13b)$$

Applying the power invariant transformation to the abc variables results in Equation (2.14).

$$\mathbf{R}_{dq0} = \mathbf{T}_{(\theta_e)}^T \mathbf{R}_{abc} \mathbf{T}_{(\theta_e)} \quad (2.14a) \qquad \mathbf{L}_{dq0} = \mathbf{T}_{(\theta_e)}^T \mathbf{L}_{abc} \mathbf{T}_{(\theta_e)} \quad (2.14b)$$

$$\mathbf{i}_{abc} = \mathbf{T}_{(\theta_e)} \mathbf{i}_{dq0} \quad (2.14c) \qquad \mathbf{u}_{dq0} = \mathbf{T}_{(\theta_e)}^T \mathbf{u}_{abc} \quad (2.14d) \qquad \boldsymbol{\psi}_{abc} = \mathbf{T}_{(\theta_e)} \boldsymbol{\psi}_{dq0} \quad (2.14e)$$

2.3.3 PMSM in dq0 coordinates

Assuming the three phases are well balanced and using the dq0 transformation (power invariant form) to transform the model into a two-phase system with a rotating referential, new resistance and inductance matrices can be computed to this new referential. The new matrices are shown in Equation (2.15), with the subscripts $d, q, 0$, denoting the direct axis, the quadrature axis, and the zero-sequence axis, respectively. The transformation of the matrices is detailed in Marques [23].

$$\mathbf{R}_{dq0} = \begin{bmatrix} r_a & 0 & 0 \\ 0 & r_b & 0 \\ 0 & 0 & r_c \end{bmatrix} = \begin{bmatrix} r & 0 & 0 \\ 0 & r & 0 \\ 0 & 0 & r \end{bmatrix} \quad (2.15a) \qquad \mathbf{L}_{dq0} = \begin{bmatrix} L_d & 0 & 0 \\ 0 & L_q & 0 \\ 0 & 0 & L_0 \end{bmatrix} \quad (2.15b)$$

Starting with Equation (2.5) and replacing the currents and flux linkages by their dq0 components results in Equation (2.16).

$$\begin{aligned} \mathbf{u}_{abc} &= \mathbf{R}_{abc} \mathbf{T}_{(\theta_e)} \mathbf{i}_{dq0} + \frac{d(\mathbf{T}_{(\theta_e)} \boldsymbol{\psi}_{dq0})}{dt} \\ &= \mathbf{R}_{abc} \mathbf{T}_{(\theta_e)} \mathbf{i}_{dq0} + \dot{\theta}_e \frac{d\mathbf{T}_{(\theta_e)}}{d\theta_e} \boldsymbol{\psi}_{dq0} + \mathbf{T}_{(\theta_e)} \frac{d\boldsymbol{\psi}_{dq0}}{dt} \end{aligned} \quad (2.16)$$

Replacing $\dot{\theta}_e$ with ω_e , and multiplying $\mathbf{T}_{(\theta_e)}^T$ to the left yields Equation (2.17).

$$\mathbf{u}_{dq0} = \mathbf{R}_{dq0} \mathbf{i}_{dq0} + \mathbf{T}_{(\theta_e)}^T \omega_e \frac{d\mathbf{T}_{(\theta_e)}}{d\theta_e} \boldsymbol{\psi}_{dq0} + \mathbf{T}_{(\theta_e)}^T \mathbf{T}_{(\theta_e)} \frac{d\boldsymbol{\psi}_{dq0}}{dt} \quad (2.17)$$

As the transformation matrix is orthogonal, it can be further simplified, as in Equation (2.18).

$$\mathbf{u}_{dq0} = \mathbf{R}_{dq0} \mathbf{i}_{dq0} + \omega_e \mathbf{T}_{(\theta_e)}^T \frac{d\mathbf{T}_{(\theta_e)}}{d\theta_e} \boldsymbol{\psi}_{dq0} + \frac{d\boldsymbol{\psi}_{dq0}}{dt} \quad (2.18)$$

Lastly, calculate the derivative of the transformation matrix, as in Equations (2.19) and (2.20).

$$\mathbf{T}_{(\theta_e)}^T \frac{d\mathbf{T}_{(\theta_e)}}{d\theta_e} = \frac{2}{3} \begin{bmatrix} \cos(\theta_e) & \cos(\theta_e - \frac{2\pi}{3}) & \cos(\theta_e - \frac{4\pi}{3}) \\ -\sin(\theta_e) & -\sin(\theta_e - \frac{2\pi}{3}) & -\sin(\theta_e - \frac{4\pi}{3}) \\ \frac{1}{\sqrt{2}} & \frac{1}{\sqrt{2}} & \frac{1}{\sqrt{2}} \end{bmatrix} \begin{bmatrix} -\sin(\theta_e) & -\cos(\theta_e) & 0 \\ -\sin(\theta_e - \frac{2\pi}{3}) & -\cos(\theta_e - \frac{2\pi}{3}) & 0 \\ -\sin(\theta_e - \frac{4\pi}{3}) & -\cos(\theta_e - \frac{4\pi}{3}) & 0 \end{bmatrix} \quad (2.19)$$

$$\mathbf{T}_{(\theta_e)}^T \frac{d\mathbf{T}_{(\theta_e)}}{d\theta_e} = \begin{bmatrix} 0 & -1 & 0 \\ 1 & 0 & 0 \\ 0 & 0 & 0 \end{bmatrix} \quad (2.20)$$

Thus, the PMSM model in the dq0 frame is presented in Equation (2.21). This approach can be used for the amplitude invariant transformation and will result in the same form of equation (Appendix A), but the equation will be scaled by a factor of $\sqrt{\frac{3}{2}}$ in the d and q axis, while the zero axis can give different results.

$$\mathbf{u}_{dq0} = \mathbf{R}_{dq0} \mathbf{i}_{dq0} + \omega_e \begin{bmatrix} 0 & -1 & 0 \\ 1 & 0 & 0 \\ 0 & 0 & 0 \end{bmatrix} \boldsymbol{\psi}_{dq0} + \frac{d\boldsymbol{\psi}_{dq0}}{dt} \quad (2.21)$$

Is worth noticing that because this is a delta wound machine, the sum of the phase currents is not necessarily zero, and as such, it is mathematically possible to have a circulating current through the phases [24], thus the zero-sequence component is not directly zero as in a Y wound device. For such currents to exist, an external exciting winding, a relevant non-considered inductance harmonic, or an imbalance through the phases is necessary. Even when those currents are present, they are usually dependent on the rotor position, and cannot be controlled with the standard 3-terminal connection, thus for the sake of simplicity, they are discarded throughout this work, which gives Equation (2.22).

$$u_d = ri_d + \frac{d\psi_d}{dt} - \omega_e \psi_q \quad (2.22a)$$

$$u_q = ri_q + \frac{d\psi_q}{dt} + \omega_e \psi_d \quad (2.22b)$$

$$T_e = p(\psi_d i_q - \psi_q i_d) \quad (2.22c)$$

$$\frac{d\omega_e}{dt} = \frac{T_e - T_{load} - T_{loss}}{J} \quad (2.22d)$$

$$\frac{d\theta_e}{dt} = \omega_e \quad (2.22e)$$

Here ω_e is the rotor electrical rotational velocity, p is the number of pole pairs, J is the rotor rotational inertia, while T_e is the electromagnetic torque, T_{load} is the reaction torque of the load attached to the motor, and T_{loss} is a torque equivalent to the losses on the motor (such as iron or friction losses).

If ψ is assumed to be of form $\psi = i_x L_x + \psi_{PM_x}$ where the inductance only varies with the current and the permanent magnets flux (ψ_{PM_x}) is defined as constant and affecting only the direct axis ($\psi_{PM_q} = 0$), Equations (2.22a) and (2.22b) result in Equation (2.23).

$$u_d = ri_d + \frac{di_d}{dt} \left(L_d + i_d \frac{dL_d}{di_d} \right) - \omega_e L_q i_q \quad (2.23a)$$

$$u_q = ri_q + \frac{di_q}{dt} \left(L_q + i_q \frac{dL_q}{di_q} \right) + \omega_e (L_d i_d + \psi_{PM}) \quad (2.23b)$$

Note that in Equation (2.23) the cross-magnetization effect is not accounted for, but the saturation is

included in the inductance variation [25]. If the inductance derivative is small when compared with the other terms, it can be further simplified to Equation (2.24).

$$u_d = ri_d + L_d \frac{di_d}{dt} - \omega_e L_q i_q \quad (2.24a)$$

$$u_q = ri_q + L_q \frac{di_q}{dt} + \omega_e (L_d i_d + \psi_{PM}) \quad (2.24b)$$

$$T_e = p i_q ((L_d - L_q) i_d + \psi_{PM}) \quad (2.24c)$$

$$\frac{d\omega_e}{dt} = \frac{T_e - T_{load} - T_{loss}}{J} \quad (2.24d)$$

$$\frac{d\theta_e}{dt} = \omega_e \quad (2.24e)$$

Lastly, for the sake of completeness, if the amplitude invariant dq0 transformation is used, the currents need to be multiplied by a factor of $\sqrt{\frac{3}{2}}$ in the torque equation to have a power conservative output, resulting in Equation (2.25). The $\sqrt{\frac{2}{3}}$ next to the ψ_{PM} is just a reminder that the flux linkage value has a different value depending on the dq0 transformation used.

$$T_e = 1.5p i_q ((L_d - L_q) i_d + \sqrt{\frac{2}{3}} \psi_{PM}) \quad (2.25)$$

2.3.4 Discretization of the PMSM model

An approximation of the differential equations is needed to discretize the equations to be able to use the model in a discrete time control system. Two usual solutions are the Backward and the Forward Euler methods. Although simpler to compute, the Forward Euler method is prone to instabilities especially in fast systems such as power converters, in contrast with the Backward alternative that is unconditionally stable. Due to this consideration, the Euler Backward technique will be prioritized.

From Equation (2.24), knowing that the currents and voltages vary with time and that the inductances are dependant on the currents the derivatives are isolated, as shown in Equation (2.26).

$$\frac{di_d}{dt} = \frac{u_d - ri_d + \omega_e L_q i_q}{L_d} \quad (2.26a)$$

$$\frac{di_q}{dt} = \frac{u_q - ri_q - \omega_e (L_d i_d + \psi_{PM})}{L_q} \quad (2.26b)$$

$$T_e = p i_q ((L_d - L_q) i_d + \psi_{PM}) \quad (2.26c)$$

$$\frac{d\omega_e}{dt} = \frac{T_e - T_{load} - T_{loss}}{J} \quad (2.26d)$$

$$\frac{d\theta_e}{dt} = \omega_e \quad (2.26e)$$

Then it is possible to discretize the system with h as the sampling time, and $t = kh$. As the Backward Euler method is desired, the derivatives are approximated by Equation (2.27), resulting in Equation (2.28)

$$\frac{dy}{dt} = \frac{y(k+1) - y(k)}{h} \quad (2.27)$$

$$\left\{ \begin{array}{l} \frac{i_{d(k+1)} - i_{d(k)}}{h} = \frac{u_{d(k+1)} - ri_{d(k+1)} + \omega_{e(k+1)}L_{q(i_q(k+1))}i_{q(k+1)}}{L_{d(i_d(k+1))}} \\ \frac{i_{q(k+1)} - i_{q(k)}}{h} = \frac{u_{q(k+1)} - ri_{q(k+1)} - \omega_{e(k+1)}(L_{d(i_d(k+1))}i_{d(k+1)} + \psi_{PM})}{L_{q(i_q(k+1))}} \\ T_{e(k+1)} = p i_{q(k+1)}((L_{d(i_d(k+1))} - L_{q(i_q(k+1))})i_{d(k+1)} + \psi_{PM}) \\ \frac{\omega_{e(k+1)} - \omega_{e(k)}}{h} = \frac{T_{e(k+1)} - T_{load(k+1)} - T_{loss(k+1)}}{J} \\ \frac{\theta_{e(k+1)} - \theta_{e(k)}}{h} = \omega_{e(k+1)} \end{array} \right. \quad (2.28)$$

This set of equations has an algebraic loop, where the currents in $k+1$ depend on the value of $\omega_{(k+1)}$, that depends on the value of $T_{e(k+1)}$ that is defined by the currents in $k+1$. The same thing happens with the inductances, as they depend on the currents, but the currents define the value of inductance. Those problems are solved by first assuming that the inductance change due to the current change in a time step is small enough so that the inductances can be calculated using the previous time step currents ($L_{x(i_x(k+1))} \approx L_{x(i_x(k+1))}$). Similarly, the rotor speed is assumed to vary little between iterations, so that $\omega_{(k+1)} \approx \omega_{(k)}$.

With those considerations, and rearranging the equations, the system can be solved iteratively, as shown in Equation (2.29).

$$\begin{bmatrix} i_{d(k+1)} \\ i_{q(k+1)} \end{bmatrix} = \begin{bmatrix} 1 & -h \frac{\omega_{e(k)} L_{q(i_q(k))}}{hr + L_{d(i_d(k))}} \\ h \frac{\omega_{e(k)} L_{d(i_d(k))}}{hr + L_{q(i_q(k))}} & 1 \end{bmatrix}^{-1} \left(\begin{bmatrix} \frac{L_{d(i_d(k))}}{hr + L_{d(i_d(k))}} & 0 \\ 0 & \frac{L_{q(i_q(k))}}{hr + L_{q(i_q(k))}} \end{bmatrix} \begin{bmatrix} i_{d(k)} \\ i_{q(k)} \end{bmatrix} + \begin{bmatrix} \frac{h}{hr + L_{d(i_d(k))}} & 0 \\ 0 & \frac{h}{hr + L_{q(i_q(k))}} \end{bmatrix} \begin{bmatrix} u_{d(k+1)} \\ u_{q(k+1)} \end{bmatrix} + \begin{bmatrix} 0 \\ -h \frac{\omega_{e(k)} \psi_{PM}}{hr + L_{q(i_q(k))}} \end{bmatrix} \right) \quad (2.29a)$$

$$T_{e(k+1)} = p i_{q(k+1)}((L_{d(i_d(k+1))} - L_{q(i_q(k+1))})i_{d(k+1)} + \psi_{PM}) \quad (2.29b)$$

$$\begin{bmatrix} \omega_{e(k+1)} \\ \theta_{e(k+1)} \end{bmatrix} = \begin{bmatrix} 1 & 0 \\ h & 1 \end{bmatrix} \begin{bmatrix} \omega_{e(k)} \\ \theta_{e(k)} \end{bmatrix} + \frac{T_{e(k+1)} - T_{load(k+1)} - T_{loss(k+1)}}{J} \begin{bmatrix} h \\ h^2 \end{bmatrix} \quad (2.29c)$$

2.4 Control Methods State of the Art

The quest for higher efficiency and performance has pushed the development in the field of control of electrical machines, and even though several advances have been made, the main strategies in the market are still the FOC with PID current control, and DTC. While robust and well-known, these methods cannot explore the full performance envelope of the controlled machines, and the development of more complex machines with increased dynamic response and efficiency has pushed for new control strategies. In this context, the use of MPC has grown as a good alternative as it explicitly considers the system dynamics and constraints.

2.4.1 Field Oriented Control

For many years field oriented control has been one of the cornerstones of electrical machine control due to its simplicity and easy implementation [26]. This technique is based on the Blondel Park transformation, where it converts the currents and voltages from a stationary ABC reference frame into a rotating referential d_{q0}. This allows the individual control of the motor magnetic flux and torque, which are proportional to i_d and i_q respectively. These currents usually are controlled using two separated PIDs, where the quadrature current reference comes from the desired motor torque and the direct current comes from the field weakening strategy. The PIDs compare the references with the measured values and output a voltage to be applied in each axis, voltages that are passed to a modulator (usually SVM) to calculate the duty cycle of each MOSFET and generate the control signals. An example of such a system is shown in Figure 2.5.

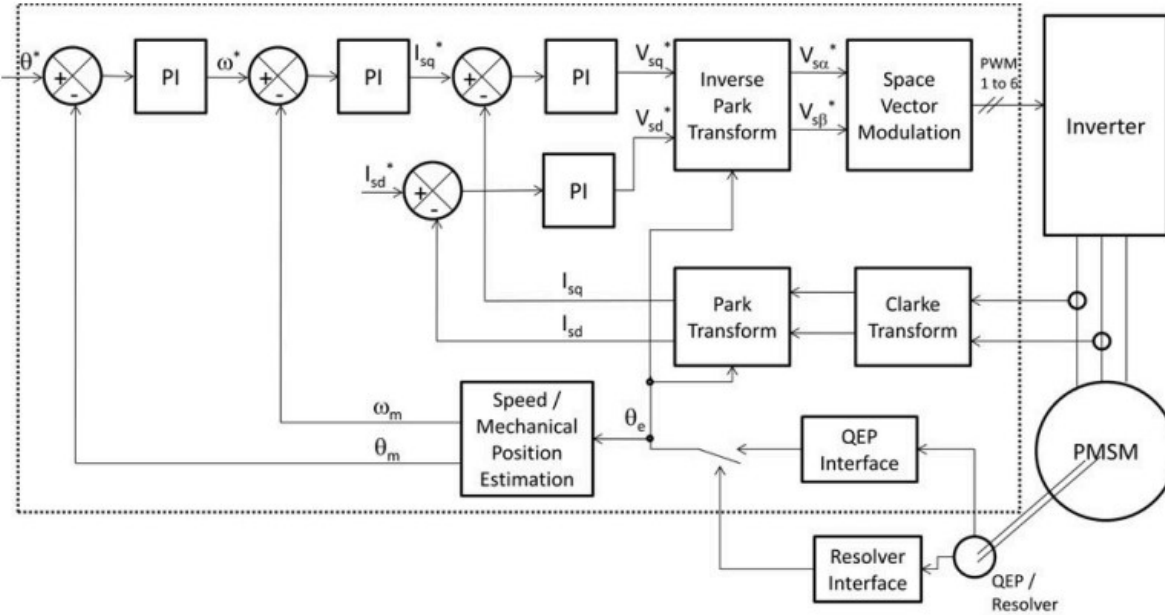


Figure 2.5: Field Oriented Control - from Texas Instruments [27].

While simple and robust, this technique heavily depends on the rotor position which is not always available, thus often needing some form of estimation to work correctly. Despite this limitation, FOC is a

versatile method, being suitable not only for PMSM, but also for induction motors, reluctance machines, among others [28, 29]. One of the great advantages of FOC is that it produces a smooth operation in the full range of the motor, with low current distortions and reduced torque ripple [30].

2.4.2 Direct Torque Control

The principal rival of FOC is DTC, it shows better dynamic response with simpler implementation and less dependency on machine characterization [28]. Popularized by its use on induction machines, this method usually operates at the abc reference frame, calculating the flux based on the voltage and current vectors as in Equation (2.30a), where V_s is the stator voltage vector, I_s is the stator current vector, R_s is the stator resistance matrix, and ψ_r is the rotor magnetic flux vector. Using this information, the torque can be calculated as in Equation (2.30b), where p is the number of pole pairs. When using an induction machine it is not necessary to have a rotor position, but on PMSM this becomes a necessity as in FOC.

$$\psi_s = \int (V_s - R_s I_s) dt + \psi_r \quad (2.30a)$$

$$T_e = p(\psi_s I_s) \quad (2.30b)$$

With these states calculated, a simple hysteresis band is applied to each, torque and flux, to select one of the 8 possible voltage vectors. This selection is done based on a lookup table that depending on the output of both hysteresis controllers, chooses the vector that pushes the torque and flux towards its references. This table can be generated using several strategies with different resultant dynamics [31, 32]. The general schema of the DTC is shown in Figure 2.6. Note that the nature of only switching

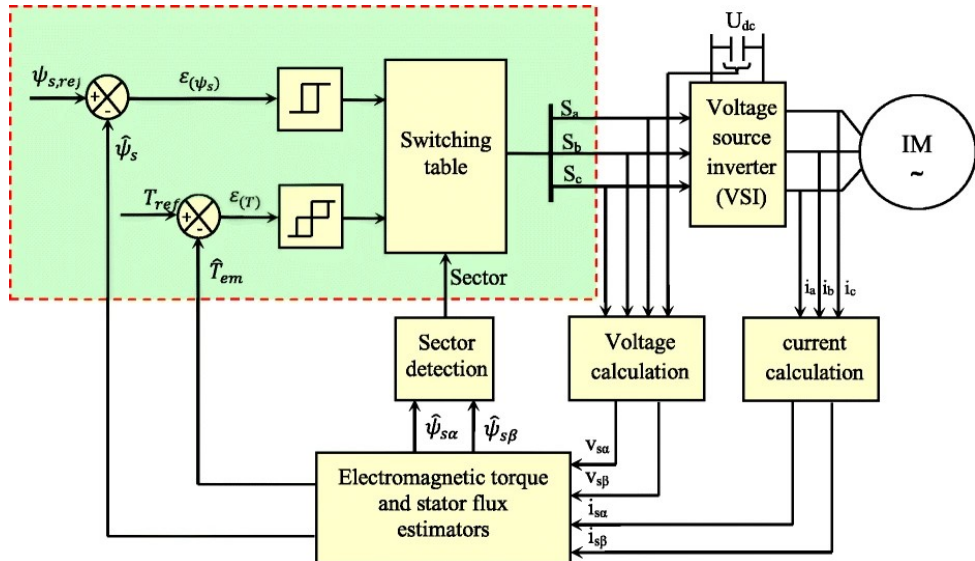


Figure 2.6: Direct Torque Control - from El Ouanjli et al. [33].

vectors when the hysteresis is surpassed results in a variable switching frequency as opposed to FOC that has a fixed switching frequency. Another feature of the DTC is that it does not need any modulators, as it directly chooses the voltage vector to be applied.

DTC is a very accessible method, with simpler implementation than FOC a faster dynamic response and low sensitivity to motor parameters, but it falls short in steady state operation with torque and current

ripple often bigger than its rival FOC [34, 35].

2.4.3 Model Predictive Control

With the increase in computational power, the MPC has gained space among the machine controllers as it handles multivariable non-linear cases, is easy to integrate constraints, and has a great dynamic response and integrates constraint managing [36]. The model predictive controller's basic idea is to use a mathematical model of the controlled system to test several control actions and make a prediction about the system response. This prediction is then evaluated by a cost function that can include some soft constraints and the control action with the smaller cost is chosen as optimal. Vazquez et al. [8] classifies the topologies typically used in power converters and drives into continuous set, and finite set, based on the process used to find the optimal control.

Continuous set is very similar to predictive controllers used on other control fields, it computes a continuous control signal and uses a modulator to generate these voltage vectors. This topology comes with the advantage of fixed switching frequency at the cost of harder implementation and processing power requirements, as it needs an optimization solver. The finite set topology explores the limited control options of power converters to simplify the optimization process. This topology tests a set of the possible control vectors (this set can contain all or part of the possible vectors), and evaluates each of the vectors based on the predictions. While simpler to formulate, this method results in the chosen vector being applied to the full switching period, which results in a higher ripple when compared with a strategy that uses a modulator at the same control frequency. Another property of this strategy is the variable switching frequency, as the same vector can be chosen consecutively.

To reduce the problem of applying the vector for the full timestep, a subset of finite set topology was presented. It adds time as part of the equation by computing the optimal switching sequence instead of the optimal switching vector, similar to a modulator [8]. This allows the controller to choose a set of vectors to be switched in a given sequence with a duration also chosen by the controller.

When applied to PMSM the predictive controllers are commonly designed with the dq0 model Equation (2.24) [37], and may track the currents or the torque to a given reference. The current tracking computational cost tends to be lower as the current optimization can be done offline while tracking torque makes online parameter estimation easier. If the topology is chosen to be continuous, a solver needs to be designed, one of the approaches is to expand the model and cost function into Taylor series approximations, and then use the derivative of the cost function to create a control law [38].

Chapter 3

Machine Characterization and Control Methodology

Contents

3.1 Motor characterization	21
3.1.1 Phase resistance	22
3.1.2 Flux Linkage	22
3.1.3 Machine direct and quadrature inductances	23
3.2 Current References	30
3.2.1 Constraints with limited input voltage	31
3.2.2 Inductance Curves	34
3.3 Load profile	35
3.4 Control Methods Development	36
3.4.1 Finite Set MPC	37
3.4.2 Finite Set with Null Vector MPC	37
3.4.3 Non-Linear Continuous Set MPC	38
3.4.4 RUSH MPC	38

3.1 Motor characterization

Although AMK has provided the motor datasheet (shown in Appendix B) with the key parameters on it, it is important to verify how well they track the real values, and how they change regarding the motor operation. The datasheet values are linear approximations of the magnetic circuit on the motor, and as such do not accurately represent the machine at high current operating points. To account for the saturation effect, a variable inductance approach will be used [39, 40], where the inductance of each axis will be a function of the current on the respective axis.

3.1.1 Phase resistance

Assuming the machine is well balanced, the phase resistance will be equal to $\frac{3}{2}$ of the terminal resistance. Although a multimeter can be used, it will give poor precision, as the resistance is very low, so it's better to use a milliohmmeter or even better a micro-ohmmeter. A good practice would be to evaluate the parameters at different temperatures, especially the resistance, but that would require some specific hardware that is currently not available for this work.

The used device was a *UNI-T UT620A Micro-ohmmeter*, that has a resolution of $10\mu\Omega$ with an accuracy of $\pm(0.25\% + 25\mu\Omega)$. The measurements were taken on the terminal wires at room temperature and with the kelvin probe, resulting in $142.89 \pm 0.06m\Omega$. This value is close to the datasheet one of $135m\Omega$, and the difference is probably due to the wire terminals. The resultant phase resistance (r) is $214.335 \pm 0.091m\Omega$.

3.1.2 Flux Linkage

The magnet flux linkage can be measured by externally rotating the rotor and measuring the generated back EMF. From Equation (2.23), if the terminal wires are disconnected from everything, the current will be constantly zero, thus the measured voltage will be only a result of the flux linkage and the rotor velocity as shown in Equation (3.1).

$$u_d = r_d i_d^0 + \frac{di_d^0}{dt} \left(L_d + i_d^0 \frac{\partial L_d}{\partial i_d} \right) - \omega_e L_d i_q^0 = 0 \quad (3.1a)$$

$$u_q = r_q i_q^0 + \frac{di_q^0}{dt} \left(L_q + i_q^0 \frac{\partial L_q}{\partial i_q} \right) + \omega_e (L_d i_d^0 + \psi_{PM}) = \omega_e \psi_{PM} \quad (3.1b)$$

Using an external device, the rotor was kept at a constant speed that was measured by the digital encoder in the AMK motor, while an oscilloscope (*Promax OD-571*) was connected to two terminal wires. The oscilloscope on the used settings has an accuracy of $\pm(3\% + 0.2508V)$. An example of the output is shown in Figure 3.1(a).

In the example image, the oscilloscope measured a peak voltage of 10.2, while the rotor was spinning at 386rpm , which is equivalent to 202rad/s electrical velocity. This results in a flux linkage of 0.050Wb . The same procedure was repeated at several speeds, and the results are shown in Figure 3.1(b). In this graph, two other lines are shown, they represent the flux linkage estimated using the torque and speed constant provided in the datasheet. Notice that the experimental data aligns well with the value derived from the voltage constant but it is very different from the value derived from the torque constant. This is probably due to different references and transformations being used, but as there isn't much information available on the datasheet, the measured value is assumed to be the correct one.

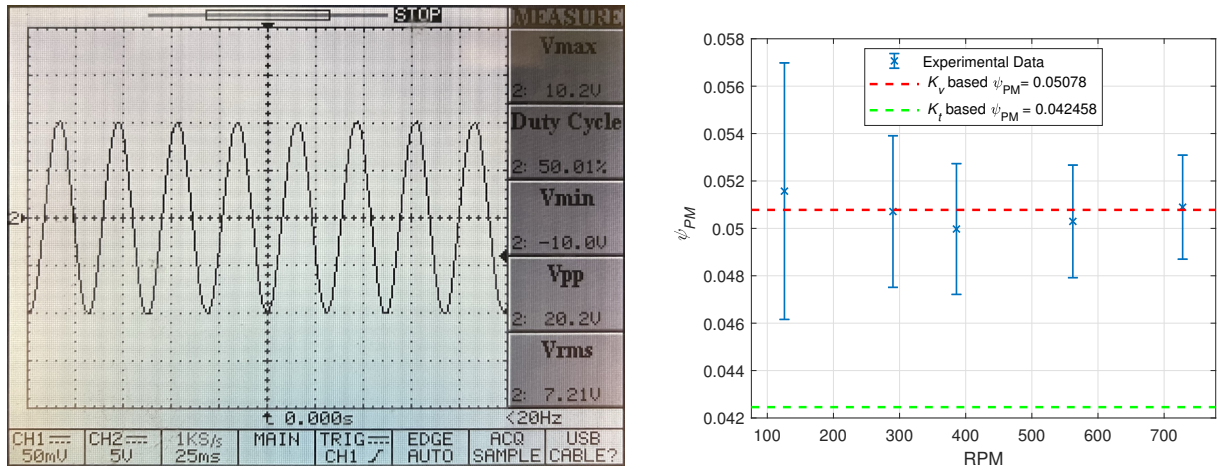


Figure 3.1: Flux Linkage characterization.

3.1.3 Machine direct and quadrature inductances

To achieve better accuracy, two different methods will be proposed, one using the inverter, and the other only using a DC power supply.

3.1.3.1 Method 1

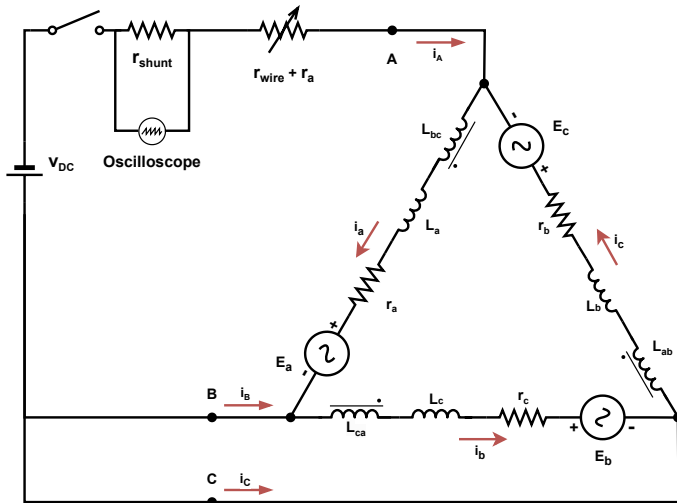


Figure 3.2: Inductance measurement setup schematic.

The simpler method, which does not use the inverter, works by measuring the current throughout a voltage step and measuring the time constant of the system. To measure the current, a shunt resistor is used coupled with the same oscilloscope from the previous section (*Promax OD-571*). To achieve a variable current, a variable resistor was used in series with the shunt, as shown in Figure 3.2. The system resistance was measured with the micro ohmmeter from the previous section (*UNI-T UT620A Micro-ohmmeter*), including wire and switch resistance. The experiment setup is shown in Figure 3.3.

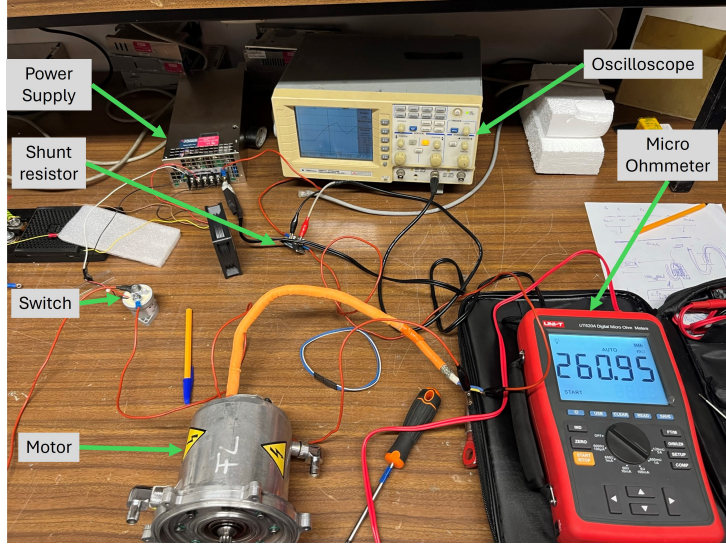


Figure 3.3: Inductance measurement setup.

Direct Axis

The direct axis measurement starts with the resistance measurement of the entire setup, motor, wires, switch, and shunt. Then, a quick voltage pulse is applied to align the rotor with the magnetic field, which in this setup is equivalent to the voltage vector V_6 . In the aligned condition, the current through phase b (i_b) is zero, and $i_a = -i_c$. After the rotor is aligned, a new pulse is done, now for the actual measurement as exemplified in Figure 3.4. The time constant can be retrieved using the basic equation for an RL circuit applied to the shunt resistor (Equations (3.2a) and (3.2b)).

$$u(t) = i_A r_{shunt} (1 - e^{-\frac{t}{\tau}}) \quad (3.2a)$$

$$\tau = \frac{2L_d}{\frac{r}{2} + r_{wire} + r_a + r_{shunt}} \quad (3.2b)$$

In Equation (3.2a) $u(t)$ represents the measured voltage on the shunt resistor, V_{DC} is the power supply voltage, τ is the system time constant, r_a is the variable resistance to adjust the current, r_{shunt} is the shunt resistance, and r_{wire} is the sum of the wire resistances with the switch resistance. To simplify the measurements, instead of calculating the first term $i_A r_{shunt}$, it was replaced by the voltage that which the oscilloscope settled.

With the curve plotted on the oscilloscope, the time constant was measured by evaluating how long it took for the voltage to reach $0.632i_A r_{shunt}$. Then, with the time constant and the system resistance, the inductance was calculated. Note that this inductance was measured for a phase current of half the line current, resulting in a direct axis current of $i_d = \frac{i_A}{\sqrt{3}}$.

The inductance variation with current is not symmetrical in the current axis, as the permanent magnet offsets the magnetic curve, causing saturation with very small positive currents in the direct axis. Although simple, this method has the drawback of not measuring the variation of inductance in the field weakening operating range, only on the field intensifying range that is not often used. To measure in the field weakening range it is necessary to lock the rotor after the initial pulse, and then invert the power

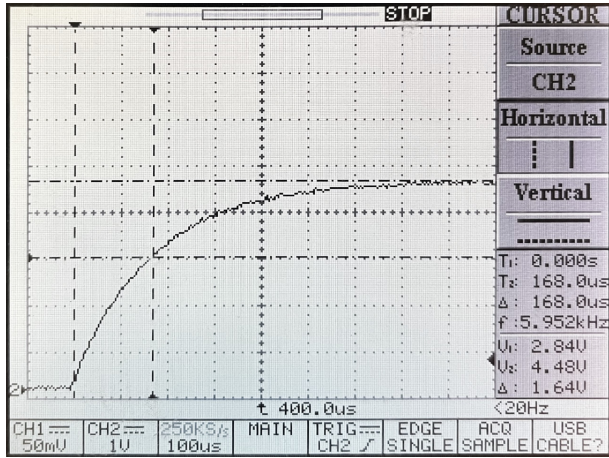


Figure 3.4: Inductance measurement oscilloscope output.

supply polarity.

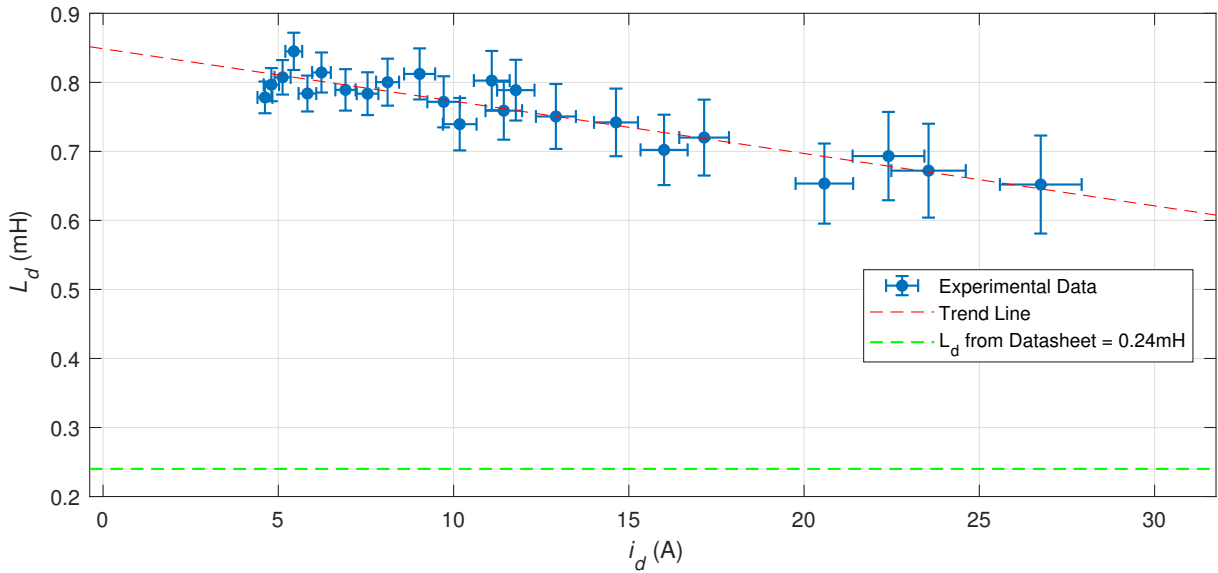


Figure 3.5: L_d in function of i_d .

The test results are shown in Figure 3.5, and as with the flux linkage, there is a great difference between the measured data and the value from the datasheet. The saturation effects are clear and start with very little current, as predicted.

Quadrature Axis

The quadrature axis measurement is very similar to the direct axis, with only two differences. The first change is on the alignment pulse, instead of shorting the B and C terminals and applying the pulse from A to BC as done for the direct inductance measurement, the pulse is only applied from B to C as shown in Figure 3.6. This will align the rotor with the phase b axis allowing it to be locked in a position electrically orthogonal to the resultant voltage of a pulse from A to BC. That is the second difference, after the alignment an external tool is necessary to lock the rotor in place. The rest of the procedure is the same as the direct axis measurement.

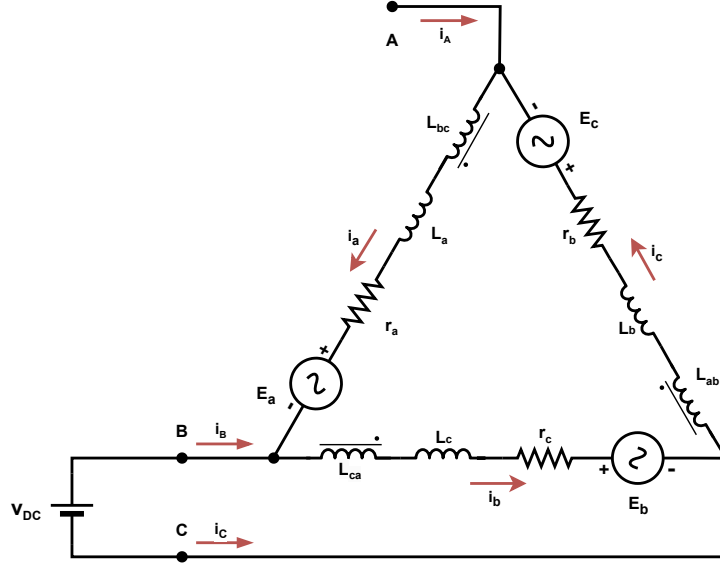


Figure 3.6: Quadrature Inductance measurement alignment pulse setup.

The results of the quadrature inductance are shown in Figure 3.7. It is important to note that as there isn't a reminiscent magnetic flux in the quadrature axis, the variation of the inductance with current is symmetrical in the current axis, and only shows signs of saturation at high currents.

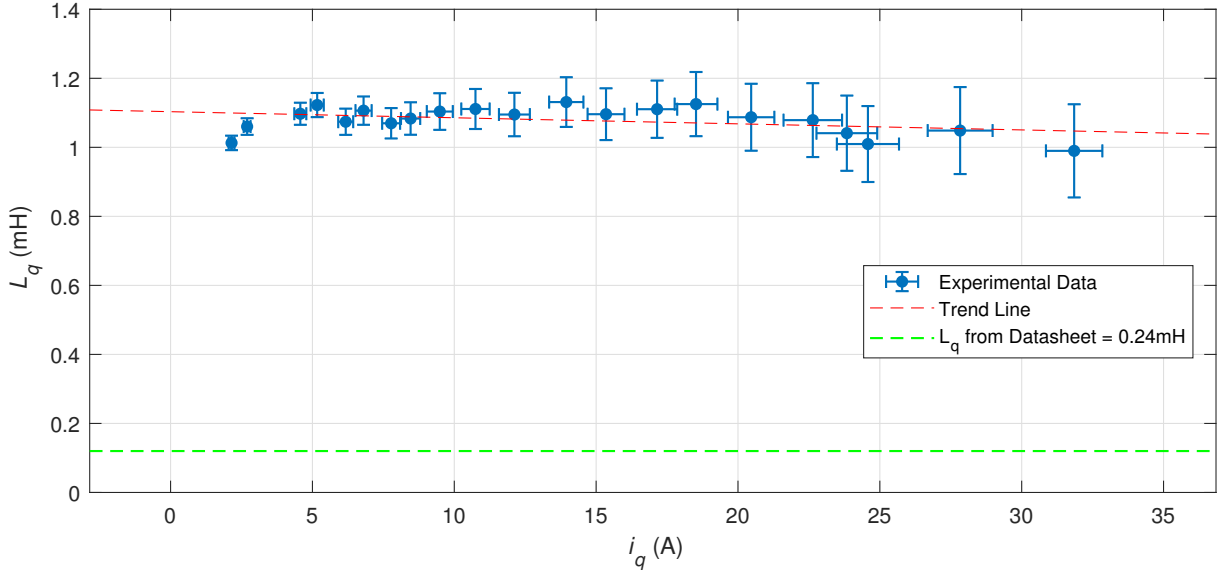


Figure 3.7: L_q in function of i_q .

3.1.3.2 Method 2

The second method for inductance characterization is according to Stumberger et al. [40]. It uses a VSI coupled with a control algorithm to keep the current in one of the axis constant, and then do a voltage step in the other axis. This measurement also needs to be done in a locked rotor position, but it has the advantage of characterizing the cross-magnetization effect. The rotor needs to be locked to

allow the simplification shown in Equation (3.3), resulting in Equation (3.4).

$$u_d = ri_d(t) + \frac{d\psi_d(t)}{dt} - \psi_q \omega_e^0 \quad (3.3a)$$

$$u_q = ri_q(t) + \frac{d\psi_q(t)}{dt} + (\psi_d + \psi_{PM}) \omega_e^0 \quad (3.3b)$$

$$\frac{d\psi_d(t)}{dt} = u_d - ri_d(t) \quad (3.4a)$$

$$\frac{d\psi_q(t)}{dt} = u_q - ri_q(t) \quad (3.4b)$$

This method defines the flux linkage based on the integration of Equation (3.4), and to measure the flux linkage variation in the quadrature axis, it performs a series of stepwise voltage changes in u_q while maintaining the current i_d constant (Figure 3.8). The integration of those curves will result in the quadrature flux linkage variation with i_q . These steps are repeated for several values of i_d , and for each of them, a flux linkage curve is created as shown in Figure 3.9. Note that this figure was generated as a concatenation of two separate voltage steps, one positive and one negative, to simplify the process. This concatenation is the reason for the small misalignment in the flux linkage lines near the origin.

Instead of using the measured value for the phase resistance, its value is estimated by assuming the current is at a steady state at the end of the voltage pulse so that the flux linkage is stable and $u_x = ri_x$, this is done to reduce integration errors on the flux linkage and also to account for wires, connections, and MOSFET resistances.

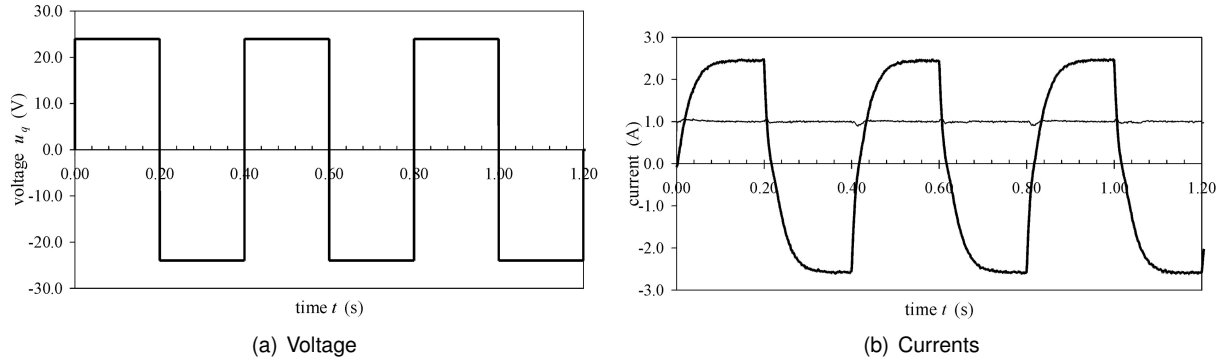


Figure 3.8: Identification voltage pulses - from Stumberger et al. [40].

The same procedure is used for measuring ψ_d , but this time the quadrature current is fixed and the direct voltage is changed in stepwise form. Although the original method is proposed to characterize cross-magnetization effects, the results shown in Figure 3.10 present little variation with currents on the perpendicular axis, thus to simplify the study they are approximated as independent. This approximation is used to reduce the dimensionality of the current reference table and to reduce the used space on the FPGA. To improve the efficiency of the process the quadrature flux linkage was not characterized for positive and negative currents, as the direct axis was, but only for negative currents. Due to the

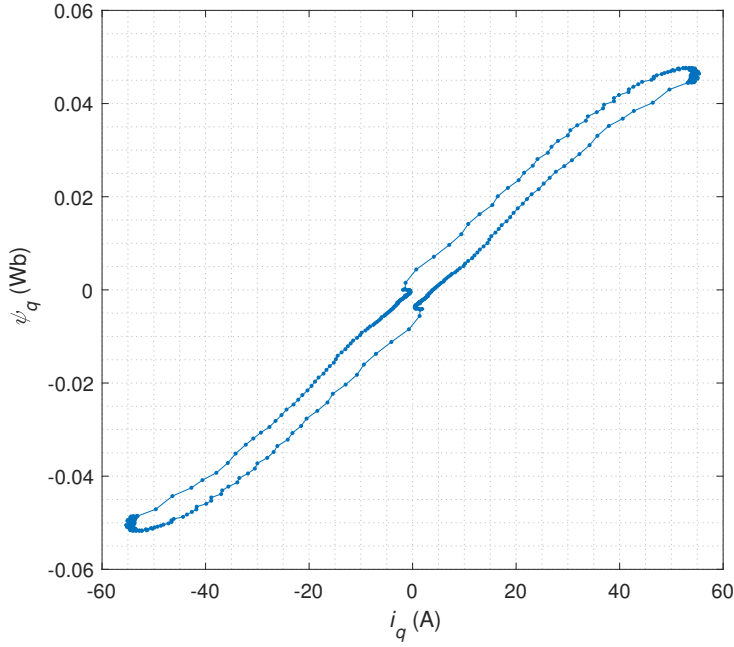


Figure 3.9: Quadrature Flux linkage @ $i_d = -5\text{A}$.

symmetry of the motor, the quadrature axis results were mirrored to create the flux values for positive and negative currents, as shown in Figure 3.10.

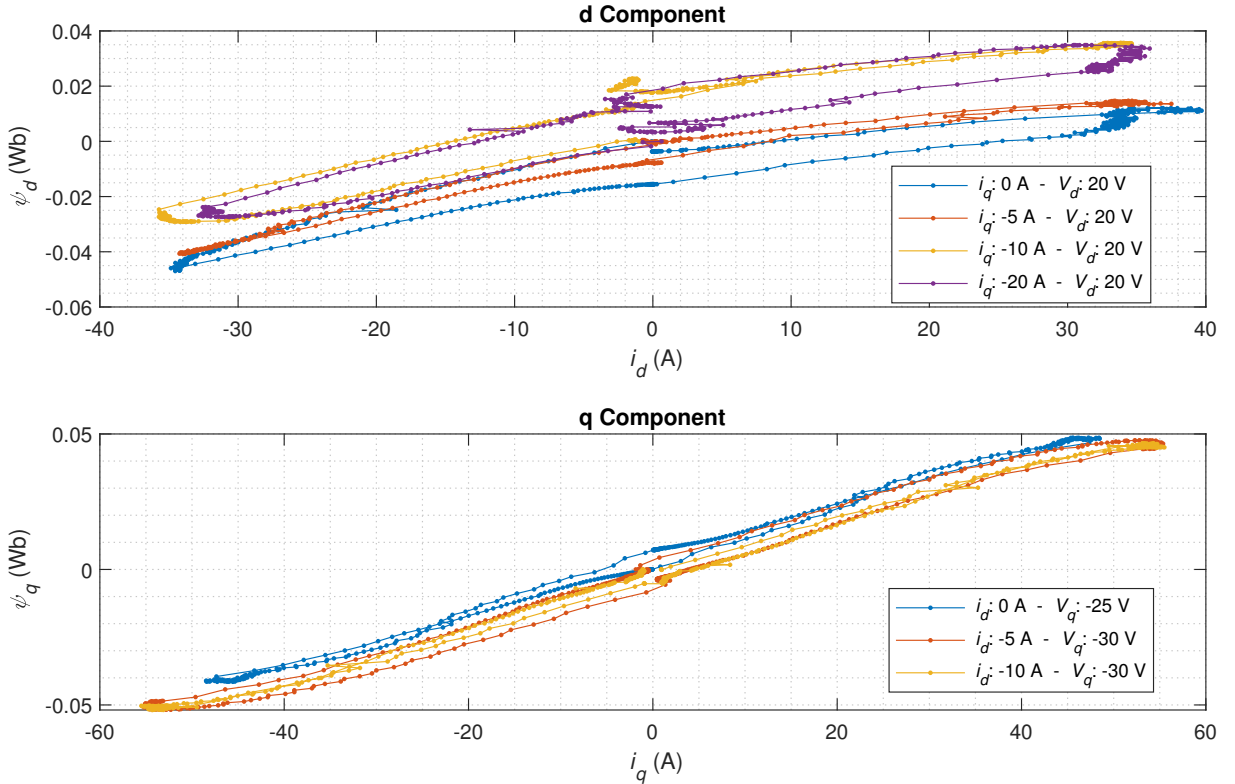


Figure 3.10: Flux linkage with different currents on a perpendicular axis.

After the characterization of the fluxes, an exponential fit is done to the data as shown in Figure 3.11. This fit is made disregarding cross magnetization effects, as explained before, and uses the format of Equation (3.5). This allows analytical differentiation, resulting in Equation (3.6). This derivative is the

inductance value for the given current on the respective axis.

$$\psi_x = (a_1 \cdot e^{-b_1 \cdot x} + a_2 \cdot e^{-b_2 \cdot x}) + c_{down} \left(1 - \left(\frac{1}{a_3 \cdot e^{-b_3 \cdot x} + 1} \right) \right) + c_{up} \left(\frac{1}{a_4 \cdot e^{-b_4 \cdot x} + 1} \right) + c \quad (3.5)$$

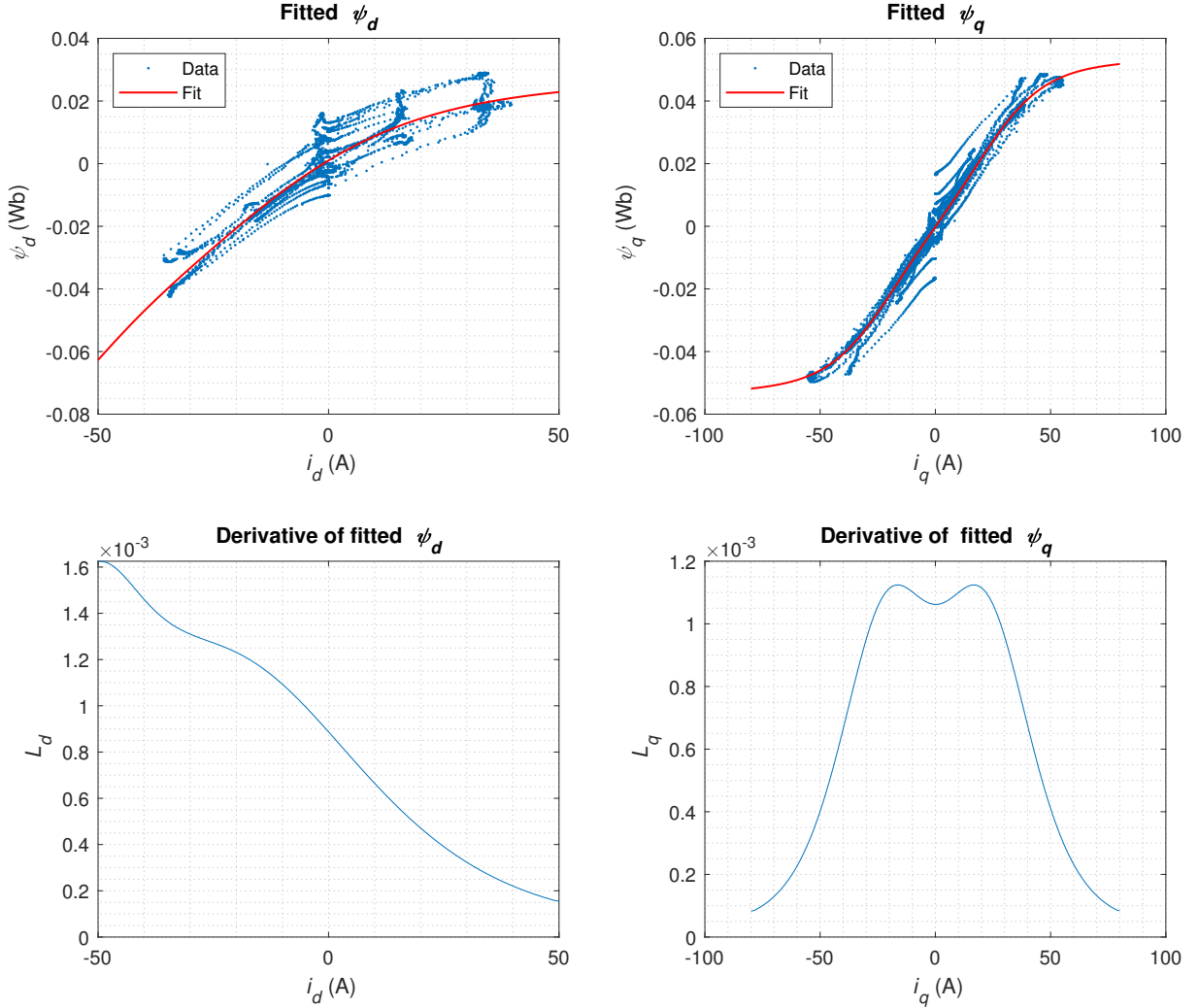


Figure 3.11: Flux Linkage exponential fit. The blue dots are the measured flux linkage, while the red line is the exponential fit (R-square 0.8879 for ψ_d and 0.9681 for ψ_q). The bottom plots show the inductances as the derivative of the fit.

$$L_d = \frac{\partial \psi_d}{\partial i_d} \approx \frac{\Delta \psi_d}{\Delta i_d} \quad (3.6a)$$

$$L_q = \frac{\partial \psi_q}{\partial i_q} \approx \frac{\Delta \psi_q}{\Delta i_q} \quad (3.6b)$$

The resultant inductances are shown in Figure 3.11. The fit has a R-squared value of 0.8879 for the direct axis and 0.9681 for the quadrature axis. The increased error in the direct axis is due to the cross magnetization effects that were not accounted for in the fit.

Ideally, this test should be performed with a voltage pulse big enough to cover the full current range of the machine, but the available hardware was not capable of reaching such currents, thus the limited range. Despite the limitations, the inductance values using this method closely match with the ones found using method 1 from Section 3.1.3.1. This not only increases the confidence in the results but also enables the formulation of a calibration routine on the inverter software that, given some adaptations,

can calculate all the motor parameters within a few minutes.

3.2 Current References

To simplify the real-time computations, the current references can be calculated offline. A simple approach would be to only consider the quadrature current i_q as the main component of torque, and compute the reference using the torque constant. This approach is simple and fast, but it does not account for the motor's inductance, which can be used to increase efficiency. The maximum torque per ampere strategy actively uses the inductance differences between the direct and quadrature axes to get the maximum torque for a given current, but as the inductances are variable, the optimal current reference is also variable. This section aims to calculate the optimal references for the current at all operating points and generate a lookup table for the real-time controller.

Although it is possible to use the MPC to optimize the current references, doing it offline not only allows for faster computational times but also results in more precise references. The downside of this approach is that it negates the possibility of acting upon online parameter estimation, however, this drawback can be mitigated by implementing regular calibration procedures.

As efficiency is one of the objectives, a good approach is to maximize the torque generated by a given current $i = \sqrt{i_d^2 + i_q^2}$. This strategy is called MTPA, and when there aren't constraints it becomes a simple problem defined in Equation (3.7).

$$\begin{aligned} \max_{i_d, i_q} \quad & p i_q ((L_d - L_q) i_d + \psi_{PM}) \\ \text{s.t.} \quad & i = \sqrt{i_q^2 + i_d^2} \end{aligned} \tag{3.7}$$

To optimize 3.7, one can write the problem using Lagrange multipliers (λ), as in Equation (3.8).

$$\mathcal{L} = p i_q ((L_d - L_q) i_d + \psi_{PM}) - \lambda (\sqrt{i_q^2 + i_d^2} - i) \tag{3.8}$$

The partial derivatives of the Lagrange function are defined in Equation (3.9).

$$\frac{\partial \mathcal{L}}{\partial i_d} = p i_q (L_d - L_q) - \frac{\lambda i_d}{\sqrt{i_d^2 + i_q^2}} \tag{3.9a}$$

$$\frac{\partial \mathcal{L}}{\partial i_q} = p ((L_d - L_q) i_d + \psi_{PM}) - \frac{\lambda i_q}{\sqrt{i_d^2 + i_q^2}} \tag{3.9b}$$

$$\frac{\partial \mathcal{L}}{\partial \lambda} = \sqrt{i_q^2 + i_d^2} - i \tag{3.9c}$$

Now, equating the partial derivatives to zero, and replacing Equation (3.9a) in Equation (3.9b) and Equation (3.9c) yields Equation (3.10).

$$i = \sqrt{i_q^2 + i_d^2} \tag{3.10a}$$

$$\frac{\lambda i_d}{i} = p i_q (L_d - L_q) \quad (3.10b)$$

$$\frac{\lambda i_q}{i} = p((L_d - L_q)i_d + \psi_{PM}) \quad (3.10c)$$

Isolating λ in Equation (3.10c) and replacing it on Equation (3.10b), results in Equation (3.11).

$$\frac{p((L_d - L_q)i_d + \psi_{PM})i_d}{i_q} = p i_q (L_d - L_q) \quad (3.11)$$

Rearranging to a quadratic form produces Equation (3.12).

$$i_d + i_d^2 \frac{L_d - L_q}{\psi_{PM}} = i_q^2 \frac{L_d - L_q}{\psi_{PM}} \quad (3.12)$$

Solving for i_d results in Equation (3.13).

$$i_d = \pm \frac{\sqrt{4 \left(\frac{L_d - L_q}{\psi_{PM}} \right)^2 i_q^2 + 1} - 1}{2 \frac{L_d - L_q}{\psi_{PM}}} \quad (3.13)$$

But comparing with the torque equation is clear that the negative option would not maximize the torque, thus, the final result is Equation (3.14).

$$i_d = \frac{\sqrt{4 \left(\frac{L_d - L_q}{\psi_{PM}} \right)^2 i_q^2 + 1} - 1}{2 \frac{L_d - L_q}{\psi_{PM}}} \quad (3.14)$$

This equation is valid for a constant inductance and with no constraints. If the inductance curve is used then an iterative approach can solve the algebraic loop of the inductances. If the inductances are assumed to be monotonically decreasing, then the iterative approach is guaranteed to converge to the proper value, resulting in Figure 3.12.

3.2.1 Constraints with limited input voltage

While direct, the presented approach does not account for voltage limitations, meaning that when the rotor speed increases the back emf becomes large enough to limit the current operation points. To account for that the voltage constraint must be defined.

If the current is assumed to be constant, Equation (2.24) can be rearranged to calculate the maximum current for a given voltage and velocity as in Equation (3.15), with the voltage constraint defined in Equation (3.16).

$$u_d = r i_d - \omega_e L_q i_q \quad (3.15a)$$

$$u_q = r i_q + \omega_e (L_d i_d + \psi_{PM}) \quad (3.15b)$$

$$\sqrt{u_d^2 + u_q^2} \leq V_{DC} \quad (3.16)$$

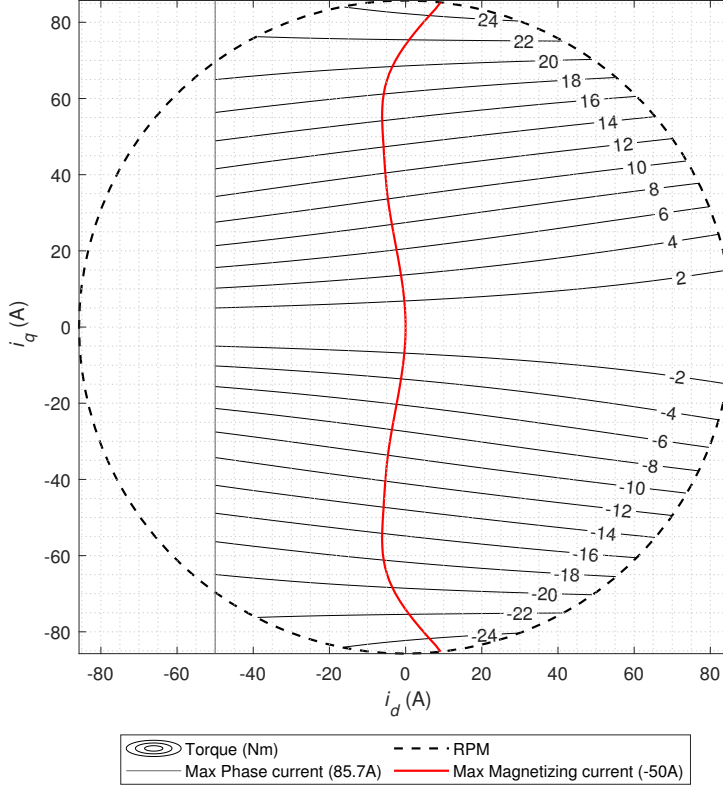


Figure 3.12: Maximum Torque per Ampere curve without constraints.

Subjecting Equation (3.15) to Equation (3.16) an ellipse equation is obtained, where the center is defined by the rotor speed and the flux linkage, while the radius is defined by the DC link voltage and the resistance. The ellipse is defined as in Equation (3.17).

$$(ri_d - \omega_e \psi_q)^2 + (ri_q + \omega_e \psi_d^*)^2 \leq V_{DC}^2 \quad (3.17)$$

Here $\psi_d^* = L_d i_d + \psi_{PM}$ and $\psi_q = L_q i_q$. Note that this ellipse size dynamically changes depending on the instantaneous rotor velocity and DC link voltage.

Using the ellipse as a constraint, Equation (3.7) can be rewritten as in Equation (3.18), where the speed and DC link voltage are known.

$$\begin{aligned} \min_{i_d, i_q} \quad & \sqrt{i_q^2 + i_d^2} \\ \text{s.t.} \quad & T_{ref} = p i_q ((L_d - L_q) i_d + \psi_{PM}) \\ & (ri_d - \omega_e \psi_q)^2 + (ri_q + \omega_e \psi_d^*)^2 \leq V_{DC}^2 \end{aligned} \quad (3.18)$$

This optimization problem was formulated on *MATLAB* for several speeds and voltages. Some of the main cases are shown in Figure 3.13. On this graph, the iso-torque lines show the current combinations that yield the same torque, independent of the velocity or the voltage. The voltage ellipses are defined from the rotor velocity and the current DC link voltage, and they assume that the current is constant. The area contained by the ellipse is the feasible region at that speed and supply voltage. Steady-state operation at any point outside the ellipse would require a speed reduction or a voltage increase.

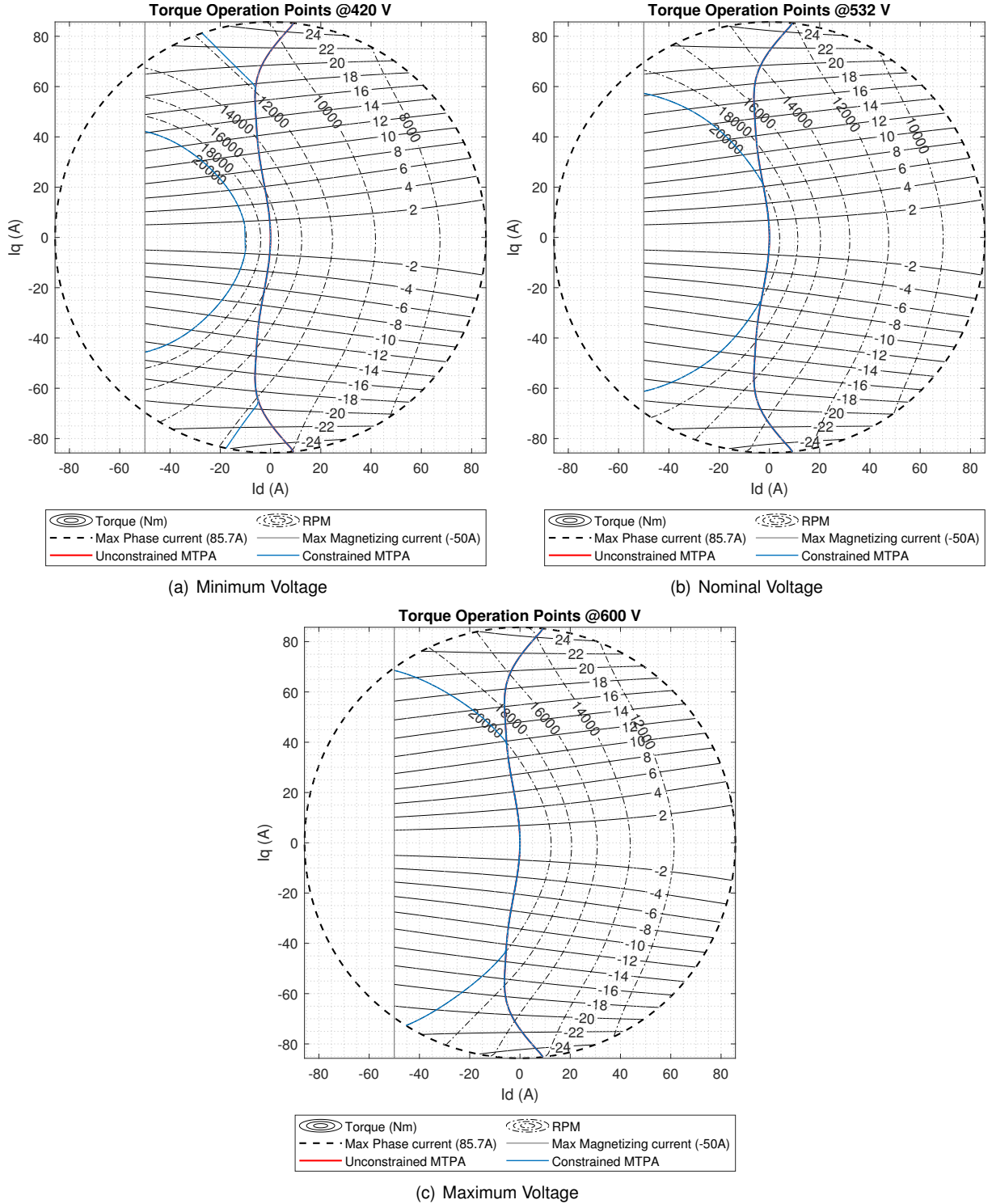


Figure 3.13: Constrained Maximum Torque per Ampere curve at minimum, nominal, and maximum voltages. Reference currents are shown for 0, 13000 and 2000 RPMs.

Note that while the torque map is symmetrical relating to the i_d axis, the voltage ellipse is not, it has been rotated slightly in an anti-clockwise direction. This rotation is due to the resistance of the phases that when the machine is working as a motor, reduce the total available voltage to fight the back EMF. If the phase resistance is low the ellipse becomes aligned with the i_d axis. Another important remark is the center of the voltage ellipse, as the AMK motor has permanent magnets with strong flux linkage the

ellipse center is shifted farther away from the origin, but in a reluctance machine, the center would be at the origin, the same as the torque. Special cases appear when the ellipse center is inside the feasible current region, as the voltage-limited speed goes to infinity. An important location in this graph is the motor characteristic point, which can be easily located as being the place where the maximum phase current circumference yields the higher torque. The speed at this point is the motor's characteristic speed, and if the graph is created for the motor's nominal voltage, that becomes also the nominal speed of the motor. This point is important as any further increase in speed will result in a reduction in the maximum motor torque.

Figure 3.13 clearly shows that the optimal current reference is the MTPA while the velocity and voltages allow it, and after that, the voltage ellipse becomes the best alternative. It is important to understand that the voltage constraint is dependent on the combination of DC Link voltage and rotor speed, when the voltage increases the ellipse for a given speed expands, allowing further operation on the unconstrained MTPA line. This not only increases efficiency (as it produces the same torque with less current) but also improves performance, pushing the motor characteristic point further on the torque vs rpm diagram.

Some processing is still needed to account for points outside of the feasible region, but the presented graphs can be used as a motor map, where given the current DC Link voltage, motor speed, and desired torque, it returns the reference currents to optimally reach the torque reference. This can also be expanded to include temperature effects.

3.2.2 Inductance Curves

The inductance curves used to generate the motor maps presented in Section 3.2 were obtained from a spreadsheet provided by the manufacturer that contained simulation data. The inductances computed from it are presented in Figure 3.14. However, for the sake of completeness, the current reference curves generated from the inductance values obtained through characterization (Figure 3.11) are included in the Appendix C. This was necessary because a working testbench with stable control was needed to properly characterize the inductances. This characterization was completed after the implementation of the control in the experimental setup. Unfortunately, shortly after, testbench limitations impeded further testing. Consequently, the maps generated using the characterization inductance curves were not tested experimentally.

Note that replacing the manufacturer tables with the characterized inductance curves from the appendix should not have a significant impact on the controller performance, only affecting the current references passed to the controller. The process to generate the current references and the controller structure remains the same despite the inductance curves.

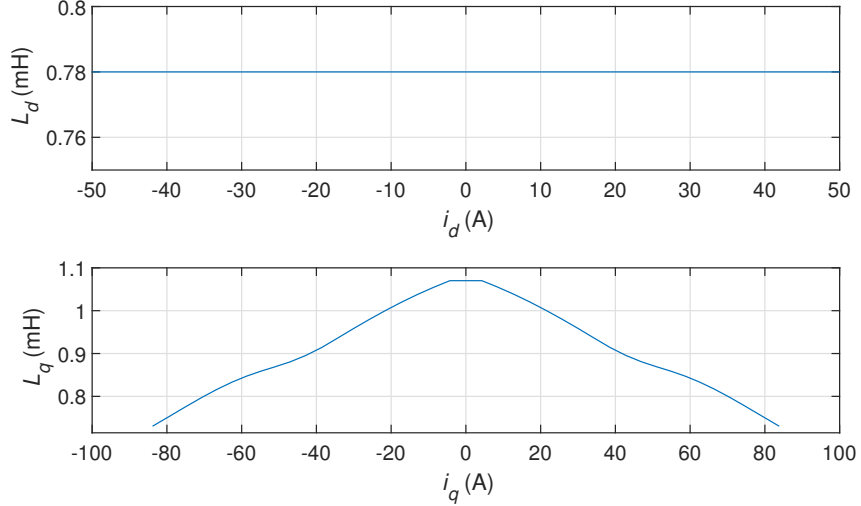


Figure 3.14: Manufacturer inductance curves.

3.3 Load profile

To properly simulate the use case of the motor, a representative load profile must be defined. This profile will be used in the motor torque balance equations inside the simulations. To derive a representative load profile for the motor a car model is necessary. In this case, a simple one-dimensional point mass model is used in Equation (3.19).

$$(m_{car} + m_{wheel\ equivalent}) a_x = F_{motor} \eta_{transm} - F_{rolling\ resistance} - F_{drag} \quad (3.19)$$

Where the rolling resistance is a constant force that depends on the rolling resistance coefficient and the weight of the car (Equation (3.21)), the losses are neglected, and the aerodynamic drag is calculated as in Equation (3.20).

$$F_{drag} = 0.5 \rho C_d A_r v^2 \quad (3.20)$$

$$F_{rolling\ resistance} = C_r m_{car} g \quad (3.21)$$

To calculate the inertia seen by the motor, an equivalent rotational inertia must be computed. To do that, the energy stored in the rotating parts and on the car is equated with the equivalent inertia as shown in Equation (3.22). This equation was rearranged as shown in Equations (3.23) to (3.25), which results in Equation (3.26).

$$\frac{1}{2} J_{eq} \omega^2 = \frac{1}{2} m_{car} v^2 + \frac{1}{2} J_{wheels} \omega^2 \quad (3.22)$$

$$\frac{1}{2} J_{eq} \omega^2 = \frac{1}{2} m_{car} (\omega_{wheels} r_{tire})^2 + \frac{1}{2} J_{wheels} \omega_{wheels}^2 \quad (3.23)$$

$$\frac{1}{2} J_{eq} \omega^2 = \frac{1}{2} m_{car} \left(\frac{\omega}{Gr} r_{tire} \right)^2 + \frac{1}{2} J_{wheels} \left(\frac{\omega}{Gr} \right)^2 \quad (3.24)$$

$$\frac{1}{2} J_{eq} \omega^2 = \frac{1}{2} \left(\frac{m_{car} r_{tire}^2}{Gr^2} + \frac{J_{wheels}}{Gr^2} \right) \omega^2 \quad (3.25)$$

$$J_{eq} = \frac{m_{car} r_{tire}^2 + J_{wheels}}{Gr^2} \quad (3.26)$$

From experimental tests with previous prototypes, a good rule of thumb is that when accelerating, only one-third of the power can be applied at the front axle, while the rear axle receives two-thirds. Ideally, a weight transfer function would be used, but to simplify the equations the constant distribution will be used. Thus the equivalent rotational inertia at each motor is on Equation (3.27).

$$J_{f_{eq}} = \frac{m_{car}r_{tire}^2 + 6 J_{wheel}}{6 Gr^2} \quad (3.27a)$$

$$J_{r_{eq}} = \frac{m_{car}r_{tire}^2 + 3 J_{wheel}}{3 Gr^2} \quad (3.27b)$$

Combining the equations, a torque profile is defined in Equation (3.28).

$$J_{f_{eq}} \dot{\omega} = T_{motor} \eta_{transm} - \frac{(F_{rolling\ resistance} + F_{drag}) r_{tire}}{6 Gr} \quad (3.28a)$$

$$J_{r_{eq}} \dot{\omega} = T_{motor} \eta_{transm} - \frac{(F_{rolling\ resistance} + F_{drag}) r_{tire}}{3 Gr} \quad (3.28b)$$

3.4 Control Methods Development

In this section some of the main MPCs used on the power converters field are developed. At the end of the section, the proposed control strategy is presented. The methods compared with the manufacturer's FOC are:

- Finite Set MPC
- Finite Set with null vector MPC
- Non-Linear Continuous Set MPC
- Real-time Ultra Short Horizon extension MPC (RUSH MPC)

All those methods rely on the line current and rotor position encoder data to estimate the currents in the d_q frame. The DC Link voltage is also measured to account for battery voltage fluctuation. The control strategy is then applied to the motor model to predict the next time step values. This processed data is refreshed at each time step to be utilized by the selected control strategy. Although it is possible to use multiple horizon prediction steps, to keep the computational cost low, and maintain high switching frequencies, all the proposed methods use a horizon of only 1 discretized time step.

Some of these control methods depend on a cost function definition to choose the best control action. The control action that minimizes this cost function is then applied to the system.

$$\mathcal{J} = s_1 \left(\frac{i_{d_{ref}} - i_{d_{k+1}}}{i_{d_{ref}}} \right)^2 + s_2 \left(\frac{i_{q_{ref}} - i_{q_{k+1}}}{i_{q_{ref}}} \right)^2 + \mathcal{C}_{soft} \quad (3.29a)$$

$$\mathcal{C}_{soft} = s_3 \max \left(0, \sqrt{i_{d_{k+1}}^2 + i_{q_{k+1}}^2} - \sqrt{\frac{2}{3} i_{linemax}} \right) + s_4 \max \left(0, \sqrt{u_{d_{k+1}}^2 + u_{q_{k+1}}^2} - V_{DC} \right) \quad (3.29b)$$

The cost function shown in Equation (3.29a) is composed of the error between the reference and the predicted values of the currents, and a soft constraint that penalizes the system for exceeding the maximum line current or the DC link voltage while some gains s_x are used to adjust the priorities. The soft constraint is defined in Equation (3.29b).

3.4.1 Finite Set MPC

In a FS-MPC each of the basic vectors defined on Table 2.2 are applied to Equation (2.29) using the current measured data, resulting in different predictions for the next time step values. A cost function that compares the torque and currents (to account for MTPA) with the references, is then evaluated for each of those predictions. The vector with the lowest cost is then applied at the next time step, as shown in Figure 3.15.

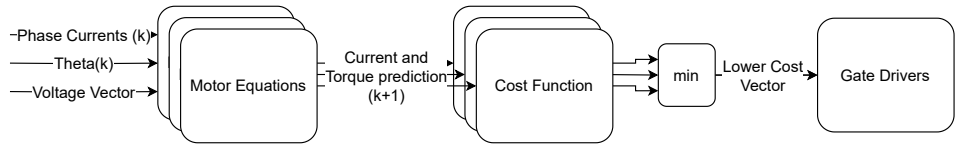


Figure 3.15: FSMPC Diagram.

3.4.2 Finite Set with Null Vector MPC

Although effective, the simple Finite Set MPC can incur heavy torque ripple, due to its limited options on which vector can be applied. That behavior can be exacerbated by low power operation points, where the active vectors result in a bigger percentual change in currents. This problem can be mitigated by introducing the possibility of sharing the sample time between the chosen active vector and a null vector. Such an approach allows the control to apply vectors that point in the direction of the native ones but have smaller amplitude.

This addition of a null vector comes with the problem of now having virtually infinite vector options (depending on the PWM resolution), but that can be solved with some approximations. This method begins as the previous one, where each of the 7 possible vectors is applied to the motor model, but before passing those results for the cost function the predicted torque is compared with the reference. If a crossing is detected, meaning the values $T_{ref} - T_{e(k)}$ and $T_{ref} - T_{e(k+1)}$ have different signs the algorithm assumes that the ideal vector has a smaller amplitude, thus computes a ratio of active vector time and null vector time. To calculate such a ratio an approximation was made that, given the short sample time, the complete system is assumed to behave linearly during that period. If the system behaves linearly, the currents and torque for a combination of null and active vectors will also be a linear combination of the individual values for each vector multiplied by its application time. This approximation is shown in Equations (3.30) and (3.31), where d is the duty cycle value for a given vector, and the subscripts a and n represents the active and null vectors respectively.

$$i_x = i_a d_a + i_n d_n \quad (3.30)$$

$$T_x = T_a d_a + T_n d_n = T_a d_a + T_n - T_n d_a \quad (3.31)$$

With that property, and knowing that $d_a + d_n = 1$ the duty cycle for the active vector is calculated as shown in Equation (3.32).

$$d_a = \frac{T_{ref} - T_n}{T_a - T_n} \quad (3.32)$$

Given the duty cycle, the predictions are updated and passed to the cost function, which chooses the best combination of active and null vectors. A diagram of this method is shown in Figure 3.16.

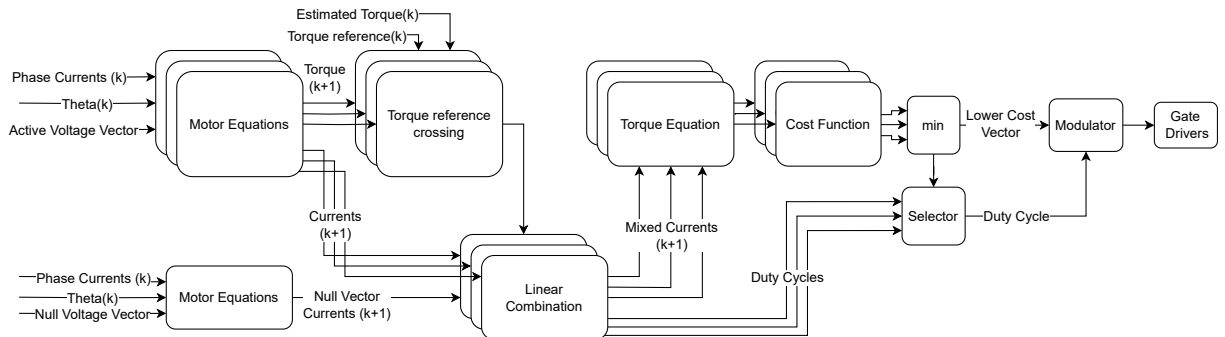


Figure 3.16: Finite Set with Null Vector MPC Diagram.

3.4.3 Non-Linear Continuous Set MPC

In the continuous set MPCs the control action is not limited to a finite set of vectors, but it is assumed that any vector attainable by a defined modulation technique is available. This increases the complexity of the control, as the control action locus becomes infinite. This approach is very similar to the most common approach of MPC used in other fields that are not power systems. It takes an implicit approach, where the motor model shown in Equation (2.29) is combined with an optimization solver that numerically finds the best control action. This MPC technique has the advantage of easy constraints implementation while having the benefits of a continuous set controller. This advantage comes at the cost of largely increased computational time, as it needs to evaluate the model equation several times to find the optimal voltage vector that fulfills the constraints. This additional complexity can often be prohibitive for power systems where a fast-acting control is needed. The diagram of this method is shown in Figure 3.17.

3.4.4 RUSH MPC

One of the advantages of the approximations made in the discretization process is that even though the matrices change in time, for a given moment the system is linear, and as such an inverse dynamic can be derived. So, if in Equation (2.29) the currents on the next step are replaced by a reference

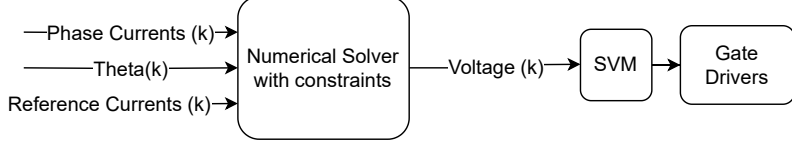


Figure 3.17: Implicit Continuous Set MPC Diagram.

for the current vector, the necessary applied voltage can be calculated in real-time. This is done by Equation (3.33).

$$\begin{bmatrix} u_{d(k+1)} \\ u_{q(k+1)} \end{bmatrix} = \begin{bmatrix} \frac{h}{hr+L_{d(i_d(k))}} & 0 \\ 0 & \frac{h}{hr+L_{q(i_q(k))}} \end{bmatrix}^{-1} \left(\begin{bmatrix} 1 & -h \frac{\omega_{e(k)} L_{q(i_q(k))}}{hr+L_{d(i_d(k))}} \\ h \frac{\omega_{e(k)} L_{d(i_d(k))}}{hr+L_{q(i_q(k))}} & 1 \end{bmatrix} \begin{bmatrix} i_{dref} \\ i_{qref} \end{bmatrix} - \begin{bmatrix} \frac{L_{d(i_d(k))}}{hr+L_{d(i_d(k))}} & 0 \\ 0 & \frac{L_{q(i_q(k))}}{hr+L_{q(i_q(k))}} \end{bmatrix} \begin{bmatrix} i_{d(k)} \\ i_{q(k)} \end{bmatrix} - \begin{bmatrix} 0 \\ -h \frac{\omega_{e(k)} \psi_{PM}}{hr+L_{q(i_q(k))}} \end{bmatrix} \right) \quad (3.33)$$

This approach is commonly used in linear unconstrained MPCs to improve computation times, where a control law is precomputed and stored in memory. But in the presented case there is an important constraint that is not accounted for in the previous equation. When very short time steps are used, and there is a big reference change, the necessary voltage to achieve the target on just one discrete time step can be very high. This would lead to problems, like distortions due to overmodulation or not being able to reach the desired voltages. The solution to this problem is to saturate the voltage vector. Some authors have suggested saturating based on the closest possible vector [41], in this work, the saturation only limits the vector amplitude to match the DC-link voltage, maintaining the desired vector angle as shown in Equation (3.34).

$$\gamma = \arctg \left(\frac{u_{d(k+1)}}{u_{q(k+1)}} \right) \quad (3.34a)$$

$$u_{sat_{d(k+1)}} = \min(u_{d(k+1)}, V_{dc} \cos(\gamma)) \quad (3.34b)$$

$$u_{sat_{q(k+1)}} = \min(u_{q(k+1)}, V_{dc} \sin(\gamma)) \quad (3.34c)$$

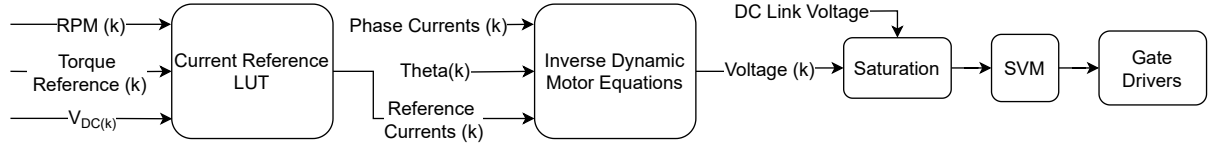


Figure 3.18: Explicit Continuous Set MPC Diagram.

This method greatly reduces the time taken to compute the control action, as instead of trying 7 different possible inputs (or more) it just calculates one time the necessary voltage and clamps it to the attainable values. As this control uses a continuous set, those values are then forwarded to a SVM

system to modulate the Pulse Width Modulator (PWM) signals. The diagram of this method is shown in Figure 3.18.

3.4.4.1 Horizon Extension

A previously overlooked problem is the compensation of the computational time, as the acquisition and control calculations cannot be done instantly their delay needs to be compensated. The strategy adopted here is to use the motor model equations Equation (2.29) coupled with the previously calculated control action to predict the system state in the next time step, this is called horizon extension. Usually, this is done in a fixed timestep manner, where the predictive controllers instead of picking the control action for k in the timestep k , pick the control action for $k+1$ in the timestep k , as shown in Equation (3.35) where x represent the currents, u is the voltage vector, A , B , C , and D are the matrices and vectors of the model in Equation (2.29) and are all dependent on the prediction duration $h = \frac{1}{f_{sw}}$.

$$x_{k+1} = A^{-1} (Bx_k + Cu_k + D) \quad (3.35)$$

For this equation to work the system timeline needs to be as in Figure 3.19, starting with taking the current and voltage measurements, followed by applying the voltage vectors calculated in $k - 1$, then extending the horizon by one timestep, and calculating the voltage vector for the next timestep [36].

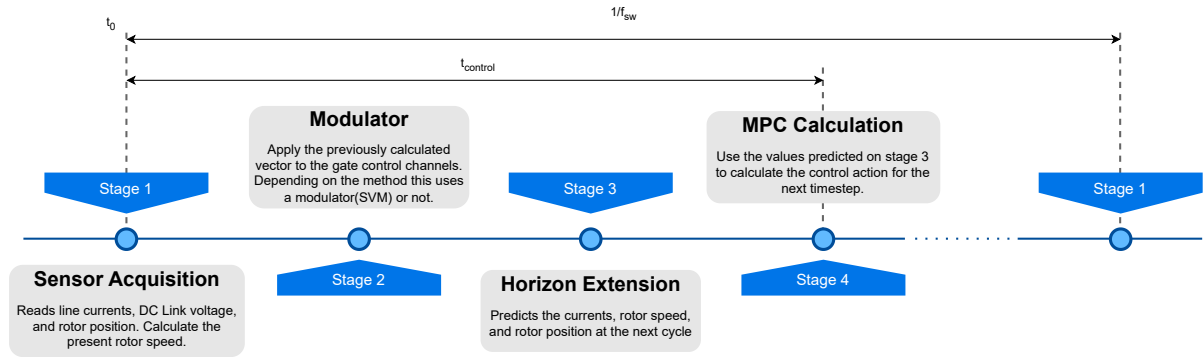


Figure 3.19: Horizon extension by one timestep.

This can be improved by only extending the horizon by the necessary time to compute the control action, this way the prediction error derived from model mismatch is reduced because the amount of time to predict is smaller. To do that the prediction duration is simply reduced to $h = t_{control}$, while the system timeline is shifted as in Figure 3.20. The combination of explicitly solving the MPC model equation with the hybrid horizon timestep approach, where the horizon extension has a shorter timestep than the controllable horizon is called Real-time Ultra Short Horizon extension MPC (RUSH MPC). It has the benefits of being a continuous set model predictive control, thus reducing the ripple, while being computationally efficient, as it is explicitly calculated, and reducing the prediction error due to model mismatch as it uses the reduced horizon extension technique.

The final control cycle starts with sensor acquisition, followed by horizon extension, and lastly the future control action computation. Note that this delay is not a problem with simulation in *Simulink*, as it

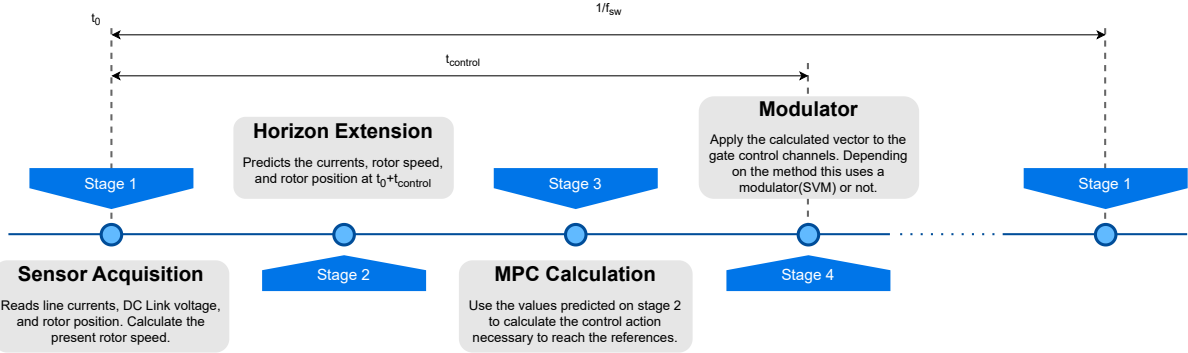


Figure 3.20: Horizon Extension by control time.

can instantly do the calculations, but it is good practice to simulate it with the proper delays to increase the similarity between simulation and experimental results.

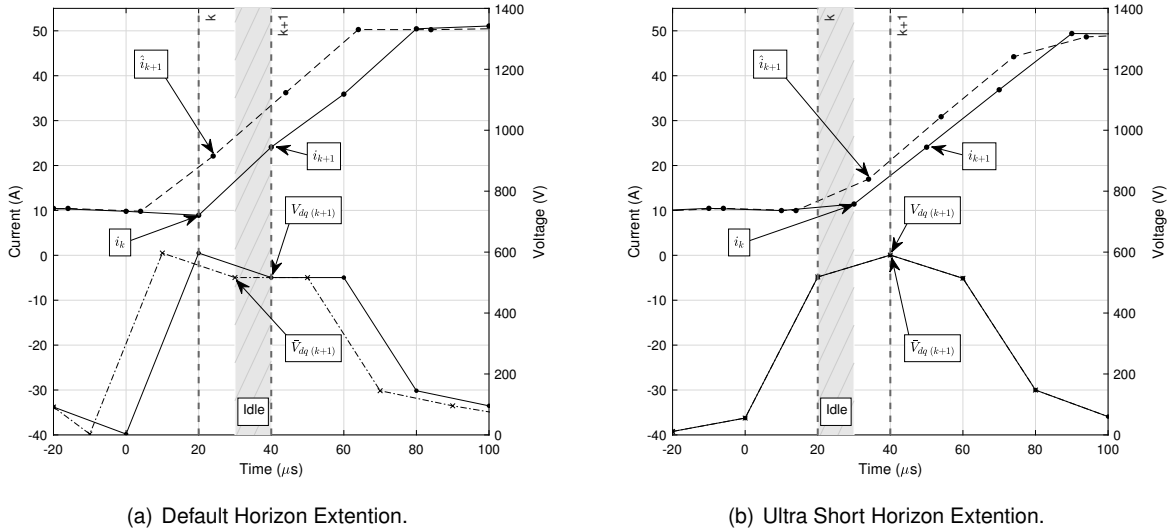


Figure 3.21: Horizon extension comparison, on top the measured and predicted voltages. The bottom lines are the computed control action and the applied control action

A comparison of the different horizon extension methods is shown in Figure 3.21. The lines on the top represent the predicted and measured currents, while the lower lines are the voltages. Note that the markers in this figure are placed on the exact time the hardware finishes each computation, thus the delay between measurement, extension, and control calculation. The dashed voltage line represents the control action at the computation time, so in the regular horizon extension it is ahead of the applied control action. The ultra short horizon technique allows it to be applied as soon as it is computed.

3.4.4.2 Speed Control

In the current architecture, the car has a slip controller that is responsible for limiting the amount of slip on the wheels. This controller is based on limiting the maximum (or minimum in the case of braking) speed that a wheel can have. In order to implement this it is necessary to have a rotor speed control.

While this could be implemented directly on the MPC, the speed dynamics are much slower than the current dynamics, and as such, it is possible to use a simpler control method. The proposed method is a PI controller that receives the rotor speed error and outputs a torque reference. This torque reference is then passed through a saturation which has the limits defined by the throttle and brake pedals, and the resultant torque is used as the input for the MPC controllers. The saturation of torque is considered in the integral part of the PI, clamping it if the output is saturated. This structure is shown in Figure 3.22.

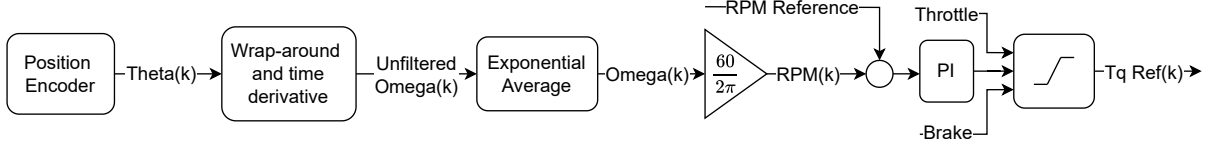


Figure 3.22: Speed control diagram.

Note that Figure 3.22 also presents a calculation for the rotor speed, this is done by calculating the difference in rotor position between two-time steps and dividing by the sample time. As the rotor position encoder is absolute the position value has a wrap-around point, and thus to calculate the position time derivative an assumption is made that the rotor position does not change more than 180 degrees between two samples. This assumption is valid as the maximum speed of the motor is 20000rpm , which translates to 333Hz , and the sample time of the encoder is smaller than $70\mu\text{s}$, meaning that the rotor can only move 8.4° between samples. This value can increase in the case of a failure in the encoder, but the margin is large enough to accommodate eventual encoder failures. With the rotor position derivative calculated, exponential averaging is applied to smooth the signal and reduce noise, this is done by Equation (3.36), where α is the smoothing factor, that defines the weight of the past samples in the current average.

$$\omega_{(k+1)} = \alpha\omega_{(k)} + (1 - \alpha)\frac{\theta_{(k+1)} - \theta_{(k)}}{h} \quad (3.36)$$

A continuous approximation of the exponential moving average can be modeled as a transfer function of a first-order system, with a time constant defined by the smoothing factor α , as shown in Equations (3.37) and (3.38).

$$\tau = \frac{-h}{\ln(\alpha)} \quad (3.37)$$

$$\frac{\omega}{\omega_{unfiltered}} = \frac{\frac{1}{\tau}}{s + \frac{1}{\tau}} \quad (3.38)$$

To define the speed controller gains, a simplified motor model was used. As the torque controller is much faster than the speed dynamic, it is assumed to be ideal, without delay. Thus, the speed is only dependant on the motor torque (T_e), mechanical losses (T_{loss}), the external load (T_{load}), and the system inertia (J), as shown in Equation (3.39).

$$\frac{d\omega_{unfiltered}}{dt} = \frac{T_e - T_{load} - T_{loss}}{J} \quad (3.39)$$

Using the Laplace transform the transfer function is given by Equation (3.40).

$$\frac{\omega_{unfiltered}}{T_e} = \frac{1}{Js} - \frac{T_{load} + T_{loss}}{JT_e s} \quad (3.40)$$

Assuming the external load, and the mechanical losses as disturbances, the model can be reduced to a first-order system, shown in Equation (3.41).

$$\frac{\omega_{unfiltered}}{T_e} = \frac{1}{Js} \quad (3.41)$$

Combining the motor model with the exponential moving average, a transfer function for the system can be derived, as shown in Equation (3.42).

$$H(s) = \frac{\omega}{T_e} = \frac{1}{\tau Js^2 + Js} \quad (3.42)$$

The controller is defined as a PI controller, thus its transfer function is given by Equation (3.43).

$$C(s) = k_p + \frac{k_i}{s} \quad (3.43)$$

The closed-loop transfer function from reference speed to filtered speed is then given by Equation (3.44), while the transfer function from reference speed to actual speed is presented at Equation (3.45).

$$\frac{\omega_{measured}}{\omega_{ref}} = \frac{C(s)H(s)}{1 + C(s)H(s)} = \frac{k_p s + k_i}{s(Js^2(\tau + 1) + Js^2)} \quad (3.44)$$

$$\frac{\omega_{real}}{\omega_{ref}} = \frac{(k_p s + k_i)(s\tau + 1)}{J\tau s^3 + Js^2 + k_p s + k_i} \quad (3.45)$$

With the transfer function defined, the controller gains can be adjusted to define a critically damped system, with a fast response time. For the testbench used in the experimental validation that has an inertia of approximately 185gcm^2 , the controller gains were defined as $k_p = 0.035\text{Nm/RPM}$ and $k_i = 10^{-9}\text{Nm/RPM}$, with the smoothing factor $\alpha = 0.8$. The resulting root locus plot is shown in Figure 3.23, where the poles are located at -3984.8 , -3602.0 , and 0 .

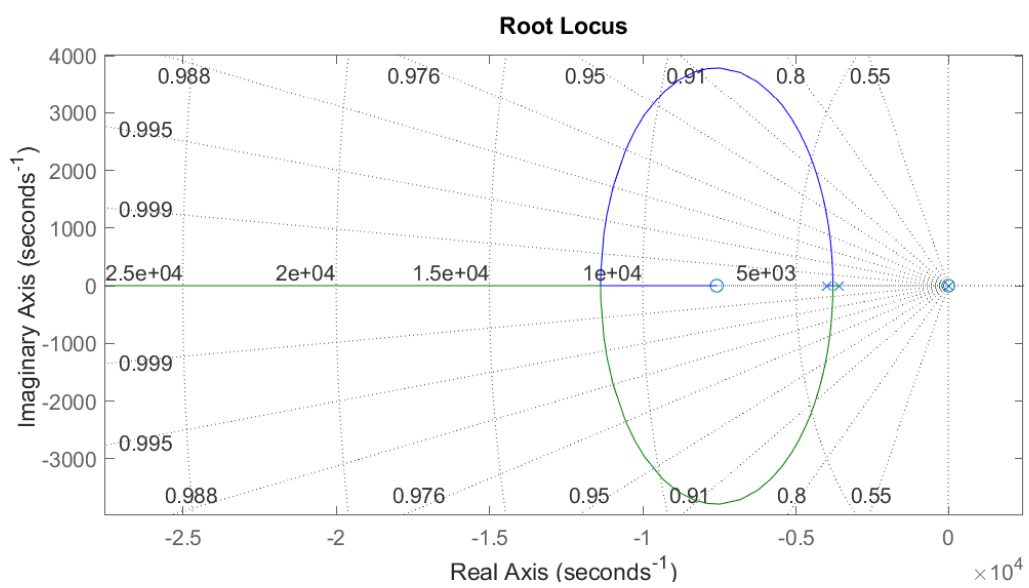


Figure 3.23: Root locus plot for the the closed loop system.

Chapter 4

Simulation and Experimental Results

Contents

4.1 Simulation	45
4.1.1 Baseline Step	46
4.1.2 Current THD	48
4.1.3 Robustness	49
4.1.4 Acceleration Event	50
4.2 Experimental Results	51

4.1 Simulation

To accelerate the development time, a model was developed in *Simulink*, allowing for faster prototyping and direct comparison of the methods in a controlled environment. An adaptation of the *Simscape Specialized Power Systems* block *Permanent Magnet Synchronous Machine* was made to convert it to a delta-wound machine and to accept variable inductances as in Equation (2.29). This model was combined with six MOSFETs blocks in three legs to simulate the VSI. To supply the MOSFETs, a model of the battery was made, where an ideal voltage source is connected through a series resistor to the DC link, where a capacitor stabilizes the voltage. In Figure 4.1 the resultant system is presented, where S_1 , S_2 , S_3 , S_4 , S_5 , S_6 , are the gate control signals that come from the control strategy.

The parameterization of the MOSFETs used in the simulation is derived from the model used in [5], the Wolfspeed C2M0040120D. The motor model is the one derived on Section 2.3, with the parameters from Section 3.1. The rotor position is based on Heidenhain ECI1118 properties as this is the encoder that the manufacturer uses. The DC link capacitor is set to $40\mu F$, while the battery series resistance is 0.03Ω , both based on the existing hardware. The ground connections are $420k\Omega$ each, to simulate the isolation between high voltage and low voltage in the car, while the inertia and torque source blocks inside the motor area are to simulate the testbench environment, with the standard value of $0.0848kgm^2$.

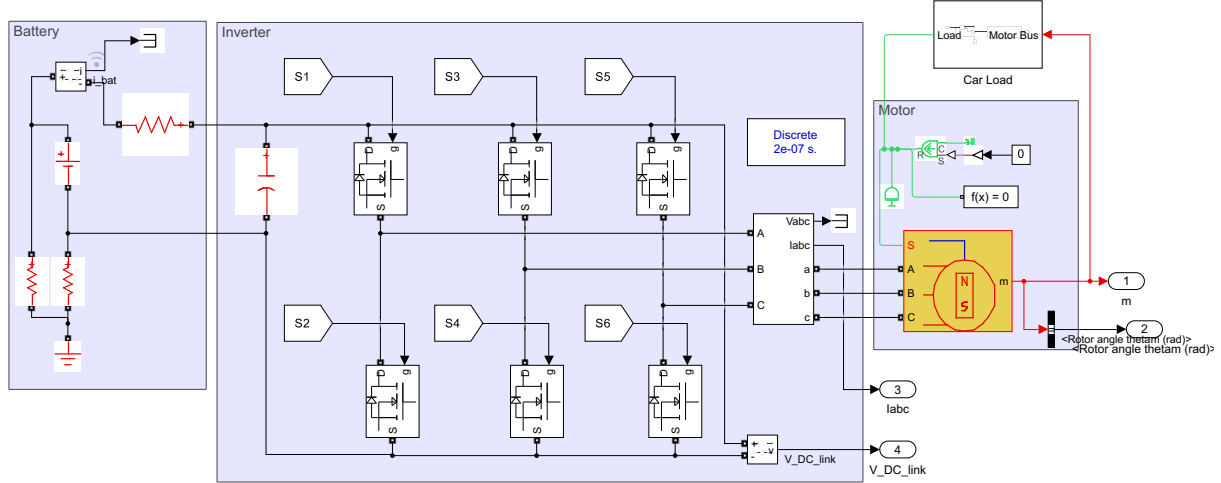


Figure 4.1: Simulink Models, Motor and Inverter.

to the inertia, and the torque source being controlled to maintain a constant speed. All those parameters are shown in Table 4.1 alongside the car parameters used in the load simulation on Section 4.1.4.

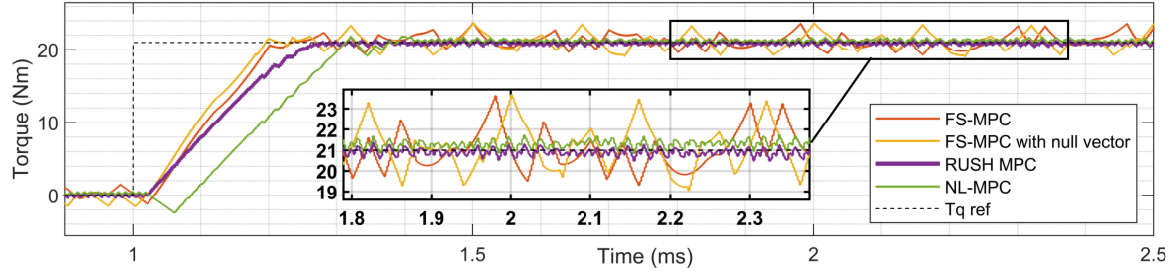
Table 4.1: Simulation Parameters

Simulation timestep	$0.2\mu s$	Car mass	$230kg$
DC Link Capacitor	$40\mu F$	Pilot mass	$60kg$
Battery Series Resistance	0.03Ω	Tire radius	$0.23m$
Ground Connection	$420k\Omega$	Wheel assembly moment of inertia	$0.2kgm^2$
Testbench Inertia	$185gcm^2$	Gear ratio	15.21
MOSFETs	Wolfspeed C2M004120D	Air density	$1.2kg/m^3$
Switching Frequency	$50kHz$	Reference car area	$1m^2$
Encoder Resolution	18 bits	Drag coefficient	1.59
Encoder Frequency	$12.5kHz$	Rolling resistance coefficient	0.09
Current and Voltage Sensor Resolution	14 bits	Speed Controller proportional gain (k_p)	$0.035Nm/rpm$
Current and Voltage Sensor Frequency	$50kHz$	Speed Controller integral gain (k_i)	$10^{-9}Nm/rpm$

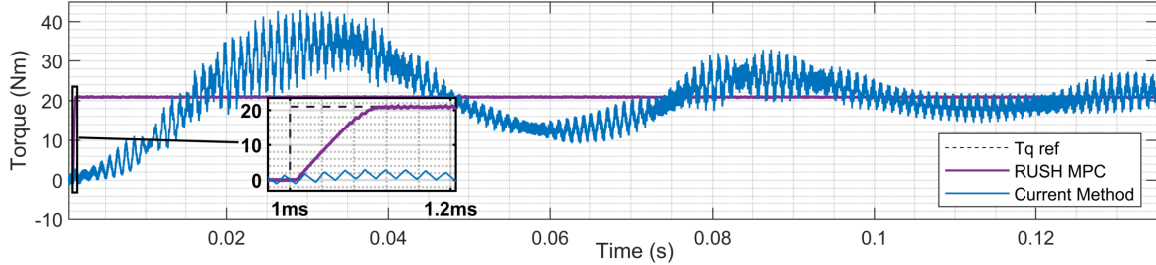
4.1.1 Baseline Step

With the model implemented on *Simulink*, a baseline was made using the manufacturer control scheme, FOC with the standard $8kHz$ switching frequency, and compared with the proposed methods at $50kHz$. The difference in frequency is to account for the complete system, where the use of wide bandgap semiconductors allowed for a faster switching frequency. The baseline profile is a positive torque step with the machine fixed at the nominal speed of $12kRPM$. The rising time of each method is

shown in Figure 4.2.



(a) MPCs comparison. In orange the Finite set MPC, in yellow the finite set MPC with null vector, in green the continuous set implicit MPC, and in purple the proposed continuous set explicit MPC.



(b) Proposed method (in purple) vs Currently used method (in blue).

Figure 4.2: Control methods comparison in a torque step.

Note that the predictive controllers all perform similarly, having a great dynamic response, with an average rising time (0 to 100%) of $200\mu s$, while the FOC method performed much slower, at approximately $180ms$. While the rising time in the FOC can be improved by better tuning the PID (these results are with the values recommended by the manufacturer), it would result in more pronounced overshoots and settling time, and would not reach the performance of a predictive controller, where the torque rising is only limited by the machine inductances, which shows the great dynamic performance of predictive controllers. It is important to also notice a small delay in the implicit NL-MPC response, this delay is due to the solver failing to converge. Although this may not always occur at each reference torque step, it was intentionally left on this graph to remind us of the possibility of this event.

Divergence among the proposed methods becomes apparent during the analysis of steady-state conditions. The basic FS-MPC stands out with the highest torque and current ripple, significantly worse than the baseline, rendering it impractical. This ripple is due to the absence of a modulator, thus the chosen vector will stay applied for the full sampling time. Although an increase in switching frequency would improve the absolute performance of this method, in comparison it would never be as smooth as a modulated control, as it uses discrete vector options, while a simple SVM would switch multiple times in a single period. The increased switching reduces the ripple at the cost of lowered efficiency due to switching losses.

The addition of the null vector on the second method reduces the ripple at low angular speeds but still fails to do so when the machine accelerates, with curves very similar to the FS-MPC. The use of complete modulators can reduce this torque ripple problem, as the SVM allows for a third vector to be applied during the same time step, allowing the control to accurately point the voltage vector to the desired angle and amplitude, where the null vector only lets the controller change the amplitude of the

existent active vectors.

4.1.2 Current THD

The distortion of currents was evaluated by setting the motor at a constant speed, waiting a few periods for it to reach a steady state and then calculating the average THD of all line currents through 5 electrical periods. This was repeated in a grid pattern with some of the results shown in Table 4.2.

Table 4.2: Control Method Current THD comparison. THD is calculated until the Nyquist frequency, that is 250kHz and 40kHz for the controllers running at 50kHz and 8kHz respectively.

		1000 RPM	7333 RPM	13666 RPM	20000 RPM
FOC @8kHz	1Nm	57.62%	43.44%	207.54%	29.62%
	11Nm	3.22%	10.62%	12.14%	58.53%
	20Nm	5.15%	6.50%	10.18%	37.08%
FOC @50kHz	1Nm	56.95%	11.08%	14.12%	4.71%
	11Nm	2.18%	2.19%	1.93%	4.85%
	20Nm	1.41%	1.41%	2.28%	3.86%
FS-MPC @50kHz	1Nm	696.41%	566.94%	247.13%	72.31%
	11Nm	39.42%	30.17%	28.04%	11.82%
	20Nm	22.10%	16.88%	8.52%	11.82%
FS-MPC Null Vector @50kHz	1Nm	30.67%	120.31%	159.20%	221.12%
	11Nm	1.59%	10.65%	12.40%	11.51%
	20Nm	1.76%	6.43%	7.10%	8.54%
NL-MPC @50kHz	1Nm	6.59%	9.98%	12.60%	14.50%
	11Nm	0.81%	1.48%	1.89%	2.17%
	20Nm	0.81%	0.96%	1.18%	1.12%
RUSH MPC @50kHz	1Nm	7.20%	11.91%	16.82%	21.95%
	11Nm	0.76%	1.47%	1.92%	2.16%
	20Nm	0.81%	0.98%	1.19%	1.12%

Table 4.2 exposes the advantage of continuous MPC over the other alternatives, with distortions expressively smaller than the baseline and the finite set MPCs, backing up the ripple analysis previously made. As expected the addition of a null vector reduced expressively the THD in operation points of low modulation index, but made no difference when the modulation index increased. When comparing the methods that use SVM, the distortion is very similar when operated at the same frequency, meaning that the main factor is the modulation frequency, not the control algorithm.

Another advantage of the proposed methods is they actively use the direct axis current to generate torque throughout the full operation map of the motor, not only in field weakening as the method currently implemented on the car. This is a result of the use of MTPA references which improves efficiency, as it produces a reduction in the current vector modulus necessary to generate the same torque.

4.1.3 Robustness

To test the controller's robustness, a Monte Carlo analysis is proposed. A normal distribution is assigned to the motor parameters with a mean equal to the characterized value, and a standard deviation equal to 5% of the mean. The step of Figure 4.2 was simulated for 1000 samples with the modified parameters applied to the motor without updating the controller (Figure 4.3).

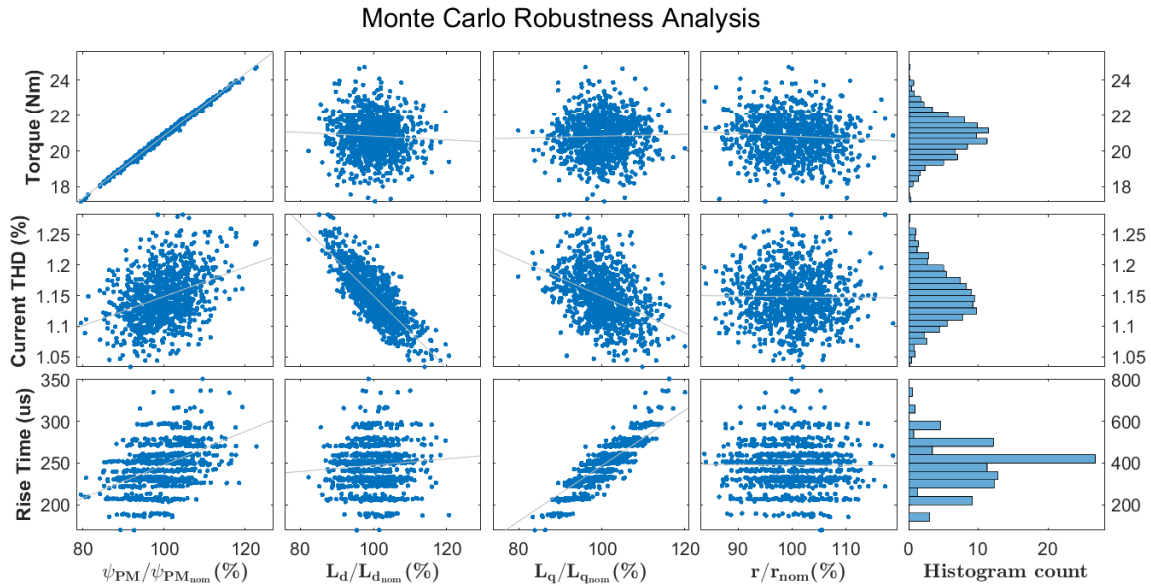


Figure 4.3: Monte Carlo Robustness Analysis. The motor parameters are shown in percentual change from the controller's expected value.

To evaluate the performance with degraded parameters three metrics were used, the steady-state mean torque, the steady-state current THD, and the torque rising time. Based on these metrics the most influential parameter is the flux linkage, with a correlation of almost 100% with the steady-state torque as shown in Figure 4.4. This is explained by the type of motor used, where the inductances between the direct and quadrature axes are very similar, resulting in most of the torque derived from the permanent magnet's flux linkage. Note that this dependency is also present in the method currently used by the team, where the quadrature current reference is based on the machine torque constant (k_t). While relatively easy to characterize, the flux linkage is also the parameter most prone to change with the life of the motors, where the magnets can overheat or be demagnetized by a high direct axis current, thus a good approach is to develop a characterization routine that can be automatically executed whenever the user deems necessary.

The quadrature inductance has a higher correlation with the torque rise time, as expected. Since almost all of the torque is derived from the permanent magnet's flux linkage the torque will rise as fast as the controller manages to create quadrature currents. While this correlation is not definitive proof, it reinforces the statement that the proposed controller dynamic response is limited by the machine inductances. The high flux linkage correlation with the rise time is due to the increase in steady-state torque since with higher flux the steady-state torque is higher and the rise is approximately linear, with an increase in steady-state torque the rise time also increases.

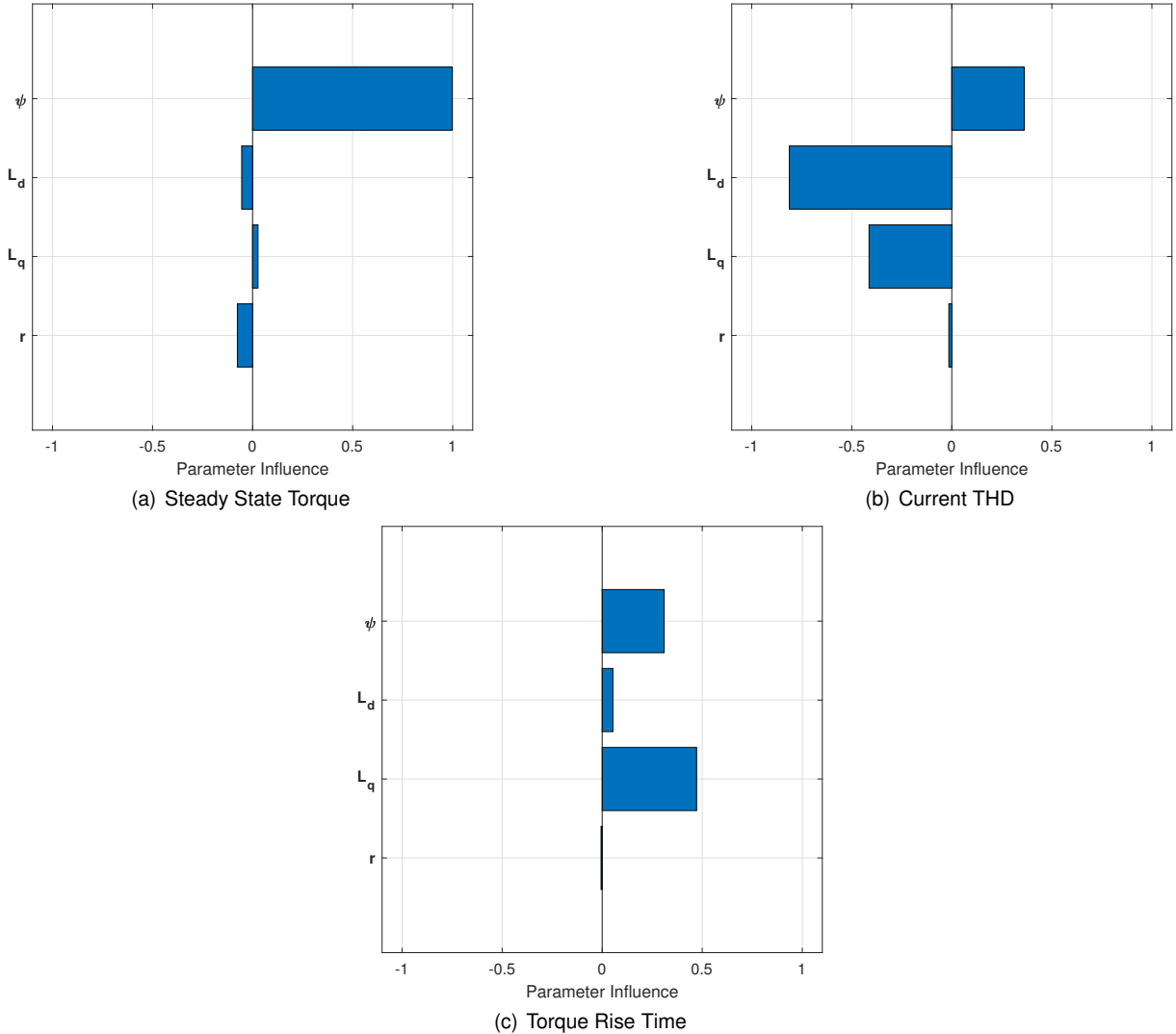


Figure 4.4: Parameter correlation coefficient with performance metrics.

Regarding the current THD, the parameter influences are well balanced, with the direct axis inductance being a little more correlated. When combining this with the small absolute variance of the THD, it is clear that the control strategy is very robust against model mismatches, maintaining a low distortion even with the wrong parameters.

4.1.4 Acceleration Event

The load profile defined in Section 3.3 was used to simulate a typical acceleration event. The car load parameters are as shown in Table 4.1, and the torque reference was set to reach 21.3kW of delivered power (after inverter and motor efficiency losses). The power value was chosen assuming an 80% powertrain efficiency and the previous approximation of one-third of the car load on the rear motors. As shown in Figure 4.5, the EMPC improved the time from 3.943s to 3.883s (1.6%), reaching also a higher top speed than the currently implemented control method and presenting a lower torque ripple.

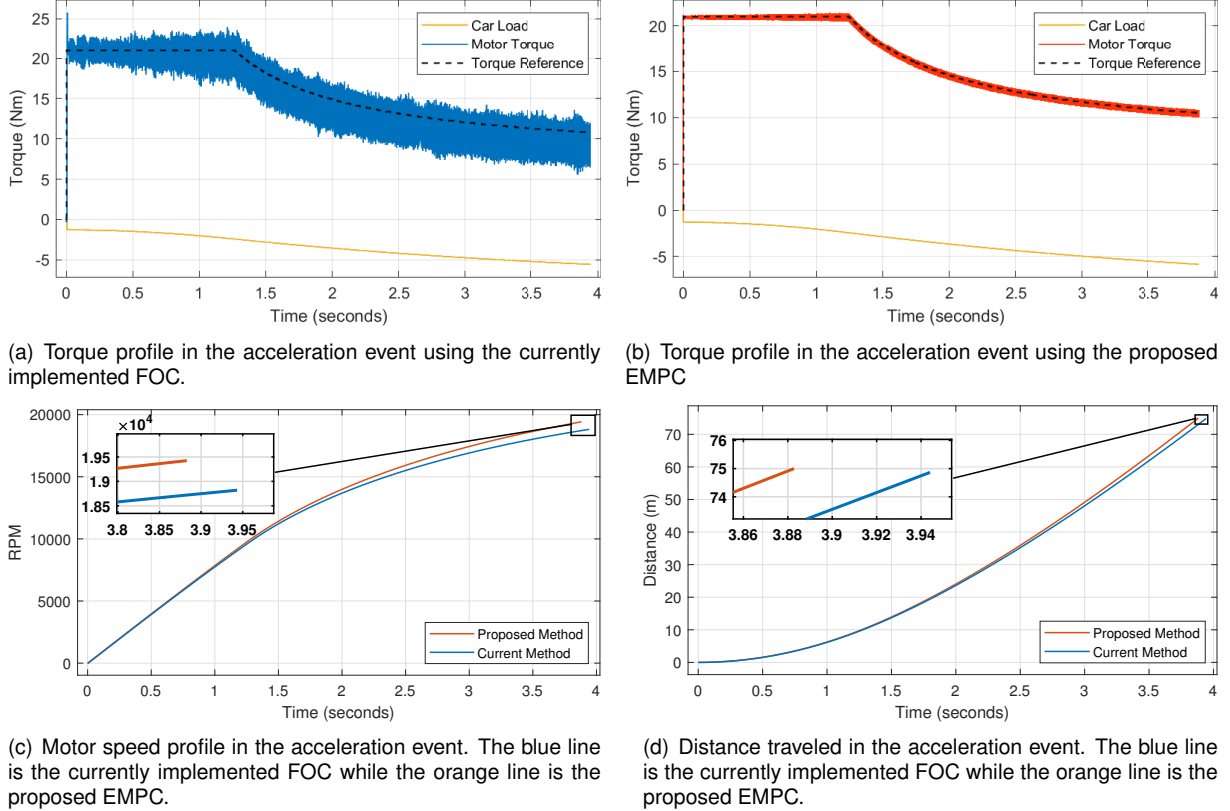


Figure 4.5: Control methods comparison on an Acceleration event.

4.2 Experimental Results

To validate the simulated results, some tests were made on a test bench. The Real-time Ultra Short Horizon extension MPC (RUSH MPC) was implemented using Xilinx Model Composer inside Simulink, compared with the simulation implementation and then generated for the Field Gate Programmable Array (FPGA) present in a Digilent Zybo Z7-20. The hardware used was comprised of the inverter developed on [5], coupled with a current measuring board, developed for this thesis to increase noise immunity. This pairing was supplied with a power supply by Elektro-Automatik (EA-PSI 8360-15 DT) capable of up to 1.5kWh, and the characterized AMK motor was set in a test bench with a Sensor Technology torque transducer (RWT441-EC-PG) and another AMK motor as load. The complete setup is shown in Figure 4.6.

The inverter used in the experimental setup was a limiting factor due to the chosen semiconductors not being able to handle the maximum motor current. This limitation was explained in [5], where it was mentioned that the intended mosfet was not available, thus an alternative semiconductor had to be used. The evolution of the SiC semiconductors since the previous design was also noticeable, going from a second SiC mosfet generation to a fourth, improving reliability and efficiency. Those limitations, combined with the advances in the SiC semiconductors industry exposed the need for a new hardware version. Even though this work focuses on the controller development, not the hardware, a new inverter

design was made, covering the limitations of the current one. This new inverter design was not ready for the experimental tests, but a brief chapter on the design process is included in Appendix D.

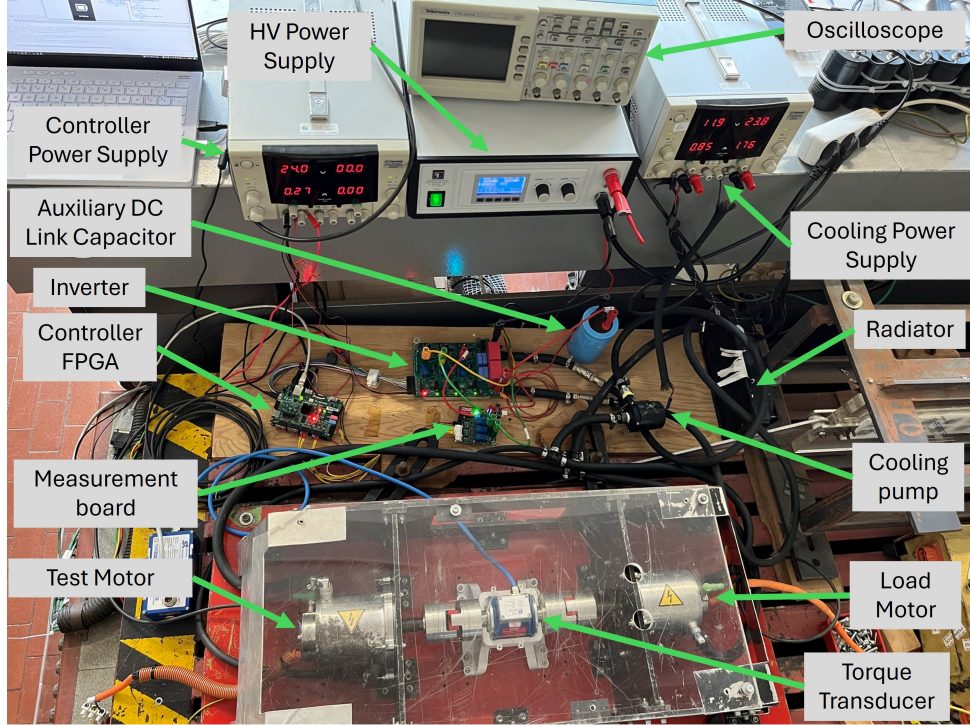


Figure 4.6: Testbench setup.

First, a simple constant torque test was made to evaluate if the model was correctly calculating the generated torque. Figure 4.7 presents the torque estimated based on the motor parameters and the current measurements with the value measured with the ST transducer output. The current measurement from the developed measurement board had some outliers from EMI, so the currents and torque in this section were filtered using a moving median (8 samples) and if the sample is further than 2 Median Absolute Deviation (MAD), then it is considered an outlier, thus it is replaced by the average of the closest 2 points.

The estimated torque is constantly smaller than the measured torque, with a difference of 0.5Nm. This difference is due to the motor parameters not being perfectly matched with the real motor, and the current measurements not being perfect. The difference between the estimated and measured torque is small enough to consider the model valid for the next tests.

With the torque estimation validated, the next step was to verify the currents on a steady state test, ideally, this would be done with nominal torque, but due to a limited maximum inverter current the motor was commanded to keep a constant torque of 7Nm. To create a load, another motor was connected to the shaft and the motor phases were short-circuited, creating a load torque that changes with the speed, this resulted in the speed stabilizing at 269RPM. The current was measured with the developed measuring board and with an oscilloscope probe (ELDITEST CP6550), while the torque was estimated by the control algorithm and compared with the simulation results. The simulation results were obtained by running the same model used for the controller implementation, with the same parameters and inputs.

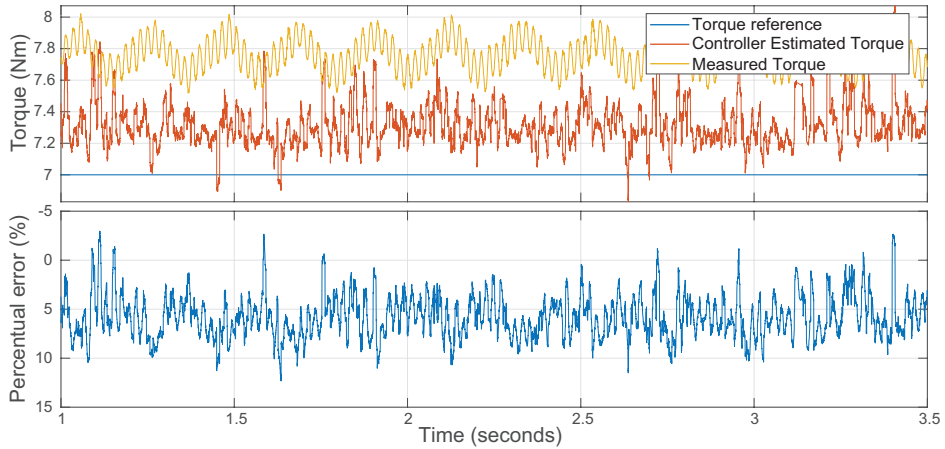
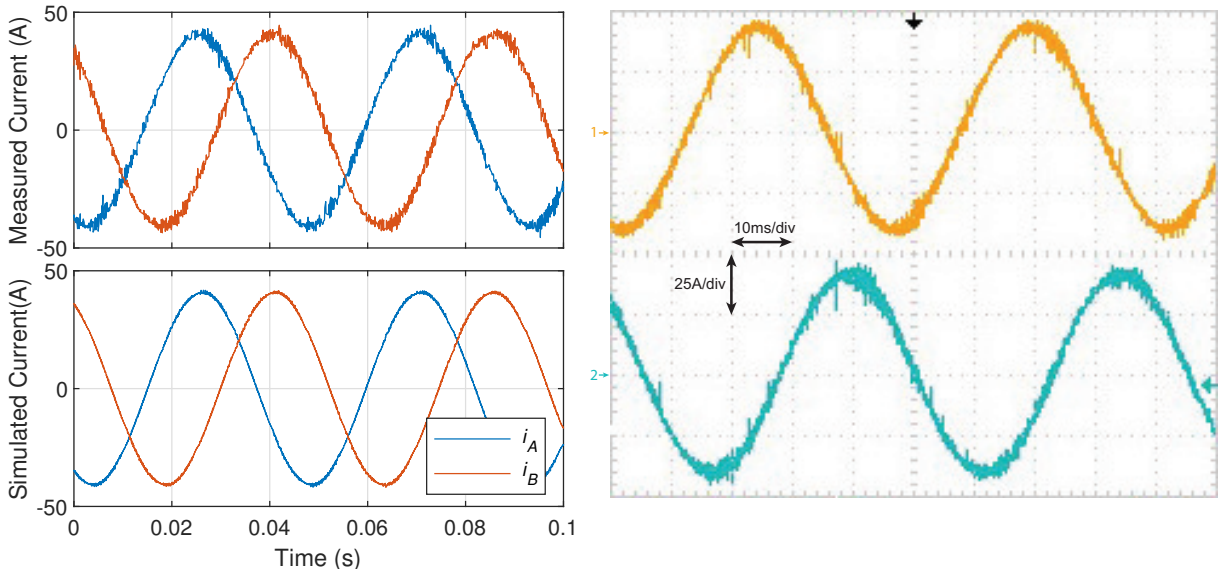


Figure 4.7: Torque estimation vs Measured. At the bottom, the percentual error between the measured and estimated torques is shown.

The results are presented in Figure 4.8.



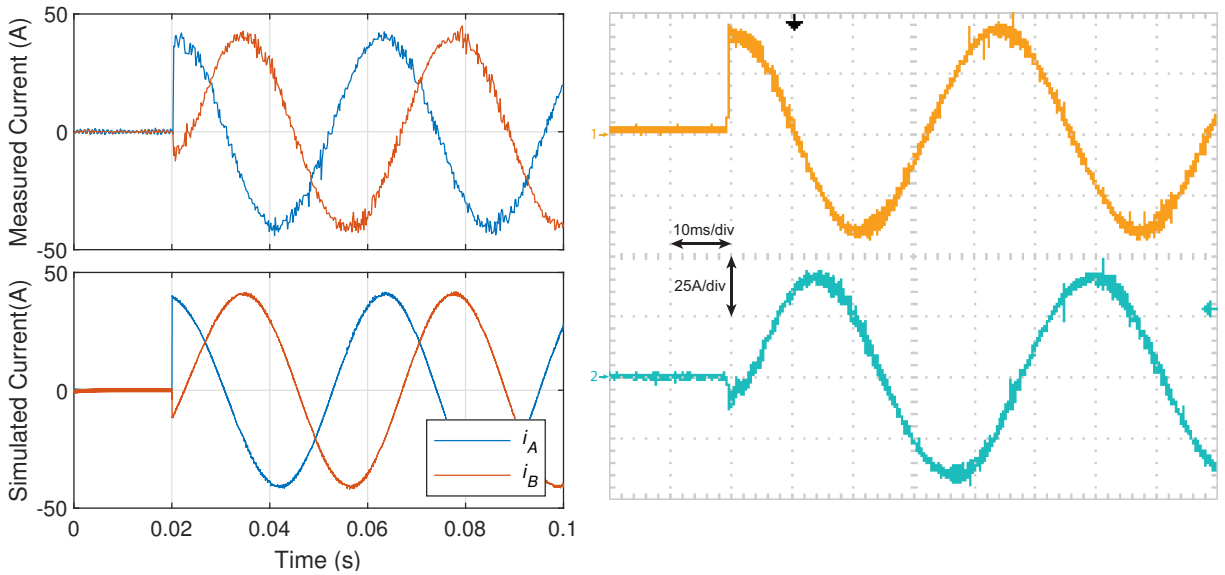
(a) Measurement Board and Simulation measurements. (b) Oscilloscope measurements. Channel 1 (in yellow) represents the plot on top present values from the measurement board, the line A current, while channel 2 (in blue) is the line B current while the bottom plot is from the simulation.

Figure 4.8: Line currents measurements at steady state. Torque reference at 7Nm and rotor speed stable at 169RPMs.

The oscilloscope measurement was made with a probe that has a sensitivity of $20mV/A$. The results show that the current measured by the developed board is identical to the one from the oscilloscope probe, proving the system's accuracy. When comparing the measured currents with the simulation results, although they have the same form and amplitude, it is clear that the simulated curve is cleaner. This is backed by the THD comparison, where the measured current has a THD of 2.44% and the simulated current has a THD of 0.47%, both of them calculated to the 50th harmonic. This difference is

due to inaccuracies in the measurements and parametrization.

Then a torque step response was applied with the motor at a standstill and with the same load as the constant current test. Once again it would be a good approach to use the nominal values but the inverter was a limitation so a reference of $7Nm$ was used. The currents presented in Figure 4.9 show an almost instantaneous dynamic response, transitioning to the specified amplitude without noticeable distortions. The oscilloscope currents are also very similar to the ones measured by the developed board, with the same form and amplitude. The simulation results are very similar to the measured ones, with the same form and amplitude, but the simulation is cleaner. The difference between the measured and simulated currents is small enough to consider the model valid.



(a) Measurement Board and Simulation measurements. (b) Oscilloscope measurements. Channel 1 (in yellow) represents the line A current, while channel 2 (in blue) is the line B current. The plot on top presents values from the measurement board, while the bottom plot is from the simulation.

Figure 4.9: Line Current measurements with a reference torque step from 0 to $7Nm$ at $0.02s$.

Figure 4.10 shows the torque dynamic response to the step. The reduced sampling time creates significant uncertainty in the measurement, but it is possible to state that the torque rise time is less than 200 microseconds, which is a great improvement when compared with the current control method. The simulation results have a greater sampling rate showing that the rise time is smaller than 100 microseconds. An improved sampling frequency would allow for a better comparison between the simulation and experimental results.

To compare the performance of the proposed method, a torque step was also applied to the current solution of the inverter and control strategy. The results presented in Figure 4.11 show that as expected, the current solution is much slower than the proposed method, with a rising time of $30ms$ and a delay of $10ms$. When compared with the simulated values in Figure 4.2 a difference can be seen in the overshoot value of the current method, which is not present in the experimental results. That is due to the gains used on the PI current controller, which are not as aggressive as the ones used in the simulation. This

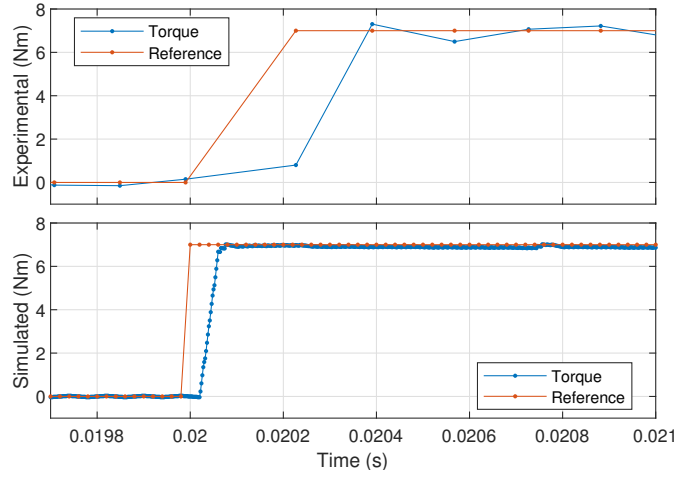


Figure 4.10: Torque reference following with a step from 0 to 7Nm . The upper plot presents the experimental data, while the bottom plot is from the simulation

also resulted in a slower rising time, as in the simulation it reached the 10Nm mark in half the time as the experimental results.

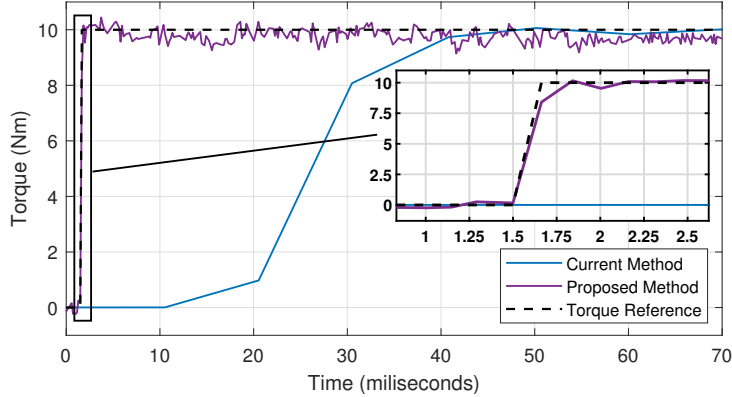


Figure 4.11: Comparison of torque step response between the proposed method and the currently implemented method.

The torque step response was repeated for several reference torque values, from 1 to 10Nm , to evaluate the tracking capabilities of the controller. The results presented in Figure 4.12 show that the RUSH MPC is capable of tracking the reference torque independently of its magnitude. The rising time stayed constant throughout the steps, being smaller than the sampling time of $157\mu\text{s}$. It can also be seen that there is not a pronounced overshoot.

To test the speed controller, an RPM step was applied with the motor at standstill and without load. In Figure 4.13 the rotor speed and the torque are presented. The speed controller was saturated to $\pm 5\text{Nm}$ to avoid overcurrents as the power supply was not able to constantly supply high currents. A small overshoot can be seen in the speed response, this is due to the exponential average filter that was implemented on the RPM measure. The filter reduced the bandwidth of the signal and when combined with high gains in the PI it produced some oscillations which can be improved with a less aggressive filter and a better-tuned PI controller. The RUSH MPC has great tracking capabilities, as shown by the

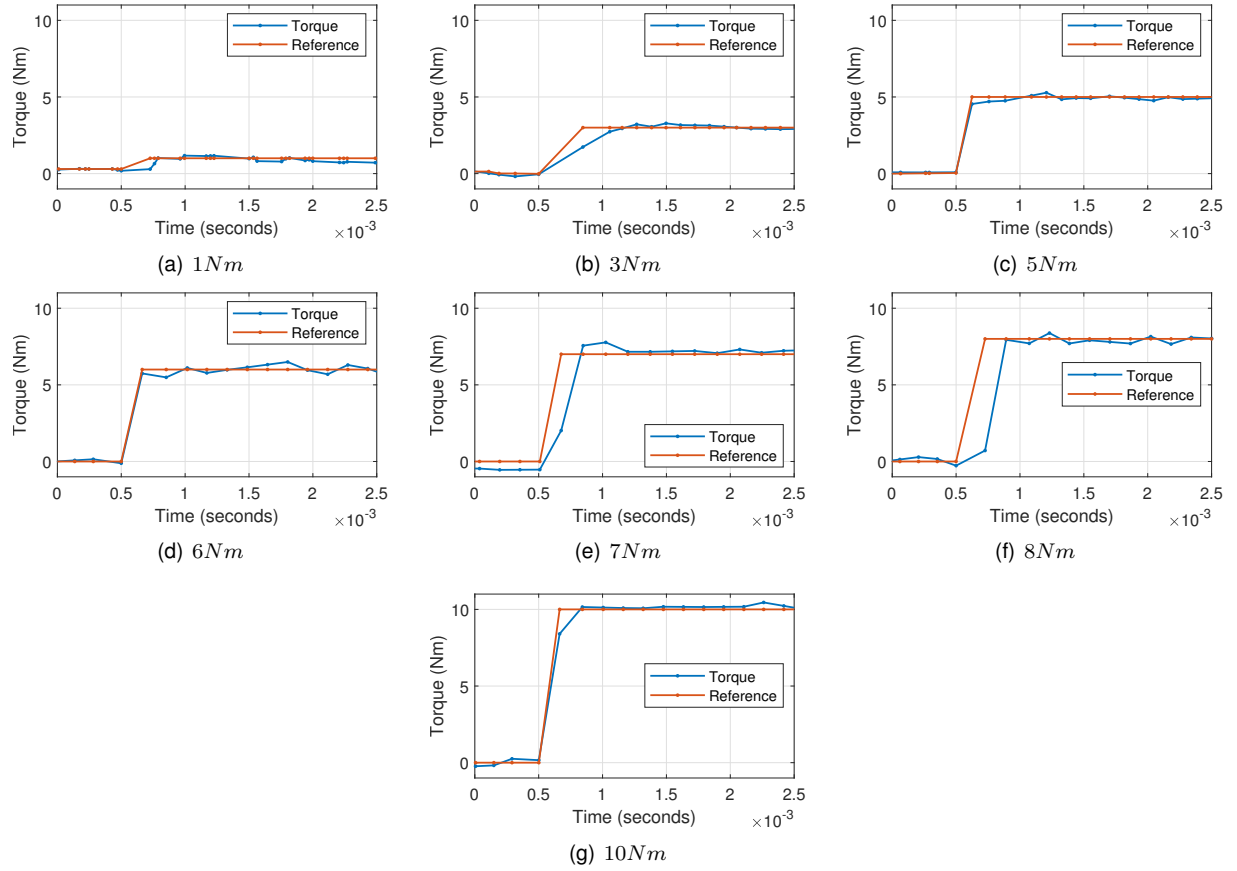
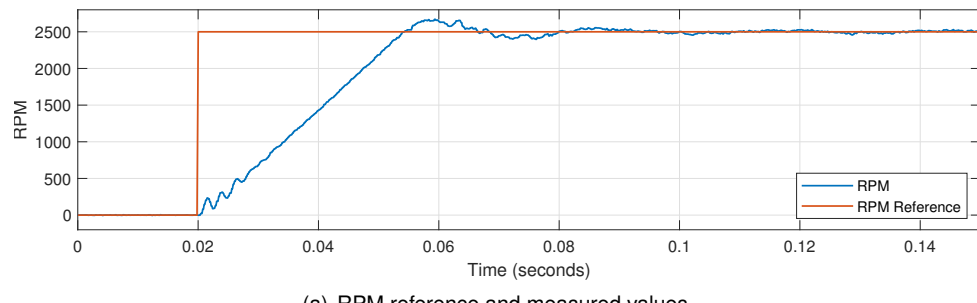


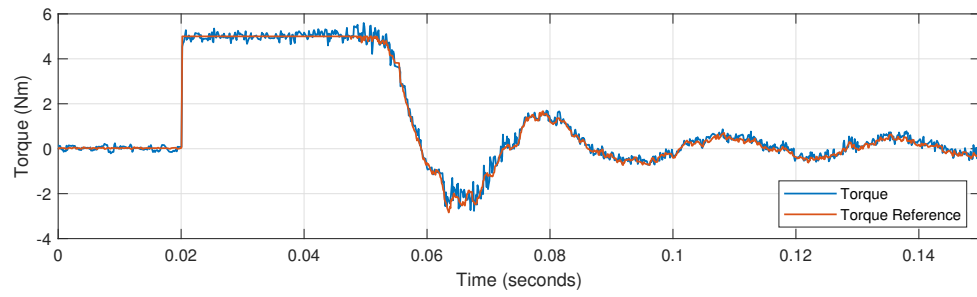
Figure 4.12: Torque step response for different reference torque values.

torque graph, with the estimated torque overlaying the reference torque. The error between the torque reference and the estimated torque is shown in Figure 4.13(c), showing an average error of 0.05Nm and a peak error of 0.9Nm .

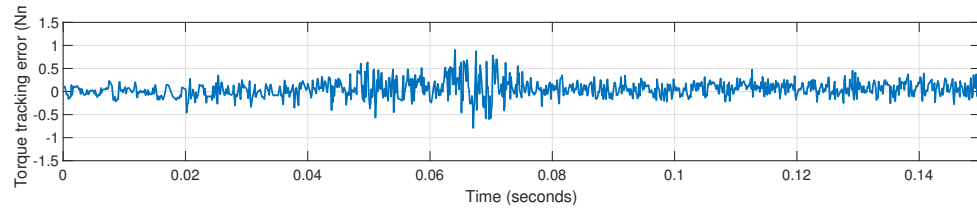
A torque profile to simulate the driver's input was also tested and is presented in Figure 4.14. The controller fails to output the reference torque around 0.1s due to the power supply not being able to provide enough current, thus it switched from constant voltage to constant current output, reducing the available voltage to the inverter. Aside from this, the controller was able to follow the torque reference with a small error, averaging 0.04Nm and peaking at 1.6Nm if the period of the power supply shortage is discarded.



(a) RPM reference and measured values.

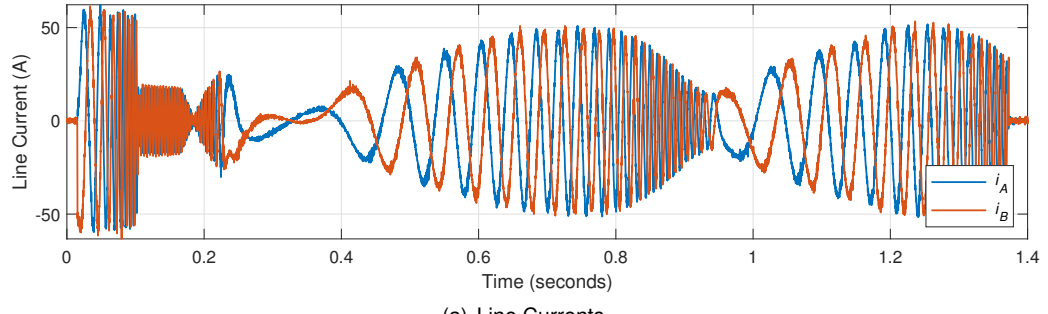


(b) Torque reference and measured values. The torque reference is derived from the speed controller but saturated to $\pm 5 \text{ Nm}$.

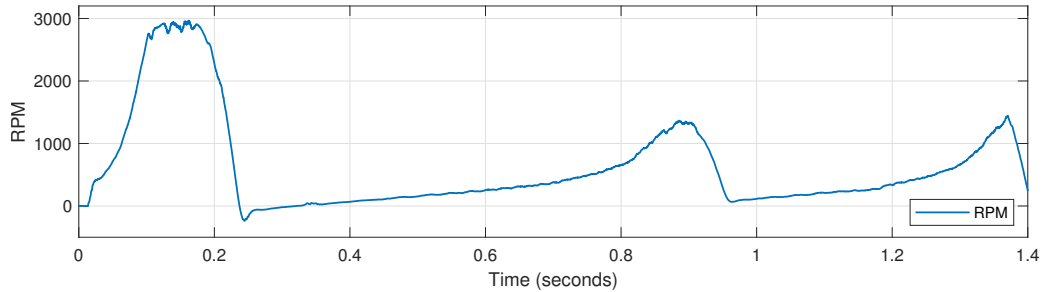


(c) Torque reference tracking error.

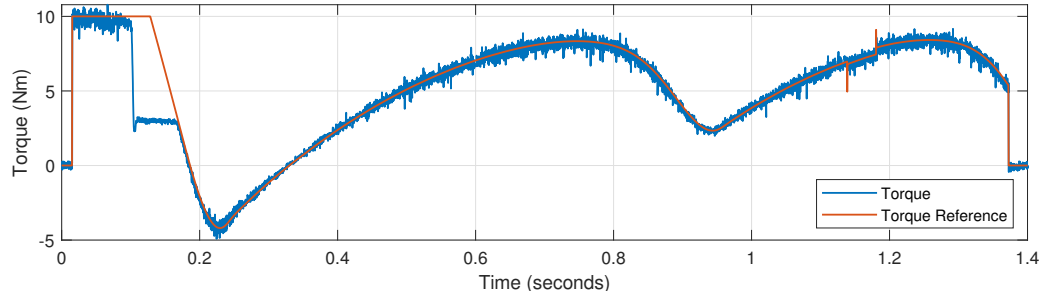
Figure 4.13: RPM step from standstill to 2500RPMs.



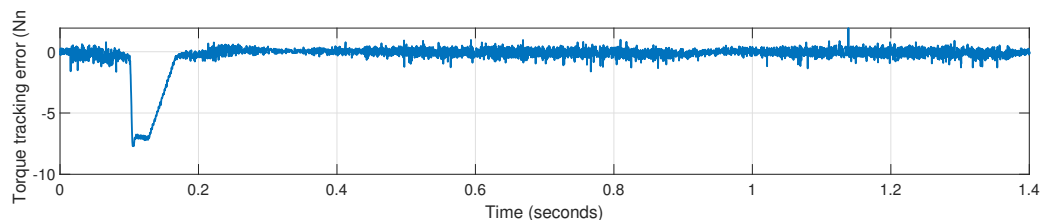
(a) Line Currents.



(b) Rotor speed.



(c) Torque reference and measured values. The torque reference is derived from the speed controller but saturated to $\pm 5\text{Nm}$.



(d) Torque reference tracking error.

Figure 4.14: Pedal torque profile.

Chapter 5

Conclusions

The work developed in this thesis aimed to fill the identified gap in the process of a powertrain developed fully in-house for the FST Lisboa that is the control strategy for the motors. This necessity led to a study of control strategies and motor models that was performed with an emphasis on improving the dynamic response of the motor torque and the system efficiency.

To achieve those goals, the motor was characterized by performing several measurements and tests. This not only provided a plant model to simulate the control algorithms but also provided the Formula Student team of Instituto Superior Técnico with valuable information about their motor characteristics and performance.

With the motor parametrized, it was possible to set up a simulation environment and some control strategies were implemented in it. This allowed a comparison between the different strategies and the selection of the most suitable for the application. The selected strategy was the Real-time Ultra Short Horizon extension MPC (RUSH MPC) due to its fast response, low current ripple, and computational efficiency.

The proposed control was then implemented in an FPGA and the hardware necessary to test the control in a test bench was developed. The motors and inverter were then assembled on a test bench to perform experimental tests. Although the testbench hardware was later verified to be a limiting factor, the experimental results were very promising.

The simulation and experimental results were compared and analyzed showing a close match between them. The torque estimation was also validated and the control strategy was able to control the motor torque with a dynamic response orders of magnitude smaller than the current solution and with a very low torque ripple. The system efficiency was also improved due to the reduction in current THD.

While not exhaustive the developed system continued to build on the great work of the previous thesis and the team's work, creating a solid platform from which the team can continue the work and implement it on the next prototypes. The work done in this thesis was a major step towards the team's goal of developing a fully in-house powertrain.

5.1 Achievements

The major achievement of the present work was the development of a control strategy capable of greatly increasing the dynamic response of the motor while also improving its efficiency. This work showed that by changing the control strategy there are performance gains to be achieved without hardware changes, only by using a control strategy that is tailored to the motor characteristics. The ability to control the currently used motor without any hardware modifications on the motor enables the team to develop its own inverter and control strategy without changing the motor, unlocking major advances in powertrain efficiency, performance, and density. Additionally, it provided some valuable information about the motor characteristics and performance that can be used in future work and at competition design events.

Summing up the achievements of this thesis, the following points can be highlighted:

- The currently used motor is characterized and a simulation environment was created;
- Several MPC strategies were compared with the current FOC solution leading to the selection of the explicit MPC;
- The proposed control strategy was implemented in an FPGA;
- The necessary hardware for a test bench setup was developed and tested to a high level of accuracy;
- Simulation data was validated with experimental results comparison;
- Motor characterization validated by comparing the torque estimation with a commercial transducer;
- System efficiency improved by the reduction of the current THD;
- The torque response was improved by orders of magnitude compared to the current solution.
- A new inverter was designed to overcome the limitations of the current one.

5.2 Future Work

One of the major setbacks of this work was the test bench hardware, which was later verified to be a limiting factor. The used setup was not able to properly align the motor shafts and the transducer, leading to eccentricity-induced vibrations. Those vibrations not only caused some torque oscillations in the experimental results but also limited the tested maximum speed. The test bench hardware should be redesigned to allow for a proper alignment of the motor shafts and the transducer, allowing for higher speeds and more accurate results.

The inverter used was also deemed a limitation, as it was developed to a maximum current of 90A, limiting the maximum torque that could be applied to the motor. A revision of the inverter was developed, but time constraints impeded it to be tested. The new inverter should be tested to verify if the limitations

of the current inverter are overcome and to verify if it meets the efficiency and performance requirements of the team. Some design aspects of the inverter should also be revised, such as the thermal design of the components, and the DC link capacitance, which could be reduced to save space and weight. The voltage measurement circuit should also be revised to include filters and improve the EMI immunity of the system.

Regarding the motor characterization, the inverter limitations did not allow for a full current range characterization of the inductances, which could be performed in the future. The current reference maps should also be updated with the maps generated using the characterization inductances, to replace the ones that used the manufacturer's data.

A proper study of the tradeoff between the reduction of the current THD by increasing the switching frequency and the losses in the inverter and motor derived from such increase should be performed. An optimal point should be found to maximize the efficiency of the system.

A known drawback of the chosen strategy is the dependence on a good model of the system. A calibration routine should be developed to allow for the controller to automatically adjust the model parameters to the real system. Another alternative is the development of a real-time parameter identification algorithm to adjust the model parameters in real-time, but this would require the current references to be solved in real-time, similar to the work done in [42].

The current implementation uses the rotor speed to estimate the current position of the rotor in between encoder readings, which is a known limitation of the system. A better approach would be to use the MPC predictions to estimate the rotor position, which would also benefit from a load torque observer, to improve the velocity and position predictions.

The proposed speed controller although capable of controlling the motor speed, could be improved, as it was not the focus of this work. It could be incorporated into the MPC controller and account for the load torque estimation to preemptively adjust the torque reference to allow for a more robust control.

Another known limitation is the encoder sampling rate, which is very reduced when compared to the control frequency. That, combined with the elevated level of complexity of the encoder protocol and its scarce documentation, suggests that the encoder should be replaced by a more modern and faster sensor.

Lastly, the current implementation of the FPGA uses almost all the available resources, which limits the implementation of more complex algorithms. It also is currently controlling only one motor, but by pipelining the control, it could control two motors, limited by the number of available GPIOs in the Zynq board. One solution could be to switch the control algorithm from floating point to fixed point, which would require fewer resources and would allow for more complex algorithms to be implemented. Another solution would be to use a more powerful FPGA, which would also enable the control of the four motors in only one FPGA, reducing the cost and volume of the system.

Bibliography

- [1] Y. Wang, O. Lucia, Z. Zhang, S. Gao, Y. Guan, and D. Xu. A review of high frequency power converters and related technologies. *IEEE Open Journal of the Industrial Electronics Society*, 1: 247–260, 2020. ISSN 2644-1284. doi: 10.1109/OJIES.2020.3023691.
- [2] P. Karamanakos, E. Liegmann, T. Geyer, and R. Kennel. Model predictive control of power electronic systems: Methods, results, and challenges. *IEEE Open Journal of Industry Applications*, 1:95–114, 2020. ISSN 2644-1241. doi: 10.1109/OJIA.2020.3020184.
- [3] J. W. Palmour. Energy efficient wide bandgap devices. In *2006 IEEE Compound Semiconductor Integrated Circuit Symposium*, pages 4–7, Nov 2006. doi: 10.1109/CSICS.2006.319904.
- [4] J. G. V. V. Sarrico. Design and implementation of a 20kw, 12000rpm permanent magnet synchronous motor (PMSM) for the IST formula student powertrain. MSc Thesis in Electrical and Computer Engineering, Instituto Superior Técnico, Lisboa, Portugal, June 2017.
- [5] P. M. B. de Sousa Correia da Costa. Compact three-phase sic inverter for the IST formula student prototype. MSc Thesis in Electrical and Computer Engineering, Instituto Superior Técnico, Lisboa, Portugal, October 2018.
- [6] N. Bianchi, P. G. Carlet, L. Cinti, and L. Ortombina. A review about flux-weakening operating limits and control techniques for synchronous motor drives. *Energies*, 15(5), 2022. ISSN 1996-1073. doi: 10.3390/en15051930.
- [7] D. Neacsu. Space vector modulation - an introduction. *IECON*, 01 2001.
- [8] S. Vazquez, J. Rodriguez, M. Rivera, L. G. Franquelo, and M. Norambuena. Model predictive control for power converters and drives: Advances and trends. *IEEE Transactions on Industrial Electronics*, 64(2):935–947, Feb 2017. ISSN 1557-9948. doi: 10.1109/TIE.2016.2625238.
- [9] M. Merzoug and F. Naceri. Comparison of field-oriented control and direct torque control for permanent magnet synchronous motor (PMSM). *International Journal of Electrical and Computer Engineering*, 2(9):1797–1802, 2008.
- [10] F. Korkmaz, I. Topaloğlu, M. F. Çakir, and R. Gürbüz. Comparative performance evaluation of FOC and DTC controlled PMSM drives. In *4th International Conference on Power Engineering, Energy and Electrical Drives*, pages 705–708, May 2013. doi: 10.1109/PowerEng.2013.6635696.
- [11] R. Souad and H. Zeroug. Comparison between direct torque control and vector control of a permanent magnet synchronous motor drive. In *2008 13th International Power Electronics and Motion Control Conference*, pages 1209–1214, Sep. 2008. doi: 10.1109/EPEPEMC.2008.4635433.

- [12] F. Wang, X. Mei, J. Rodríguez, and R. Kennel. Model predictive control for electrical drive systems—an overview. *CES TRANSACTIONS ON ELECTRICAL MACHINES AND SYSTEMS*, 1(3):219–230, Sep 2017.
- [13] Z. Ma, S. Saeidi, and R. Kennel. Fpga implementation of model predictive control with constant switching frequency for PMSM drives. *IEEE Transactions on Industrial Informatics*, 10(4):2055–2063, Nov 2014.
- [14] *DYNASYN synchronous servo motor DD5-14-10-POW-18600-B5*. AMKmotion GmbH + Co KG, 2018.
- [15] F. S. Germany. Formula student rules 2023 v1.1, 2023. URL https://www.formulastudent.de/fileadmin/user_upload/all/2023/rules/FS-Rules_2023_v1.1.pdf.
- [16] *AMKASYN inverter KW26-S5-FSE-2Q*. AMKmotion GmbH + Co KG, 2022. Version 15.
- [17] E. Gurpinar and A. Castellazzi. Single-phase t-type inverter performance benchmark using Si IGBTs, SiC MOSFETs, and GaN HEMTs. *IEEE Transactions on Power Electronics*, 31(10):7148–7160, Oct 2016. ISSN 1941-0107. doi: 10.1109/TPEL.2015.2506400.
- [18] V. Asadzadeh, A. Dastfan, and A. Darabi. Selective harmonic elimination in direct torque controlled permanent magnet synchronous motor drive. *COMPEL-The international journal for computation and mathematics in electrical and electronic engineering*, 38(1):153–166, 2019.
- [19] Microchip. Overmodulation management for field-oriented control of three-phase motors, 2023. URL <https://microchipdeveloper.com/xwiki/bin/view/applications/motors/control-algorithms/3-phase-foc/>.
- [20] F. Briz, A. Diez, M. Degner, and R. Lorenz. Current and flux regulation in field-weakening operation. *Industry Applications, IEEE Transactions on*, 37:42 – 50, 02 2001. doi: 10.1109/28.903125.
- [21] A. Mehrizi-Sani. Advanced modulation techniques for power converters. Master's thesis, University of Manitoba, Winnipeg, Canada, 2007. URL <https://api.semanticscholar.org/CorpusID:58809651>.
- [22] Microchip. Zsm viewer, 2024. URL <https://developerhelp.microchip.com/xwiki/bin/view/applications/motors/control-algorithms/zsm/zsm/zsm-viewer/>.
- [23] G. Marques. *Dinâmica das Máquinas Eléctricas*. April 2002.
- [24] P. Pramod. Circulating current induced electromagnetic torque generation in electric machines with delta windings, 2023.
- [25] D. Ohm. Dynamic model of PM synchronous motors, 2000. URL <http://www.drvetechinc.com/id16.html>. Drivetech Inc., Technical Article.
- [26] R. De Doncker and D. Novotny. The universal field oriented controller. *IEEE Transactions on Industry Applications*, 30(1):92–100, 1994. doi: 10.1109/28.273626.
- [27] *Sensored Field Oriented Control of 3-Phase Permanent Magnet Synchronous Motors Using TMS320F2837x*. Texas Instruments, 2016.
- [28] H. Le-Huy. Comparison of field-oriented control and direct torque control for induction motor drives. In *Conference Record of the 1999 IEEE Industry Applications Conference. Thirty-Forth IAS Annual Meeting (Cat. No.99CH36370)*, volume 2, pages 1245–1252 vol.2, 1999. doi: 10.1109/IAS.1999.

801662.

- [29] T. Matsuo and T. Lipo. Field oriented control of synchronous reluctance machine. In *Proceedings of IEEE Power Electronics Specialist Conference - PESC '93*, pages 425–431, 1993. doi: 10.1109/PESC.1993.471965.
- [30] B. Adhavan, A. Kuppuswamy, G. Jayabaskaran, and V. Jagannathan. Field oriented control of permanent magnet synchronous motor (PMSM) using fuzzy logic controller. In *2011 IEEE Recent Advances in Intelligent Computational Systems*, pages 587–592, 2011. doi: 10.1109/RAICS.2011.6069379.
- [31] G. Buja, D. Casadei, and G. Serra. DTC-based strategies for induction motor drives. In *Proceedings of the IECON'97 23rd International Conference on Industrial Electronics, Control, and Instrumentation (Cat. No.97CH36066)*, volume 4, pages 1506–1516 vol.4, 1997. doi: 10.1109/IECON.1997.664908.
- [32] A. Nasr, C. Gu, X. Wang, G. Buticchi, S. Bozhko, and C. Gerada. Torque-performance improvement for direct torque-controlled PMSM drives based on duty-ratio regulation. *IEEE Transactions on Power Electronics*, 37(1):749–760, 2022. doi: 10.1109/TPEL.2021.3093344.
- [33] N. El Ouanjli, A. Derouich, e. g. Abdelaziz, S. Motahhir, C. Ali, Y. El Mourabit, and M. Taoussi. Modern improvement techniques of direct torque control for induction motor drives-a review. *Protection and Control of Modern Power Systems*, 4, 05 2019. doi: 10.1186/s41601-019-0125-5.
- [34] L. Zhong, M. Rahman, W. Hu, and K. Lim. Analysis of direct torque control in permanent magnet synchronous motor drives. *IEEE Transactions on Power Electronics*, 12(3):528–536, 1997. doi: 10.1109/63.575680.
- [35] F. Niu, B. Wang, A. S. Babel, K. Li, and E. G. Strangas. Comparative evaluation of direct torque control strategies for permanent magnet synchronous machines. *IEEE Transactions on Power Electronics*, 31(2):1408–1424, 2016. doi: 10.1109/TPEL.2015.2421321.
- [36] S. Vazquez, J. I. Leon, L. G. Franquelo, J. Rodriguez, H. A. Young, A. Marquez, and P. Zanchetta. Model predictive control: A review of its applications in power electronics. *IEEE Industrial Electronics Magazine*, 8(1):16–31, 2014. doi: 10.1109/MIE.2013.2290138.
- [37] X. Sun, J. Cao, G. Lei, Y. Guo, and J. Zhu. A robust deadbeat predictive controller with delay compensation based on composite sliding-mode observer for PMSMs. *IEEE Transactions on Power Electronics*, 36(9):10742–10752, 2021. doi: 10.1109/TPEL.2021.3063226.
- [38] R. Errouissi, M. Ouhrouche, W.-H. Chen, and A. M. Trzynadlowski. Robust nonlinear predictive controller for permanent-magnet synchronous motors with an optimized cost function. *IEEE Transactions on Industrial Electronics*, 59(7):2849–2858, 2012. doi: 10.1109/TIE.2011.2157276.
- [39] A. Wijenayake and P. Schmidt. Modeling and analysis of permanent magnet synchronous motor by taking saturation and core loss into account. In *Proceedings of Second International Conference on Power Electronics and Drive Systems*, volume 2, pages 530–534 vol.2, May 1997. doi: 10.1109/PEDS.1997.627416.
- [40] B. Stumberger, G. Stumberger, D. Dolinar, A. Hamler, and M. Trlep. Evaluation of saturation and cross-magnetization effects in interior permanent-magnet synchronous motor. *IEEE Transactions*

- on Industry Applications*, 39(5):1264–1271, Sep. 2003. ISSN 1939-9367. doi: 10.1109/TIA.2003.816538.
- [41] J. D. Barros, J. F. A. Silva, and É. G. A. Jesus. Fast-predictive optimal control of NPC multilevel converters. *IEEE Transactions on Industrial Electronics*, 60(2):619–627, 2013. doi: 10.1109/TIE.2012.2206352.
- [42] S.-Y. Jung, J. Hong, and K. Nam. Current minimizing torque control of the IPMSM using ferrari's method. *IEEE Transactions on Power Electronics*, 28(12):5603–5617, 2013. doi: 10.1109/TPEL.2013.2245920.
- [43] P. Costa, S. Pinto, and F. Silva. A novel analytical formulation of SiC-MOSFET losses to size high-efficiency three-phase inverters. *Energies*, 16:818, 01 2023. doi: 10.3390/en16020818.
- [44] Q. Song, W. Wang, S. Zhang, Y. Li, and M. Ahmad. The analysis of power losses of power inverter based on SiC MOSFETs. In *2019 1st Global Power, Energy and Communication Conference (GPECOM)*, pages 152–157, 2019. doi: 10.1109/GPECOM.2019.8778499.
- [45] *EasyDUAL module FF8MR12W1M1H_B11 Datasheet*. Infineon, https://www.infineon.com/dgdl/Infineon-FF8MR12W1M1H_B11-Datasheet-v00_30-EN.pdf?fileId=8ac78c8c8b6555fe018b72791dec7c06, 02 2023. Version 0.30.
- [46] *EiceDRIVER™ 1ED332xMC12N Enhanced (1ED-F3) Datasheet*. Infineon, https://www.infineon.com/dgdl/Infineon-1ED332xMC12N-Datasheet-v01_02-EN.pdf?fileId=8ac78c8c7ddc01d7017e49e76a311599, 05 2023. Version 1.02.
- [47] *UCC27614 30-V, 10-A Single Channel Low Side Gate Driver Datasheet*. Texas Instruments, <https://www.ti.com/lit/ds/symlink/ucc27614.pdf?ts=1636432512065>, 01 2022.
- [48] *Current Transducer LA 100-P Datasheet*. LEM International, https://www.lem.com/sites/default/files/products_datasheets/la_100-p_e_.pdf, 11 2018. Version 13.
- [49] I. for Interconnecting and I. Packaging Electronic Circuits (Northbrook. *Generic Standard on Printed Board Design: IPC-2221*. IPC, 1998. URL <https://books.google.pt/books?id=nHPFoQEACAAJ>.

Appendix A

Amplitude invariant dq0 PMSM model

Starting with Equation (2.5) and replacing the currents and flux for the ones presented in Equation (2.14) results in Equation (A.1).

$$\begin{aligned} \mathbf{u}_{abc} &= \mathbf{R}_{abc} \mathbf{T}_{(\theta_e)}^* \mathbf{i}_{dq0} + \frac{d(\mathbf{T}_{(\theta_e)}^* \boldsymbol{\psi}_{dq0})}{dt} \\ &= \mathbf{R}_{abc} \mathbf{T}_{(\theta_e)}^* \mathbf{i}_{dq0} + \dot{\theta}_e \frac{d\mathbf{T}_{(\theta_e)}^*}{d\theta_e} \boldsymbol{\psi}_{dq0} + \mathbf{T}_{(\theta_e)}^* \frac{d\boldsymbol{\psi}_{dq0}}{dt} \end{aligned} \quad (\text{A.1})$$

Replacing $\dot{\theta}_e$ with ω_e , and multiplying $\mathbf{T}_{(\theta_e)}^{*-1}$ to the left yields Equations (A.2) and (A.3).

$$\mathbf{u}_{dq0} = \mathbf{R}_{dq0} \mathbf{i}_{dq0} + \mathbf{T}_{(\theta_e)}^{*-1} \omega_e \frac{d\mathbf{T}_{(\theta_e)}^*}{d\theta_e} \boldsymbol{\psi}_{dq0} + \mathbf{T}_{(\theta_e)}^{*-1} \mathbf{T}_{(\theta_e)}^* \frac{d\boldsymbol{\psi}_{dq0}}{dt} \quad (\text{A.2})$$

$$\mathbf{u}_{dq0} = \mathbf{R}_{dq0} \mathbf{i}_{dq0} + \omega_e \mathbf{T}_{(\theta_e)}^{*-1} \frac{d\mathbf{T}_{(\theta_e)}^*}{d\theta_e} \boldsymbol{\psi}_{dq0} + \frac{d\boldsymbol{\psi}_{dq0}}{dt} \quad (\text{A.3})$$

Lastly, calculate the derivative of the transformation as in Equation (A.4), resulting in Equation (A.5).

$$\begin{aligned} \mathbf{T}_{(\theta_e)}^{*-1} \frac{d\mathbf{T}_{(\theta_e)}^*}{d\theta_e} &= \frac{2}{3} \begin{bmatrix} \cos(\theta_e) & \cos(\theta_e - \frac{2\pi}{3}) & \cos(\theta_e - \frac{4\pi}{3}) \\ -\sin(\theta_e) & -\sin(\theta_e - \frac{2\pi}{3}) & -\sin(\theta_e - \frac{4\pi}{3}) \\ \frac{1}{2} & \frac{1}{2} & \frac{1}{2} \end{bmatrix} \begin{bmatrix} -\sin(\theta_e) & -\cos(\theta_e) & 0 \\ -\sin(\theta_e - \frac{2\pi}{3}) & -\cos(\theta_e - \frac{2\pi}{3}) & 0 \\ -\sin(\theta_e - \frac{4\pi}{3}) & -\cos(\theta_e - \frac{4\pi}{3}) & 0 \end{bmatrix} \\ \mathbf{T}_{(\theta_e)}^{*-1} \frac{d\mathbf{T}_{(\theta_e)}^*}{d\theta_e} &= \begin{bmatrix} 0 & -1 & 0 \\ 1 & 0 & 0 \\ 0 & 0 & 0 \end{bmatrix} \end{aligned} \quad (\text{A.4}) \quad (\text{A.5})$$

Thus, the PMSM model in the dq0 frame using amplitude invariant transformation is presented in Equation (A.6). This result is the same as Equation (2.21) with the currents, voltages, and fluxes scaled by a factor of $\sqrt{\frac{3}{2}}$ in the direct and quadrature axis, but in the zero axis some results may vary.

$$\mathbf{u}_{dq0} = \mathbf{R}_{dq0} \mathbf{i}_{dq0} + \omega_e \begin{bmatrix} 0 & -1 & 0 \\ 1 & 0 & 0 \\ 0 & 0 & 0 \end{bmatrix} \boldsymbol{\psi}_{dq0} + \frac{d\boldsymbol{\psi}_{dq0}}{dt} \quad (\text{A.6})$$

Appendix B

Technical Datasheets

The datasheets for the current inverter and motor used in the project are presented in this appendix. The inverter datasheet is an excerpt from the original document with the main characteristics, while the motor datasheet is the full document. More information about the kit is available at the manufacturer's website¹.

¹https://www.amk-motion.com/amk-dokucd/dokucd/en/DokuCD_HTML5_en.htm#projekt/doku_cd_html5/topics/amk_automotive.htm

Motor-Datenblatt motor data sheet

AMK

B.1

AMK Motor Datasheet

Bezeichnung/name

DD5-14-10-POW - 18600-B5

- Formula Student

Datum/date: 27.11.2018

Teile-Nr./part number

A2370DD

Zeichn.-Nr./drawing no.:12703-01260

Motorbeschreibung motor description:

Motorprinzip/motor principle:

synchron

Kühlart/cooling type:

Flüssigkeit 4l/min

liquid 4l/min

Bauform/mounting type:

IMB5

Schutzart/degree of protection:

IP 65

Isolierklasse/insulation class:

F

Leistungsdaten performance data:

Betriebsart/duty type:

S1 dT=100K

Dauerstillstandsmoment/continuous Stall Torque "Mo":

13,8 Nm

Maximales Moment/maximum torque "Mmax":

21 Nm

Bemessungsmoment/rated torque "Mn" (ID32771):

9,8 Nm

Bemessungsleistung/rated power "Pn":

12,3 kW

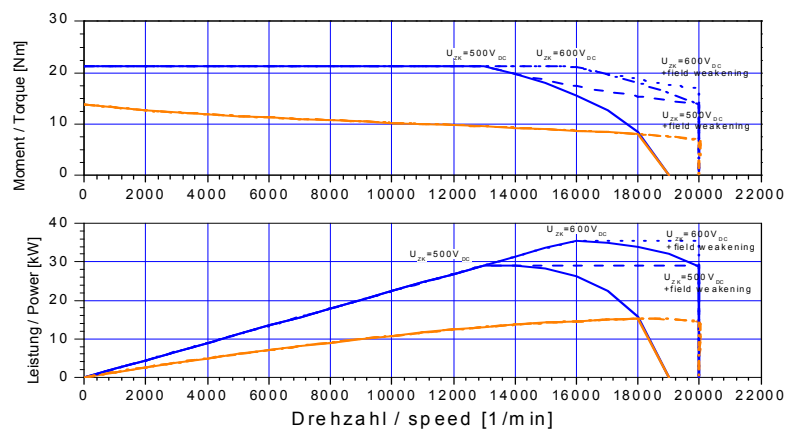
Bemessungsdrehzahl/rated speed "Nn" (ID32772):

12000 rpm

Theo. Leerlaufdrehzahl/theor. no-load-speed "No":

18617 rpm

Motorkennlinien performance - characteristics:



Kennlinie kann die maximal zulässige Drehzahl übersteigen! / Characteristic may exceed mechanical speed limit of motor

Elektrische Daten electrical data:

Nennspannung/rated voltage "Un" (ID32768):

350 V

Nennstrom/rated current "In" (ID111):

41 Arms

Dauerstillstandsstrom/cont. stall current "Io" (ID34096):

53,1 Arms

Maximalstrom/maximum current "Imax" (ID109):

105 Arms

Maximale Dauer für/duration for "Imax" (ID34168):

1,24 s

Drehmomentkonstante/torque constant "kt":

0,26 Nm/Arms

Spannungskonstante/voltage constant "ke" (ID 34234):

18,8 V/kU/min

Schaltung/connection type:

D

Polzahl/number of poles "2p" (ID32775):

10 Pole

Klemmenwiderstand/terminal resistance "Rt" (ID34164):

0,135 Ohm

Klemmeninduktivität/terminal inductance "Ltt" (ID34167):

0 mH

Querachseninduktivität/quadrature axis inductance "Lq" (ID34046):

0,12 mH

Hauptachseninduktivität/direct axis inductance "Ld" (ID34045):

0,24 mH

Magn.-Strom/magn. current "Im" (ID32769):

35 Arms

Magn.-Strom/magn. current "Im1" (ID32770):

0 Arms

Rotorzeitkonstante/rotor time constant "Tr" (ID32774):

0,01 s

Reglereinstellungen controller settings:

Stromregler current controller:

Verstärkung q-Achse/gain q-axis "Kpq" (ID34151):

0,64 V/A

Verstärkung d-Achse/gain d-axis "Kpd" (ID34152):

0,58 V/A

Nachstellzeitkonstante/time constant "Tnq" (ID34050):

1,2 ms

Nachstellzeitkonstante/time constant "Tnd" (ID34052):

1,2 ms

Adaption Verstärkung/adaption gain "Kpq2" (ID 34179)

20 %

Adaption Nachstellzeit/adaption time constant "Tnq2" (ID 34180)

400 %

Untere Anpaßschwelle/lower adaption limit "lua" (ID34177):

19 %

Obere Anpaßschwelle/upper adaption limit "loa" (ID34178):

68 %

Drehzahlregler speed controller (default for plain motor):

Verstärkung/gain "Kp_n" (ID100):

40

Nachstellzeitkonstante/time constant "Tn_n" (ID101):

20 ms

Spannungsregler voltage controller:

Spannungsregler/voltage controller "Kp" (ID34148):

0,08 A/V

Spannungsregler/voltage controller "Tn" (ID34149):

6 ms

Spannungsüberhöhung "dU" (ID34235):

116 %

Systemwiderstand "Rs" (ID34233):

0 Ohm

Motor-Datenblatt motor data sheet

AMK

Bezeichnung/name **DD5-14-10-POW** - 18600-B5
Teile-Nr/part numbe **A2370DD**

- Formula Student

Datum/date: 27.11.2018

Zeichn.-Nr./drawing no.: 12703-01260

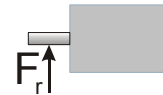
Mechanische Daten mechanical data:

Gesamtmasse/motor mass "m":	3,55 kg
Motorträgheitsmoment/inertia "J":	2,74 kgcm ²
Mech. zul. Drehzahl/mech. speed limit "Nmax":	20000 rpm
Rundlauf/run out (DIN 42955):	N
Wuchtgüte/balancing quality:	G2,5
Passfeder/shaft key:	-

Lagerbelastung bearing load:

(Lastangriff Mitte Abtriebswelle):

(Force to the middle of the shaft):

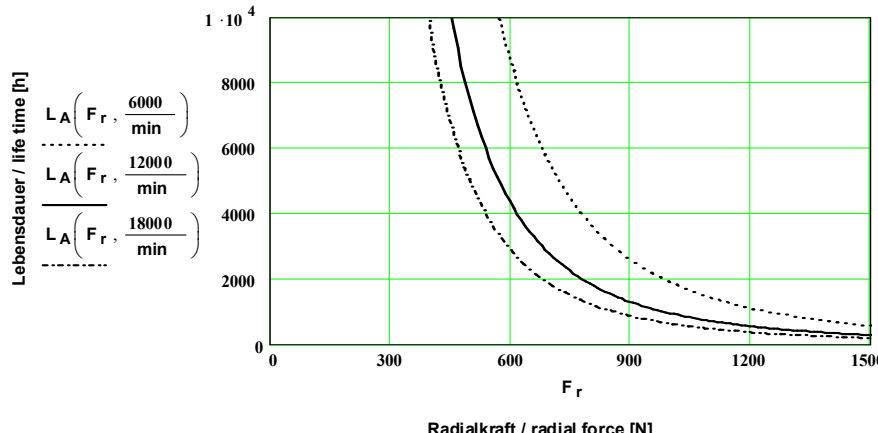


A/B - Lager/A/B - side bearing:

Lagertyp/bearing type :	6005 / 6003
Fettsorte/type of grease:	GE2 / GE2
theo. Fettgebrauchsdauer/grease life time:	13000 / 18000
bei Nenndrehzahl und 70°C Lageraußenringtemp/at rated speed and 158°F at outer bearing ring erforderliche Fettmenge/necessary grease quantity :	0 /
Maximale Axialkraft bei Montage/max. axial force for assembly:	3275 N



A - Lager/A - side bearing:



Bremsendaten brake data:

Typ/type:	-
Bremsmoment/brake torque:	Nm
Bremsstrom/brake current:	A
Bremsenspannung/brake voltage:	V
Spannungsart/voltage type	-
Einfallzeit/engage time "Te":	ms
max. Bremsenergie/max. braking energy:	-
einmalig/single engagement:	J
Lebenslang/lifetime:	J

Lüfterdaten fan data:

AMK-TNr./AMK part number:	-
Lüfterspannung/fan voltage:	V
Strom/current:	A
Frequenz/frequency:	Hz

Wicklungsschutz thermistor:

Typ/type (ID34166):	KTY84
Ansprechtemp./operation temp:	- °C
Widerstand/resistance (25°C) <=:	629 Ω

Geberdaten position encoder data:

AMK-TNr./AMK part number.	108072
Typ/type:	P
Impulszahl/number of pulses:	262144

Bemerkungen remarks:

automatisch erstellt, Geber 18 Bit,
Sonderparameter FSE
Daten nur gültig mit entsprechender Wasserkühlung

* Typenschildbezeichnung unterstrichen; bitte bei Rückfragen immer angeben / Nameplate data underlined; please state with every inquiry

Ersteller/created by: SMM

Änderungsstand Mechanik/revision motor-mechanics: 0.00 Änderungsdatum/motor revision motor date 26.10.2016

Für dieses Dokument und die darin enthaltenen Angaben behalten wir uns alle Rechte und technische Änderungen vor

All rights reserved for this document and all information included. Technical modifications reserved

(c) AMK Antriebs- und Steuerungstechnik GmbH Co. KG

4 Technical data

4.1 Technical data – inverter

	Terminal / strand	KW26-S5-FSE-4Q (2WD inverter) (data per inverter)
Rated input voltage HV+, HV- power supply	HV+, HV-	540 VDC
Input voltage range		250 VDC - 720 VDC
Input current		48 A
Power supply for HV = 540 VDC		75 µF
Intermediate circuit capacity		
Supply voltage for logic supply LV	X08 (X09)	24 VDC ±15%, The 0 V potential must be connected to the vehicle ground (vehicle chassis).
Input current for logic supply LV		≤ 500 mA
Capacity at input of internal switched-mode power supply		1,500 µF
Efficiency		Approx. 98%
Ground		Vehicle ground (vehicle chassis) or ground strap Switching GND for logic voltage is internally connected to the frame of the inverter
Control method Switching frequency		PWM 8 kHz
Output frequency ¹⁾	U, V, W	0 - 1200 Hz
Output voltage (HV = 540 VDC)		350 VAC (sinusoidal output current)
Output voltage range (HV = 250 - 720 VDC)		160 - 490 VAC
Rated output power		26 KVA
Rated output current I _N		43 A
Peak output current I _{max}		107 A
Max. duration of peak output current I _{max} • Output frequency f _{OUT} > 1 Hz		10 s
Max. duration of peak output current I _{max} • Output frequency f _{OUT} ≤ 1 Hz		1 s
Temperature sensor evaluation	X12	KTY e.g., KTY84-130
Protective / monitoring function		Short-circuit / ground fault, intermediate circuit overvoltage, excess temperature at motor / heat sink, current overload as per I _t t
Galvanic isolation voltage between HV and LV		2200 VDC
Cooling		Liquid cooling
Flow rate		1.5 bar / 10 l/min
Max. cold plate and ambient temperature		40 °C
Protection class		IP 00

	Terminal / strand	KW26-S5-FSE-4Q (2WD inverter) (data per inverter)
Dimensions (2WD inverter)		Approx. 339 mm length, approx. 183 mm width, approx. 131 mm height
Weight for 2WD inverter including heat sink		Approx. 6.3 kg

1) Speed setpoint values are limited to 30000 rpm

4.2 Technical data – motor

Please refer to the motor data sheet (see: Motor_data_sheet_A2370DD_DD5) for the technical data for the motor.



When the system is started up for the first time, the motor parameters are automatically transferred from the encoder database to the inverter.

The function is not performed if the motor parameters have already been entered manually. The AIPEX EVO's 'Initial program loading' (PW: 500591) function in direct mode allows the factory settings from AMK to be restored.

Prerequisite for the automatic transfer of the data from the encoder database:

- Encoder cable connected
- Motor parameters have not already been changed manually
- The data has been stored in the encoder at the factory

Appendix C

Current Reference using characterized inductances

As explained in Section 3.2.2, the used current references on the experimental results were not calculated using the inductance values obtained from the motor characterization. This section presents the current references calculated using the characterized curves.

An important distinction to make is that the curves in Figure C.1 present an inversion in torque signal depending on the direct axis current. This is due to the reluctance torque reaching and surpassing the torque generated by the permanent magnets. This phenomenon is due to the saturation effect, which reduces the quadrature axis inductance, while the direct axis inductance increases.

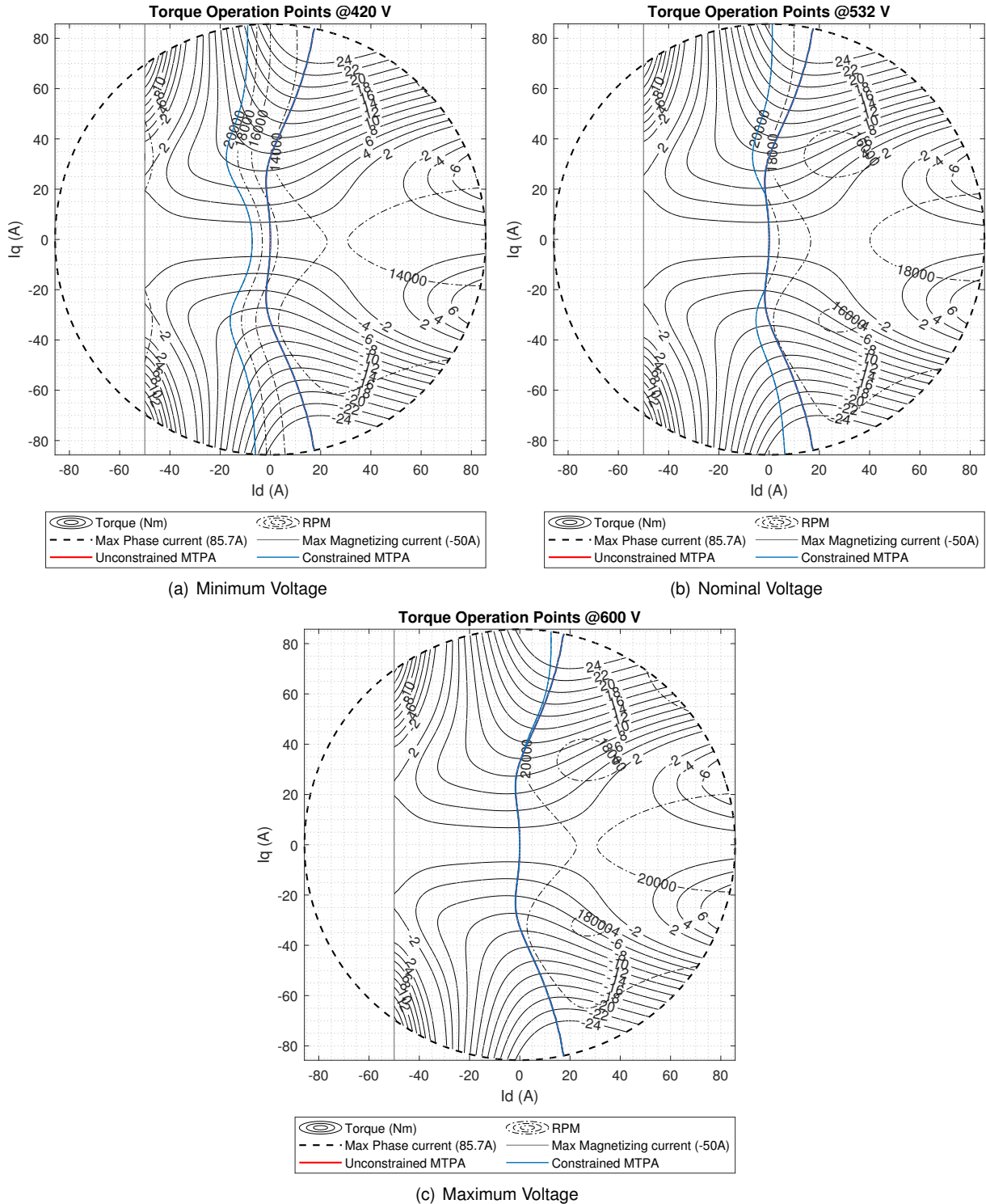


Figure C.1: Constrained Maximum Torque per Ampere curve at minimum, nominal, and maximum voltages. Reference currents are shown for 0, 13000 and 2000 RPMs.

Appendix D

Inverter Design

The new inverter design was intended to solve the current and voltage measurement issues that were present in the previous design, while also increasing the maximum current supported by the inverter. It was mainly designed using the same process as [5]. The design process started with the selection of the semiconductor devices based on an efficiency analysis, followed by the design of the gate drivers and the current and voltage measurement circuits. As this version of the inverter was intended to be used in the next prototypes, a special focus was given to reducing further the size of the inverter, while also making it more modular to allow for easier maintenance and replacement of components.

D.1 Efficiency Equation Formulation

To ease the process of choosing the semiconductor efficiency analysis approach was used. This was performed with the efficiency formulation for a three-phase inverter from [43], as it represents well the system developed. In [43] the power loss is assumed to be majorly composed by the semiconductor losses, as the inverter does not have magnetic components. This assumption is based on [44], where it is stated that the power losses of SiC MOSFET chips in the power module account for more than 93.4% of the total power losses of the power inverter.

The power losses of the MOSFET chips can be divided into conduction losses and switching losses defined as in [43]. The conduction losses are given by Equation (D.1).

$$\frac{P_{ON}}{P_o} = \frac{R_{DS_{on}}}{R_0} (1 + THD^2) \quad (\text{D.1})$$

Where P_{ON} is the conduction losses, P_o is the output power, $R_{DS_{on}}$ is the on-state resistance of the MOSFET, R_0 is the load equivalent resistance and THD is the total harmonic distortion of the output current.

The switching losses are presented in Equation (D.2).

$$\frac{P_{SW}}{P_o} = \left(\frac{\sqrt{3}}{2\pi m_p F_p} \frac{t_{on} + t_{off}}{T} + \frac{3C_t Z_0}{m_p^2 F_p T} \right) (3 - m_p) \quad (\text{D.2})$$

Where P_{SW} is the switching losses, Z_0 is the load equivalent impedance defined as $Z_0 = \frac{R_0}{F_p}$ with F_p being the load power factor, t_{on} and t_{off} are the turn-on and turn-off times of the MOSFET, T is the switching period, C_t is the total parasitic capacitance defined as $C_t = C_{oss} + C_d$ with C_{oss} being the MOSFET output parasitic capacitance, and C_d the external diode parasitic capacitance. The modulation index m_p used in this formulation is different from the one used on the control scheme, and it is defined as $\sqrt{6}V_{ORMS}/V_{DC}$ where V_{ORMS} is the line to neutral output RMS voltage.

The complete efficiency formulation is presented in Equation (D.3).

$$\eta = \frac{1}{1 + \frac{P_{ON}}{P_o} + \frac{P_{SW}}{P_o}} = \frac{1}{1 + \frac{R_{DSon}}{F_p Z_0} (1 + THD^2) + \left(\frac{\sqrt{3}}{2\pi m_p F_p} \frac{t_{on}+t_{off}}{T} + \frac{3C_t R_0}{m_p^2 F_p^2 T} \right) (3 - m_p)} \quad (D.3)$$

D.1.1 Motor and Controller parameters

With the efficiency equation defined, the next step was to define the load parameters, in this case, the motor operation points. As the power factor of the motor changes with the motor speed and torque, a map of the power factor was used. This map is derived from manufacturer data and is presented in Figure D.1(a). As the manufacturer only provided the power factor for positive torque, the power factor for negative torque was assumed to be the same as the power factor for positive torque. While this is not accurate, it is a good approximation for the efficiency analysis.

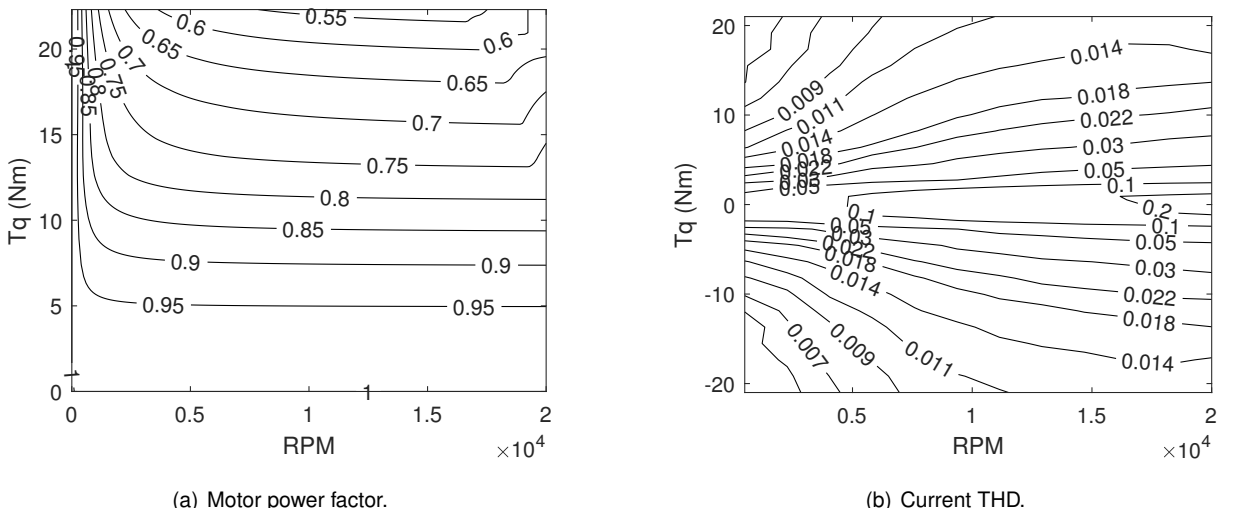


Figure D.1: Motor power factor and current THD maps as a function of the motor speed and torque.

The current THD was calculated using the simulation environment presented in Section 4.1. The motor was kept in a steady state for each of the operation points, and the current THD was calculated. The results are presented in Figure D.1(b).

D.2 Operation Points

As the load parameters are not constant a competition data-driven approach was taken to evaluate which module is better suited for the application. The logs from the 2023 competitions were used to create a 2-D histogram with the motor speed and torque usual operation points. Figure D.2 presents the histogram of the operation points for each motor in the 2023 Formula Student Germany (FSG) Endurance Event as an example.

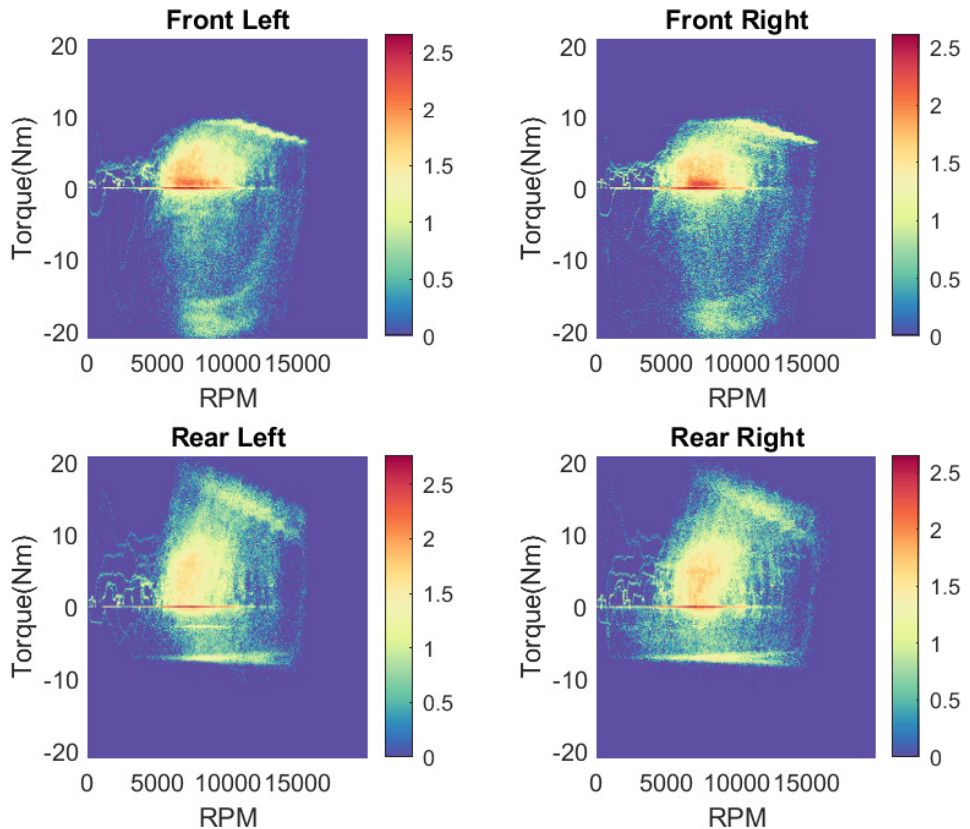


Figure D.2: Motor operation points for the 2023 Germany Endurance Event. The color represents the number of points in each bin on a logarithmic scale.

To generalize the design, each of the motor's operation points was combined, resulting in a single histogram with the operation points of all the motors. An example of the combined histogram is presented in Figure D.3.

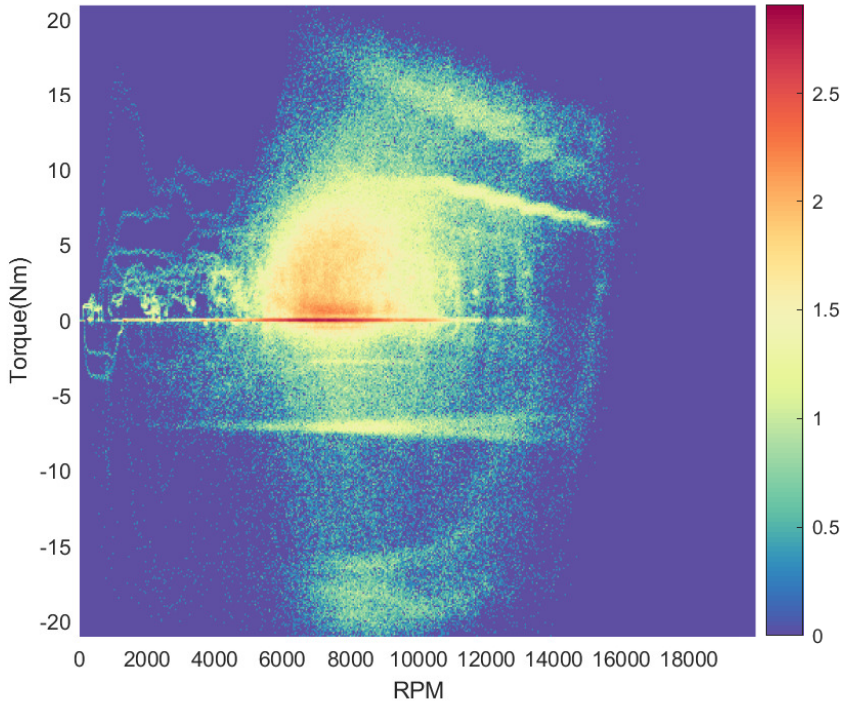


Figure D.3: Combined motor operation points for the 2023 Germany Endurance Event. The color represents the number of points in each bin on a logarithmic scale.

With the operation points defined, the efficiency of the inverter was averaged using the operation points histogram as weights. This allowed a direct comparison of the average efficiency of each semiconductor in a representative competition environment. The results for the chosen module are presented in ??.

D.3 Diode Selection

The antiparallel diode is used with two main functions, the first is to protect the MOSFETs from the reverse voltage generated by the motor inductance in case a fault occurs and the control shuts down the inverter while the motor is still spinning. Although in this case, the MOSFET body diode would allow the current to flow, it usually has a smaller forward current rating and a high forward voltage drop, thus in a failure mode it would heat the module and possibly damage it. The second reason is related to efficiency, as it allows the current that would flow through the MOSFET body diode to flow through the external diode, which has a smaller forward voltage drop, thus reducing the conduction losses in the dead time period. To select the proper diode to parallel with the MOSFETs, the principal factors are the diode must support at least double the DC Link voltage in reverse voltage, and the peak current of the diode must be at least the peak current of the motor. The continuous current rating is not a concern here because in normal operation as soon as the MOSFET is turned on the diode will not conduct any current, as the MOSFET resistance produces a voltage drop smaller than the forward voltage of the diode. Ideally, the diode would be dimensioned to endure the peak current for the longest fault mode, but

timing constraints prevented this study from being made, so it was dimensioned by the normal operation conditions of the motor datasheet [14]. The diode should also have a small parasitic capacitance to reduce the increase in the switching losses, and a low forward voltage drop to reduce the conduction losses in the dead time period.

Table D.1 presents the list of possible diodes for the new inverter design compared with the one used on the current design.

Table D.1: List of possible diodes for the new inverter design compared to the solution used on the current design.

Manufacturer	Model	V_{RRM}(V)	V_f(V)	I_f(A)	I_{fsm}(A)	C(pF)	T_{MAX}(° C)	Price (€)
ST	STBR3012-Y	1200	0.95	30	300	15	175	2.62
Littelfuse	LSIC2SD120D15	1200	1.5	44	120	76	175	10.5
Microchip	MSC050SDA120B	1200	1.5	109	290	214	175	16.6
GeneSiC	GD60MPS17H	1700	1.5	122	600	252	175	42.85
Vishay	VS-E5TH3012S2L-M3	1200	1.9	30	240	17	175	2.76
Cree	C4D10120E	1200	1.5	33	75	41.5	175	11.53

Due to its reduced cost and good performance, the ST STBR3012-Y was chosen for the new inverter design. While this is not a SiC diode, it still fulfills the requirements for the application and presents the best performance on paper.

D.4 MOSFET Module Selection

To increase the inverter density and improve the thermal performance the semiconductors were limited to half-bridge modules, as they allow for a more compact design and easy integration, while also reducing the number of components needed. The use of the half-bridge configuration was also motivated by the modularity provided, as this simplifies the design to one inverter leg that can be replicated to compose the complete inverter. This modularity also allows for easier maintenance and replacement of components, at the cost of the reduced number of available semiconductors in the market.

As the battery voltage currently used is 600V, the semiconductors needed to have a voltage rating of at least 1200V. The maximum motor current is approximately 150A, with a nominal current of $45A_{RMS}$, setting the minimum drain current rating of the MOSFETs to 45A. The other parameters can be reasonably selected to maximize the efficiency of the inverter. Based on these initial requirements a list of possible MOSFETs was created and shown in Table D.2. Note that the 1700V semiconductors are significantly more expensive than the 1200V semiconductors, thus they are not considered for the final design. The Microchip modules include Schottky diodes, while the other modules do not include the diodes, thus in the efficiency calculations the capacitance of the chosen diode was summed to the other modules to allow for a fair comparison.

For each semiconductor in the list, an efficiency map was created using the efficiency formulation presented in Equation (D.3), and the operation points histogram presented in Figure D.3 was used to

Table D.2: List of possible MOSFET modules for the new inverter design compared to the discrete solution used on the current design.

Manufacturer	Model	V _{DSS} (V)	R _{DSon} (mΩ)	I _d (A)	T _{max} °C	C _{oss} (pF)	t _{on} (ns)	t _{off} (ns)	Price (€)
Infineon	FF4MR12W2M1HP_B11	1200	4	200	175	840	44	16	260.85
Infineon	FF6MR12W2M1H_B11	1200	5.4	150	175	630	39	15	194.88
Infineon	FF08MR12W1MA1_B11A	1200	7.33	150	150	700	35	38	268.99
Infineon	FF8MR12W1M1H_B11	1200	8.1	100	175	420	70	20	165.21
Infineon	FF11MR12W2M1HP_B11	1200	10.8	100	150	315	41.1	21.2	125.12
Microchip	MSCSM170AM11CT3AG	1700	8.8	240	175	600	17	19	499.29
Microchip	MSCSM170AM15CT3AG	1700	11.7	181	175	450	17	19	425.52
Microchip	MSCSM120AM11CT3AG	1200	10.4	254	175	810	30	25	360.10
Microchip	MSCSM120AM16CT1AG	1200	16	173	175	540	30	25	206.89
Semikron	SK150MB120CR03TE2	1200	8	188	175	520	17	29	
Vincotech	10-EZ122PA016ME-LJ67F68T	1200	17	83	175	258	6.72	21.48	
Vincotech	10-EY122PA008ME01-LU38F06T	1200	9.11	184	175	516	40	16.92	
Wolfspeed	C2M0040120D	1200	44	55	150	171	61	13	45.94

Table D.3: Efficiency comparison of the possible MOSFETs modules for the new inverter design.

Manufacturer	Model	Conduction Loss (W)	Switching Loss (W)	Efficiency (%)	Price (€)
Microchip	MSCSM120AM16CT1AG	70.80	15.53	98.76	206.89
Vincotech	10-EZ122PA016ME-LJ67F68T	75.22	7.94	98.80	
Infineon	FF11MR12W2M1HP_B11	47.78	15.66	99.08	125.12
Microchip	MSCSM120AM11CT3AG	46.02	17.38	99.08	360.10
Microchip	MSCSM170AM15CT3AG	51.77	10.83	99.09	425.52
Infineon	FF8MR12W1M1H_B11	35.84	22.34	99.16	165.21
Vincotech	10-EY122PA008ME01-LU38F06T	40.31	15.88	99.19	
Infineon	FF08MR12W1MA1_B11A	32.43	20.60	99.23	268.99
Microchip	MSCSM170AM11CT3AG	38.94	11.85	99.26	499.29
Semikron	SK150MB120CR03TE2	35.40	13.56	99.29	
Infineon	FF6MR12W2M1H_B11	23.89	16.03	99.42	194.88
Infineon	FF4MR12W2M1HP_B11	17.70	18.76	99.47	260.85
Wolfspeed	C2M0040120D	194.69	17.19	97.00	45

compute the average efficiency throughout the last FSG Endurance event. The average results are presented in Table D.3.

Although it does not have the highest efficiency, the Infineon FF8MR12W1M1H_B11 [45] was chosen as it has one of the smallest footprints, while having good efficiency and a reasonable price. It also brings significant performance gains when compared to the discrete option used on the current inverter design that averaged at 97% efficiency, and even more when compared with the inverter currently used on the vehicle, which averages at only 86%. One interesting factor to note here is the dominance of the conduction losses over the switching losses, indicating an increase in switching frequency could be beneficial to the efficiency of the inverter as it would reduce the current THD and thus the conduction losses. The resulting inverter efficiency is presented in Figure D.4(d).

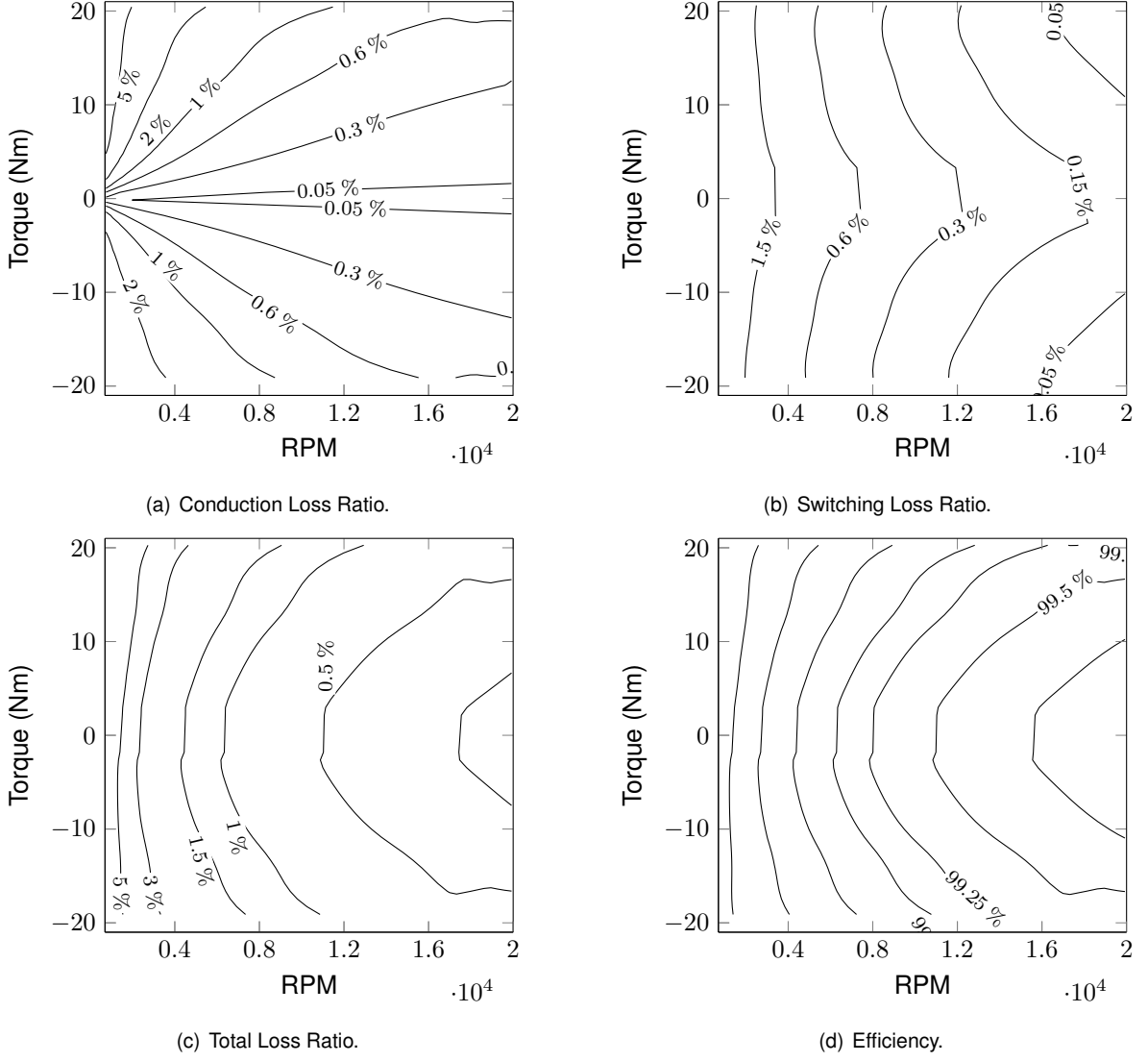


Figure D.4: Render of the PCBs used in the new inverter design.

D.5 Gate Driver Design

The selection of the gate driver was based on models proposed by the manufacturer, with the key aspects being a high source/sink current capability, galvanic isolation, and a fast desaturation function. The selected device was the Infineon EiceDRIVER™ 1ED332xMC12N [46], but as the design was defined to have the main gate driver on a mezzanine board, a secondary gate driver was needed to be placed next to the module on the power module and reduce the parasitic inductance of the gate driver connections. The secondary gate driver does not need such strict requirements, only requiring a high source/sink current capability, as the desaturation function and isolation are already present on the main gate driver. The selected secondary gate driver was the Texas Instruments UCC27614 [47], as it can provide 10A of source/sink current, can withstand the -5 to 18V voltage range of the primary gate driver, while having a small 8-Pin SON DSG footprint.

The gate resistance was chosen using the recommended values from the datasheet of the MOSFETs

module, set in 8.2Ω for charging and 2.7Ω for discharging the gate. One drawback of using this cascaded gate driver approach is the increased impedance seen by the primary gate driver, as the secondary gate driver has an input impedance of $120k\Omega$, which makes this signal extremely sensitive to noise. To mitigate this issue, a strong pull-down resistor was added near the secondary gate driver input to reduce the impedance seen by the primary gate driver. A $5.6k\Omega$ resistor was chosen, as this is the smallest resistance value that does not exceed the maximum power dissipation of a 0603 resistor. A low-pass filter was also added to the gate driver input after the pull-down, with a cutoff frequency of $4.8229MHz$ to increase noise immunity. Equation (D.4) was used to calculate the decoupling capacitor value that would allow a voltage ripple smaller than 1%. In this equation Q_g is the gate charge of the MOSFETs, V_s is the supply voltage swing of the gate driver, $C_{decoupling}$ is the decoupling capacitance, $V_{initial}$ is the initial voltage of the capacitor, and V_{final} is the final voltage of the capacitor. The resultant value was $5\mu F$, but a smaller $100nF$ was added in parallel to account for high-frequency oscillations.

$$E = Q_g V_s = \frac{1}{2} C_{decoupling} (V_{initial}^2 - V_{final}^2) \quad (\text{D.4})$$

The short circuit protection of the MOSFETs was made using the desaturation function of the primary module, the used circuit is shown on Figure D.5. The desaturation function is a protection mechanism that detects the voltage drop on the MOSFETs when they are on, and if this voltage drop is higher than a certain threshold, the gate driver turns off the MOSFETs. This is a very important protection mechanism, as it can prevent the MOSFETs from being destroyed in case of a short circuit.

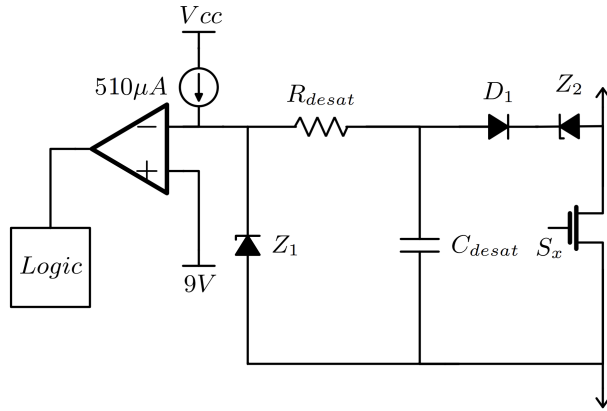


Figure D.5: Desaturation protection circuit (adapted from [5]).

The threshold voltage of the desaturation on the primary gate driver is $9V$, so the Zener diode Z_2 was used to produce a higher voltage drop and trigger the desaturation function with a lower current. The MOSFET datasheet details the V_{DS} with different drain currents and gate voltages, based on that it was verified that at room temperature the MOSFET has a V_{DS} of $1V$ with a $120A$ drain current. As the module heats up this voltage drop is reached with lower currents, thus it has a negative feedback that ensures the current will not exceed $120A$. As the diode D_1 has a forward voltage drop of $1V$ at room temperature, Z_2 should have a Zener voltage of $7V$, summing up to the $9V$ reference voltage of the gate driver. This is a very conservative current limit to start the design tests, but as the team's confidence in

the design is increased, the Zenner voltage can be decreased to allow higher currents.

The desaturation function has a blanking time to account for short bursts of current in normal operation, this blanking time is defined by the resistor R_{desat} and the capacitor C_{desat} . They were dimensioned by Equation (D.5) to have a blanking time of $3.8\mu s$.

$$t_{desat} = \frac{V_{ref}C_{desat}}{I_{desat}} \quad (D.5)$$

D.6 Current and Voltage Measurement

The design of the current and voltage sense was focused on increasing its noise immunity, as the previous design had issues with the current measurement. The current sensor was chosen to be the LEM LA 100-P [48], as it's a compact solution that can measure up to $150A$ with low drift and linearity error while having the bandwidth necessary for the fast controller frequency. Another advantage of this sensor is that it does not use integrated conductors, it only needs to wrap the primary conductor with the sensor, and as such, the current sense board does not need to be designed for high currents. This sensor outputs a current in the secondary circuit proportional to the primary circuit current, so a measurement resistance was set to 33Ω as recommended by the manufacturer.

The output voltage is amplified and converted to a differential signal by a low drift operational amplifier with passive and active low pass filters, both with a cutoff frequency of $72.3kHz$. This signal conditioning was placed as close as possible to the sensor output to reduce EMI in the readings. Next to the signal conditioning circuitry, a 14-bit SAR ADC was placed to read the sensor output. This multichannel ADC is also used to read the voltage and temperature sensors. Its output is sent to the main controller through an RS-485 communication interface.

The voltage sense is done using a voltage divider followed by an isolated amplifier that also is coupled with an active lowpass filter. The voltage divider has a configurable input that allows selecting the module to measure DC Link voltage or motor phase voltage. This ability to measure the motor voltage was implemented to enable future automatic characterization routines.

D.7 PCB Design

The PCB was designed with creepage distances according to IPC2221A [49] to withstand the maximum battery voltage. One of the main goals in the PCB design was to keep the solution compact, and to achieve that a mezzanine approach was selected. This approach allowed the leg module to be designed within the size of the MOSFET module, reducing the size of the inverter and allowing for great liberty with how the modules are arranged by the team inside the inverter container.

The design is comprised of three main boards: Half-Bridge, Driver, and Current sense boards. The Half-Bridge board is the only board carrying high currents in the inverter, it contains the MOSFETs, DC Link capacitors, and the secondary gate drivers. It uses a 8-layer stack-up with copper thicknesses of $70\mu m$ on external layers and $35\mu m$ on internal layers. The use of 8 layers allowed to increase the

current carrying capability of the board, being able to stand a current of 90A continuously. The Driver board contains the primary gate driver, the isolated DC/DCs to supply the gate drivers, and the isolation components for the voltage and temperature measurement. It also handles the connection with the other boards and the main controller. The Current sense board contains the current sensor coupled with the signal conditioning circuitry. It also includes the ADC to read all the module sensors and the communication interface with the main controller. The communication is done using RS-485, as it is a robust communication protocol that can be used in noisy environments. A render of each board and the final leg module is presented in Figures D.6 and D.7.

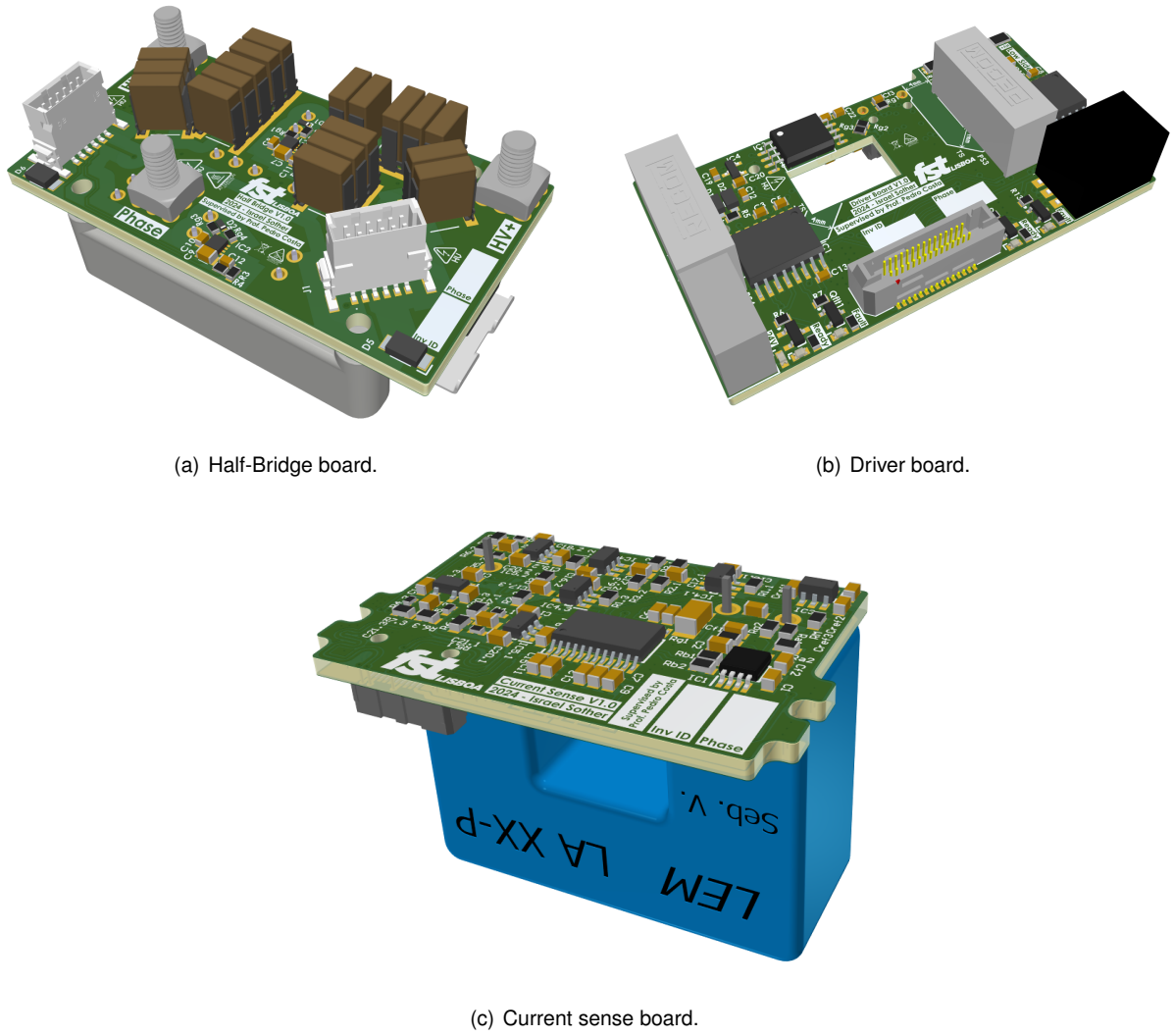


Figure D.6: Render of the PCBs used in the new inverter design.

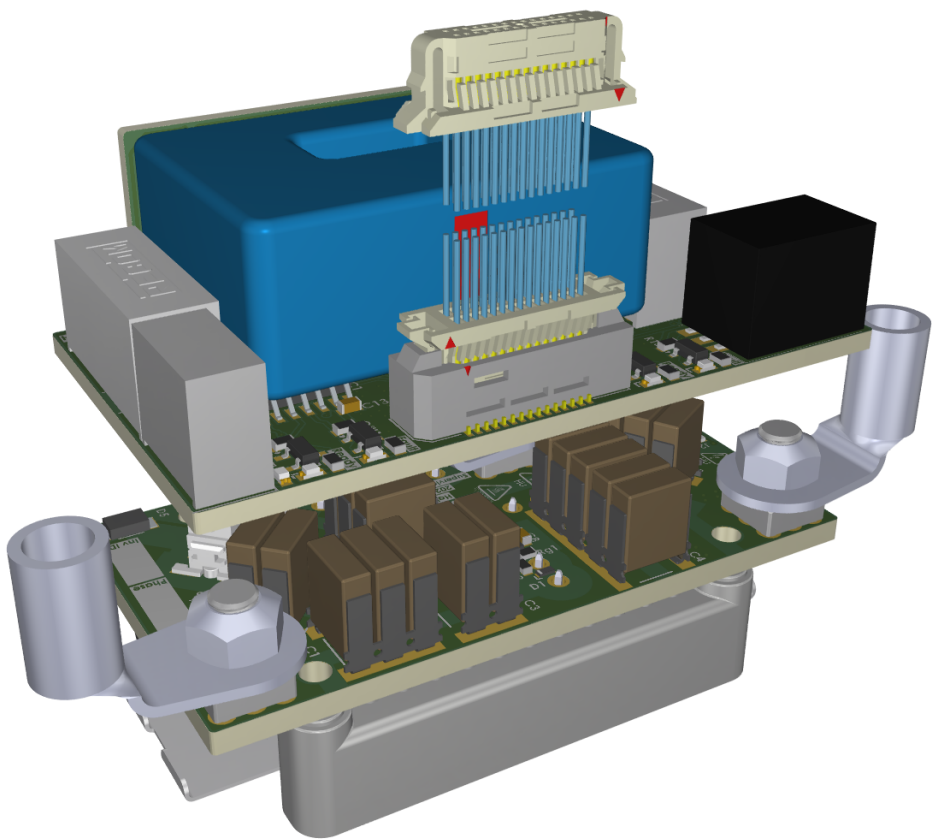
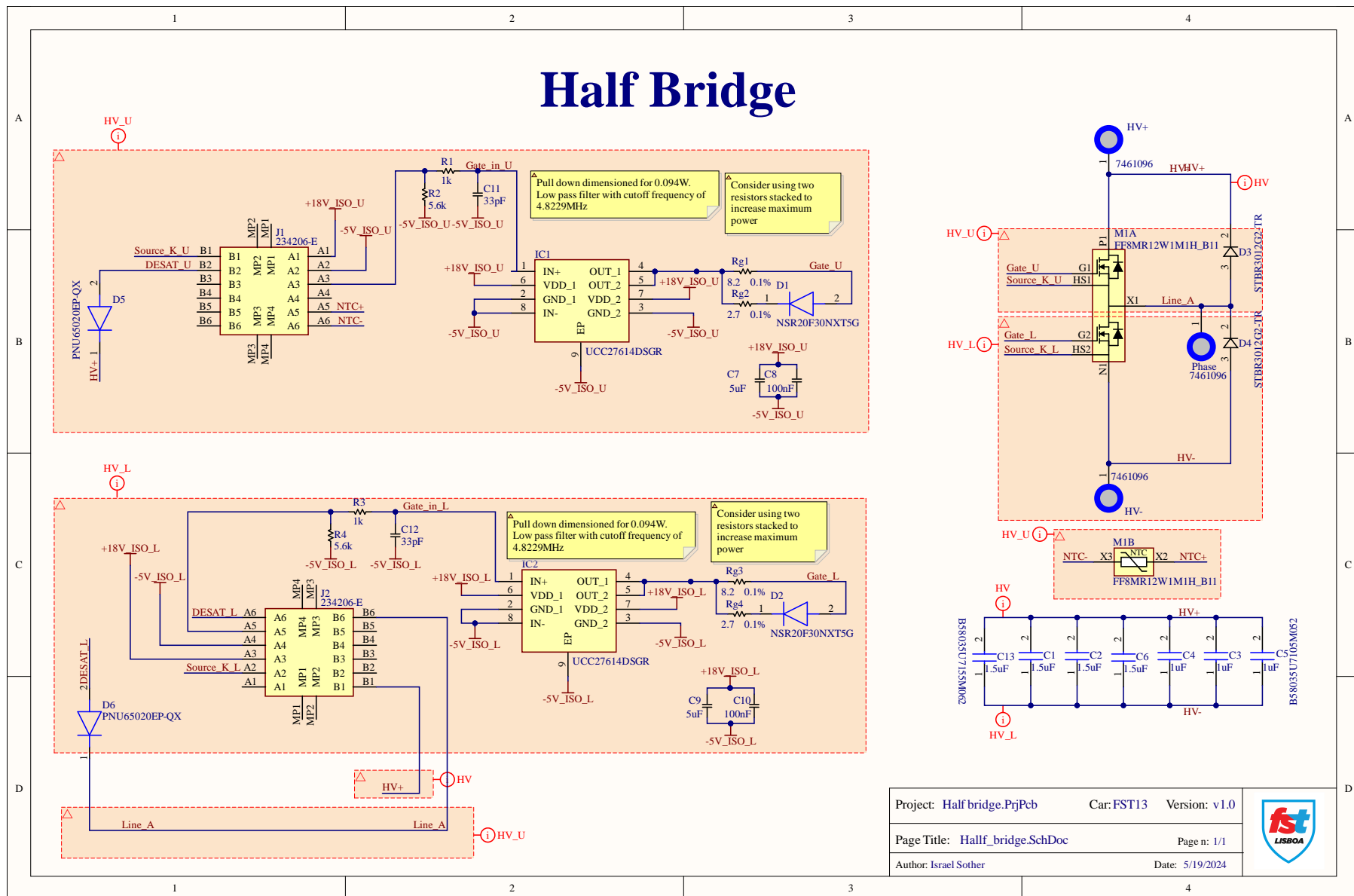


Figure D.7: Render of the final leg module.

D.8 Inverter Schematics and Layers

The resulting schematics and layers of the inverter are presented in the next pages.

D.8.1 Half Bridge Board Schematic



D.8.2 Half Bridge Board Layers

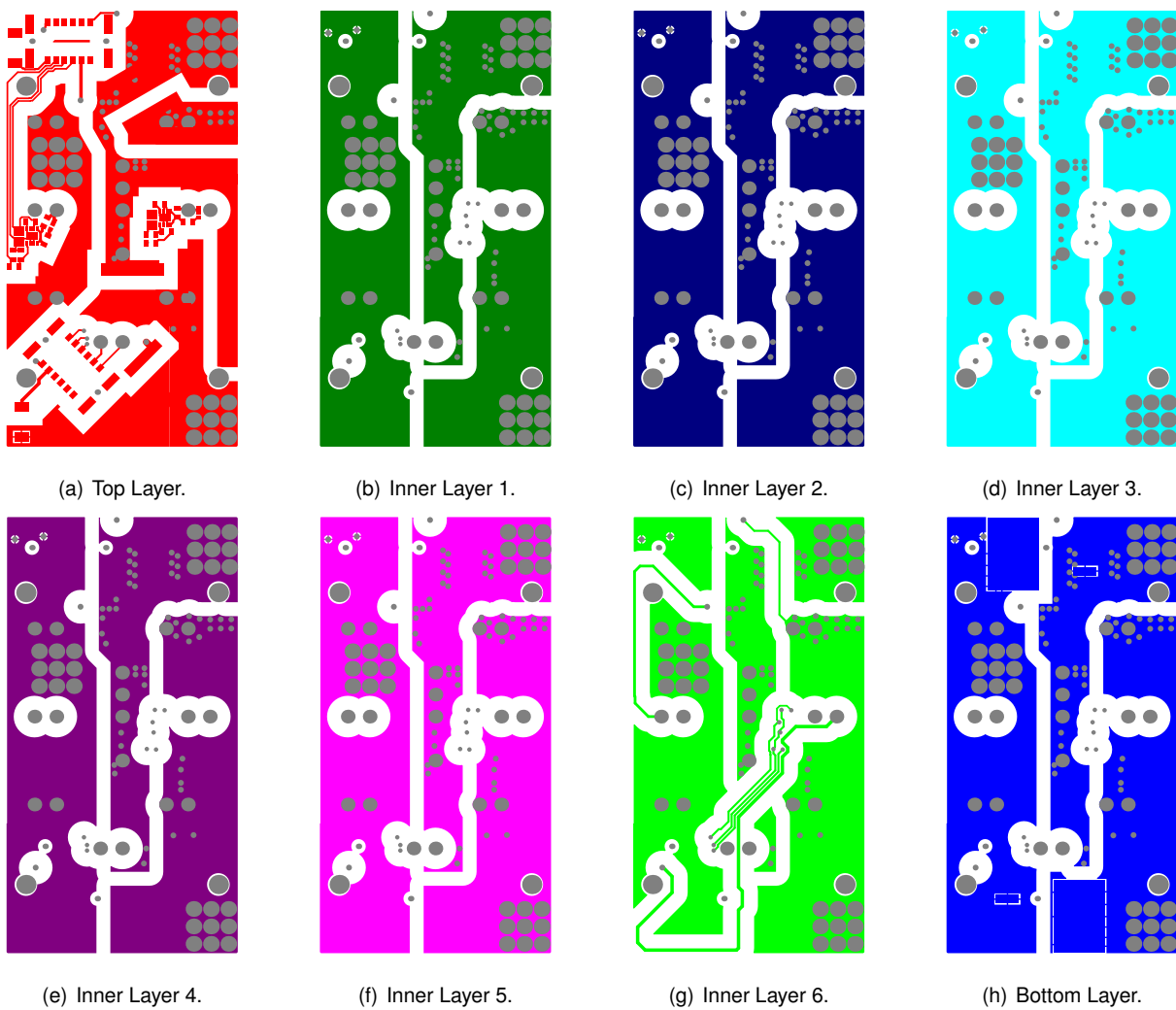
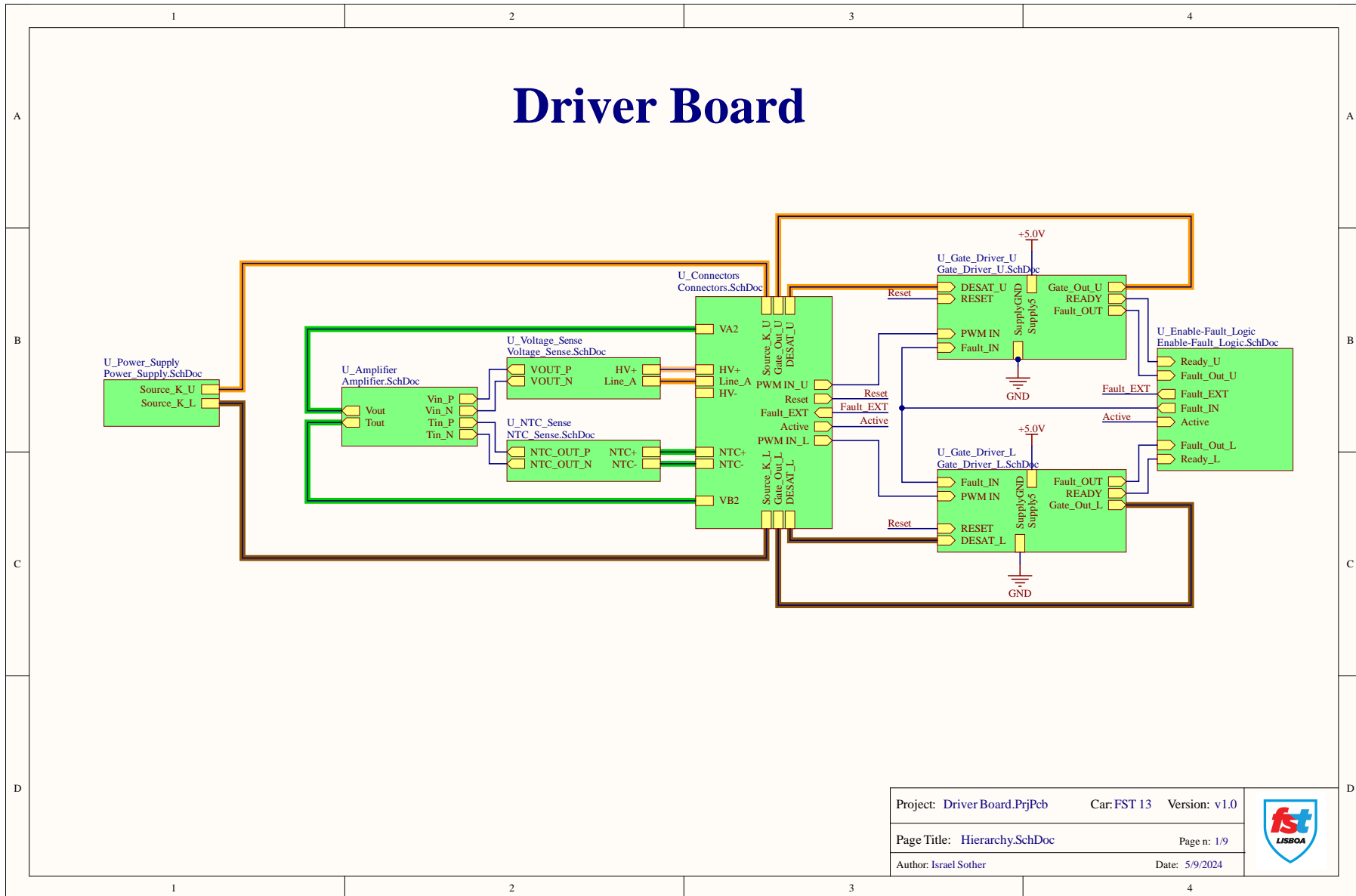


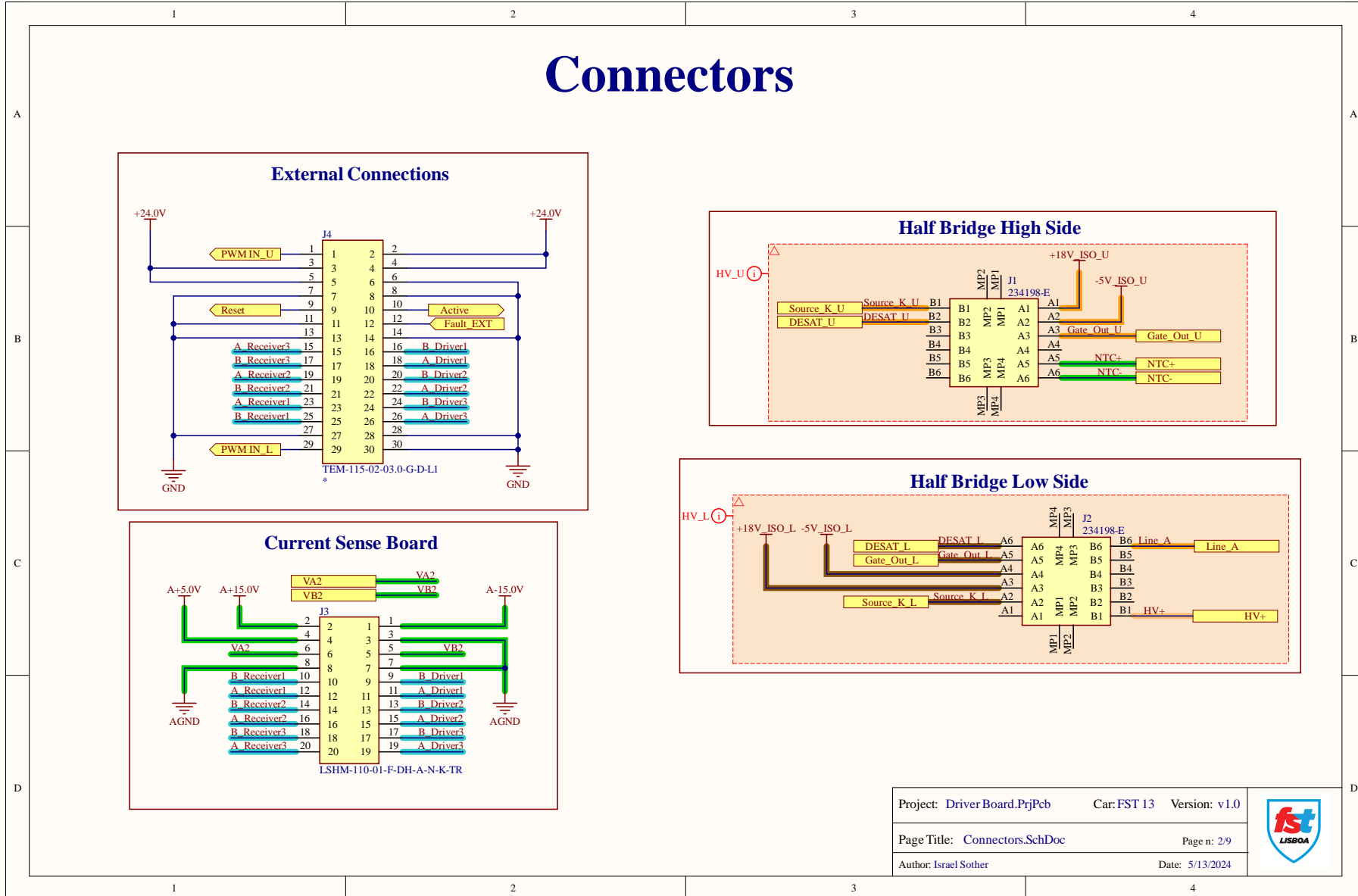
Figure D.8: Half Bridge Board Layers.

D.8.3 Gate Driver Board Schematic

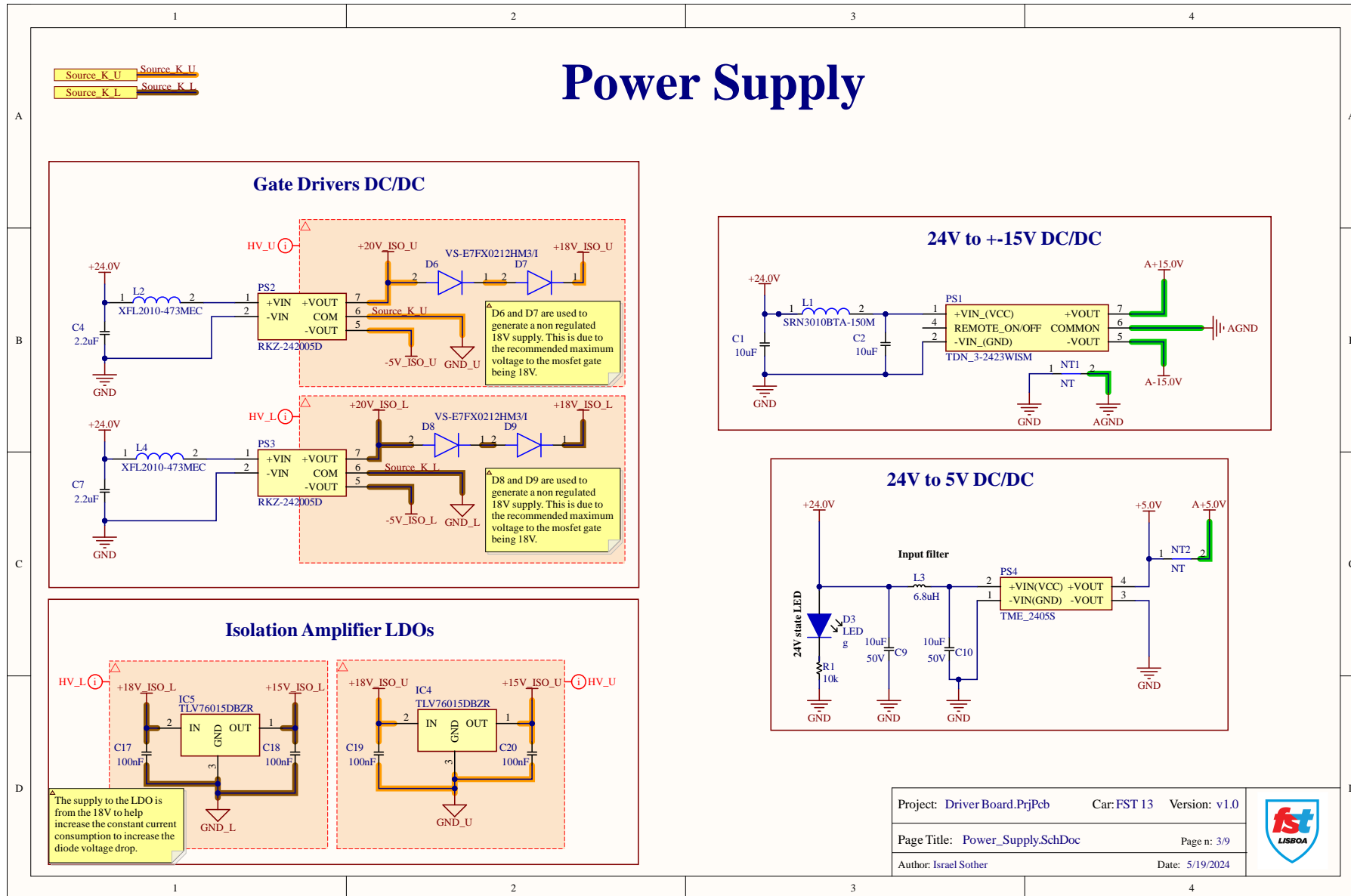


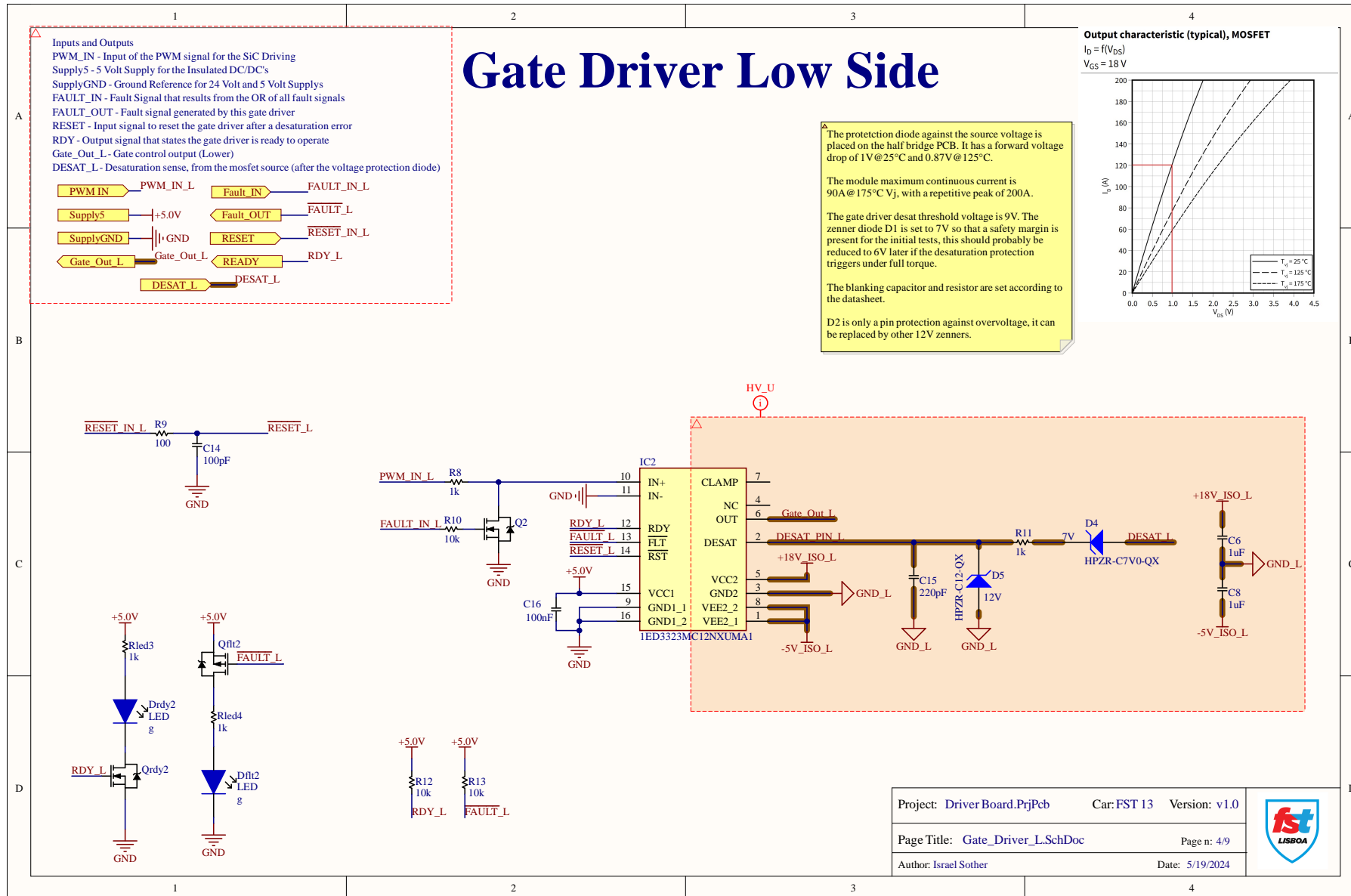
Connectors

8

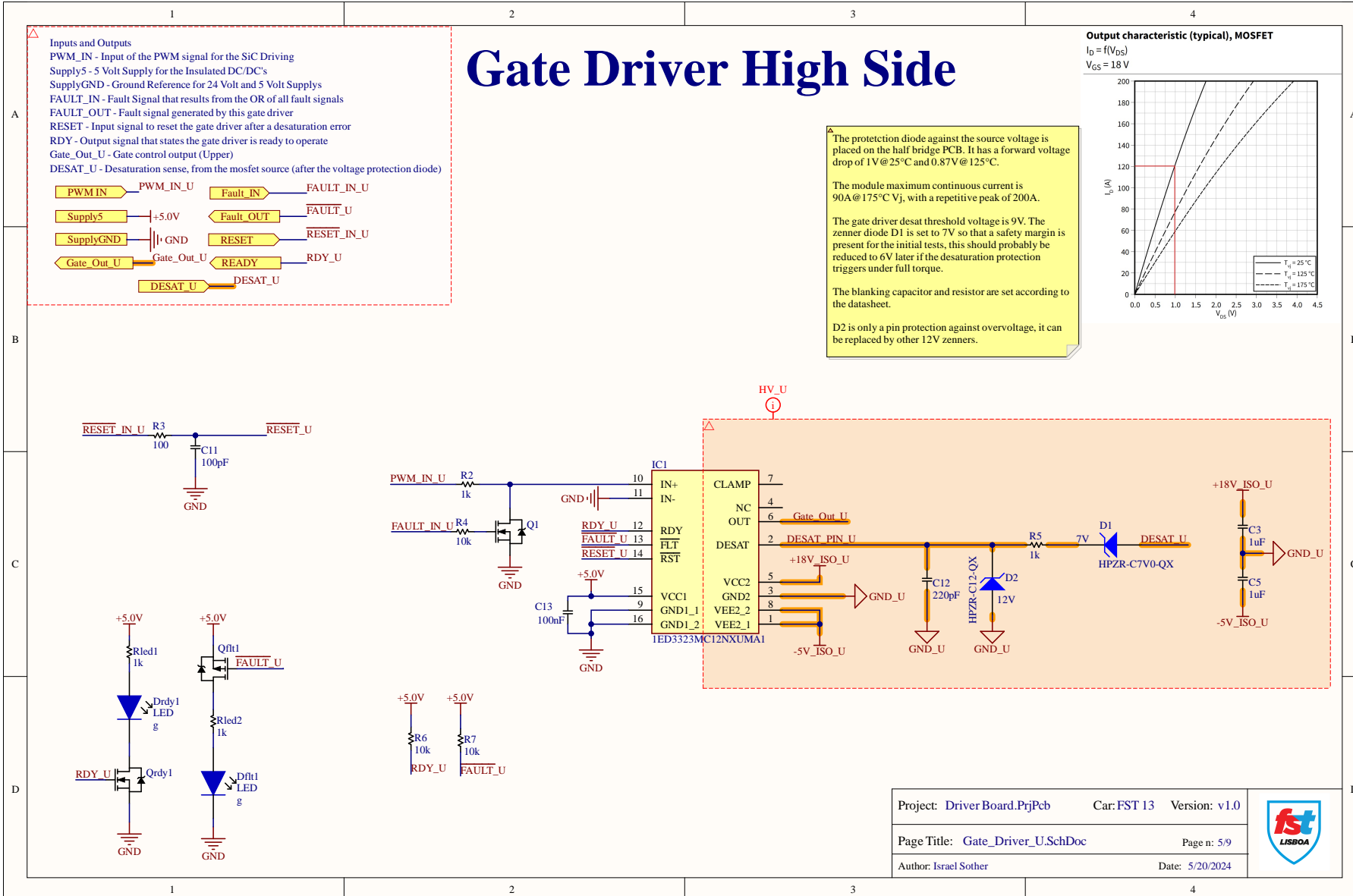


Power Supply

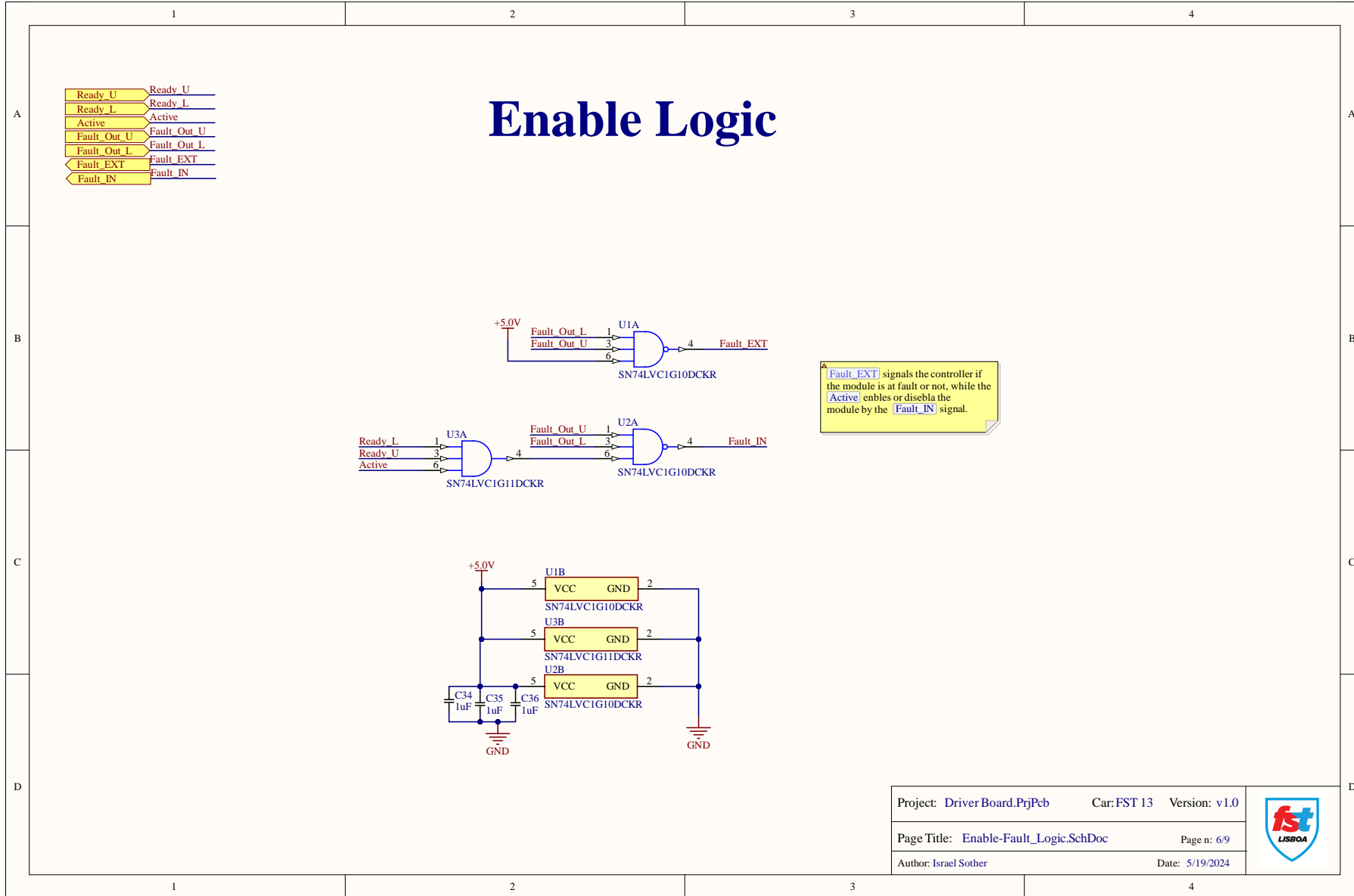




Gate Driver High Side

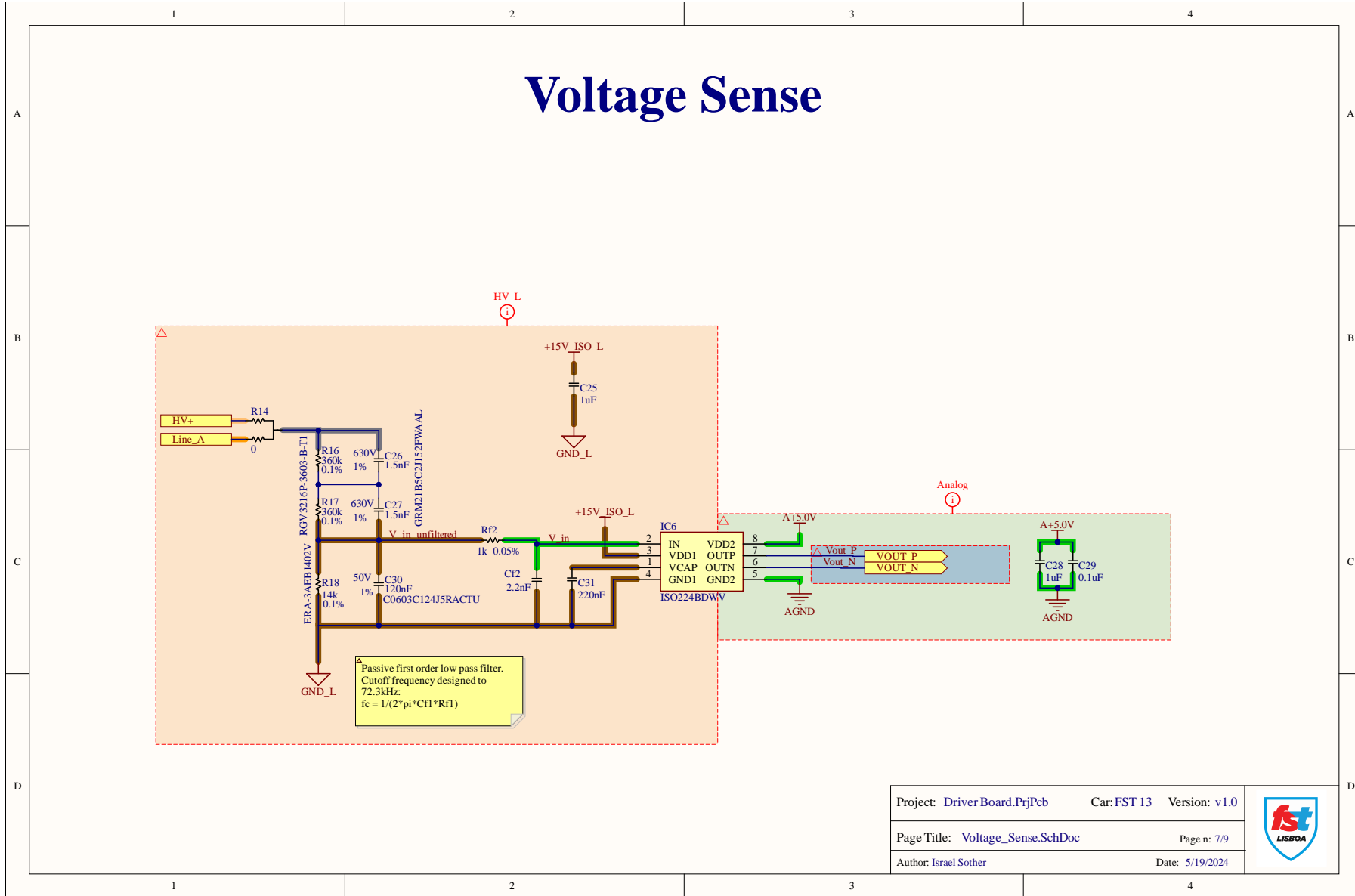


Enable Logic

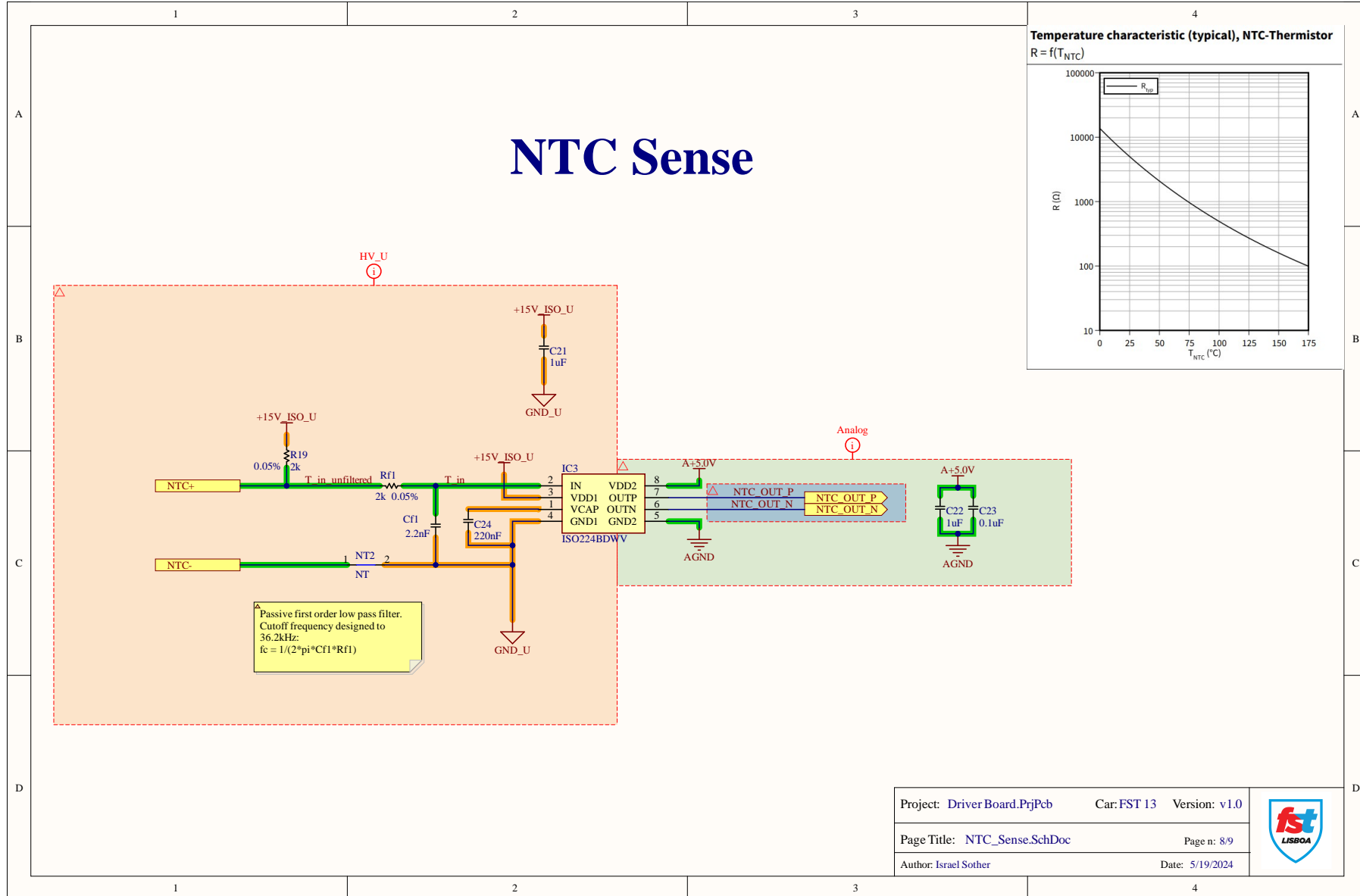


Voltage Sense

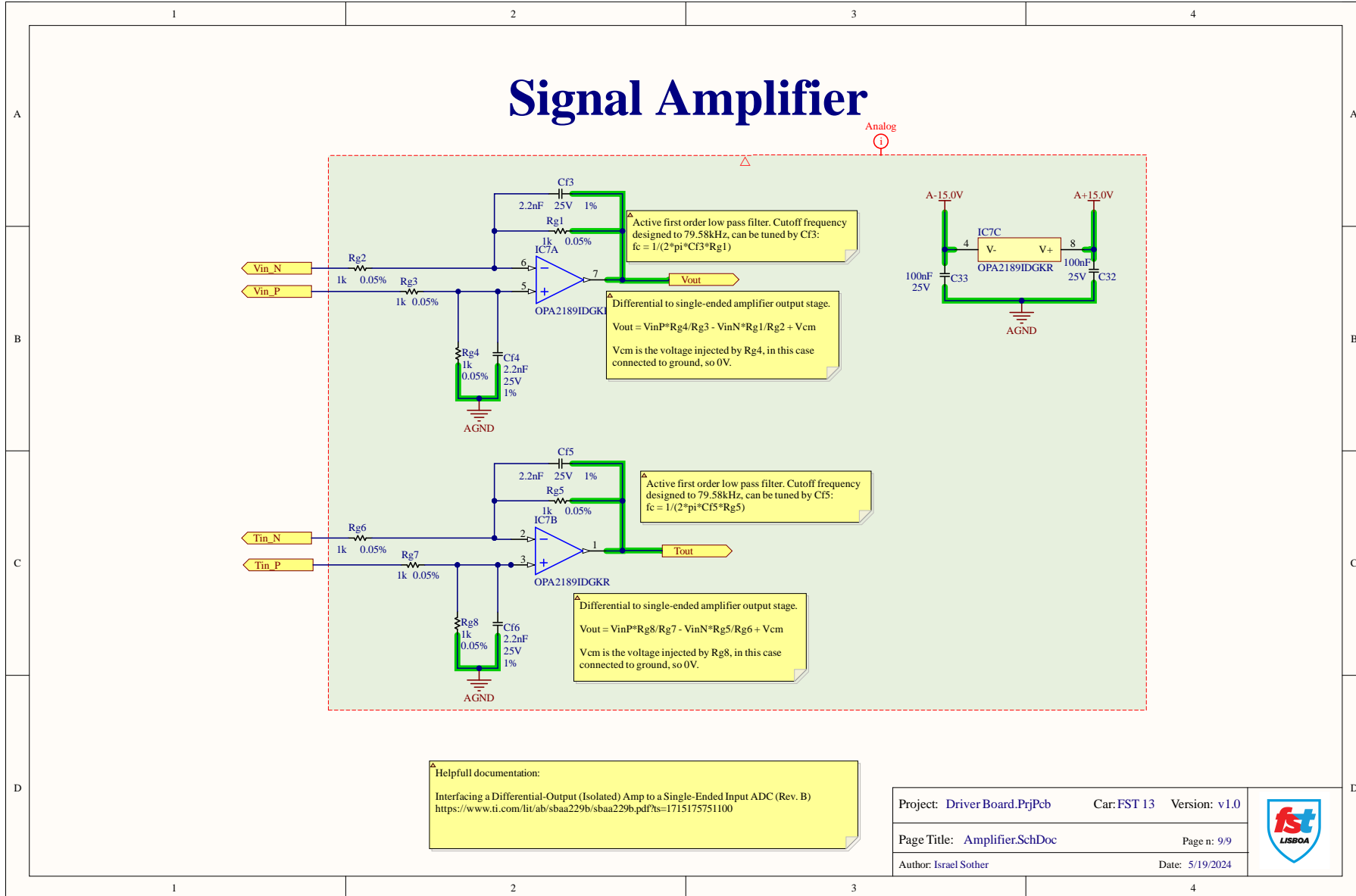
92



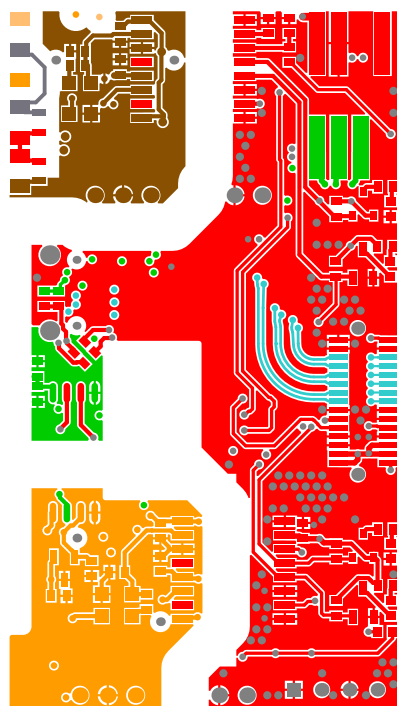
NTC Sense



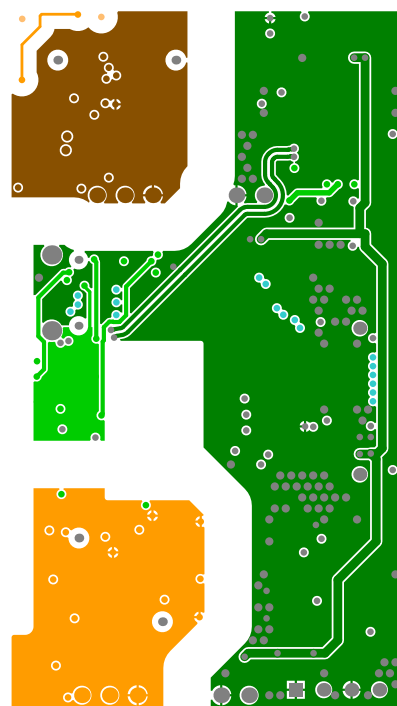
Signal Amplifier



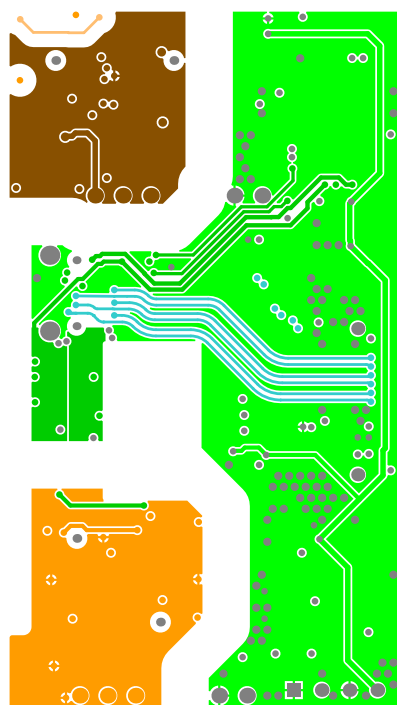
D.8.4 Gate Driver Board Layers



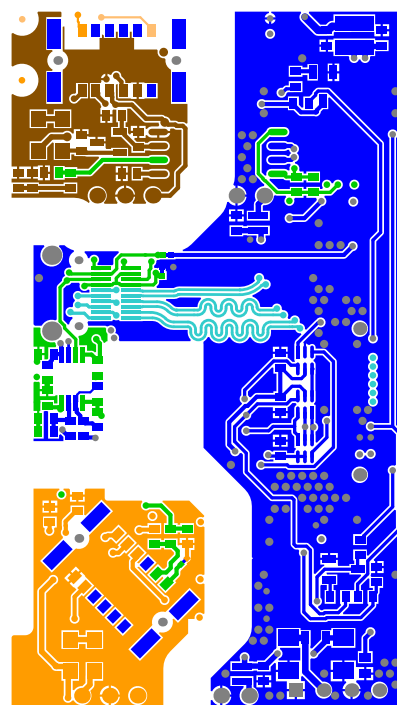
(a) Top Layer.



(b) Inner Layer 1.



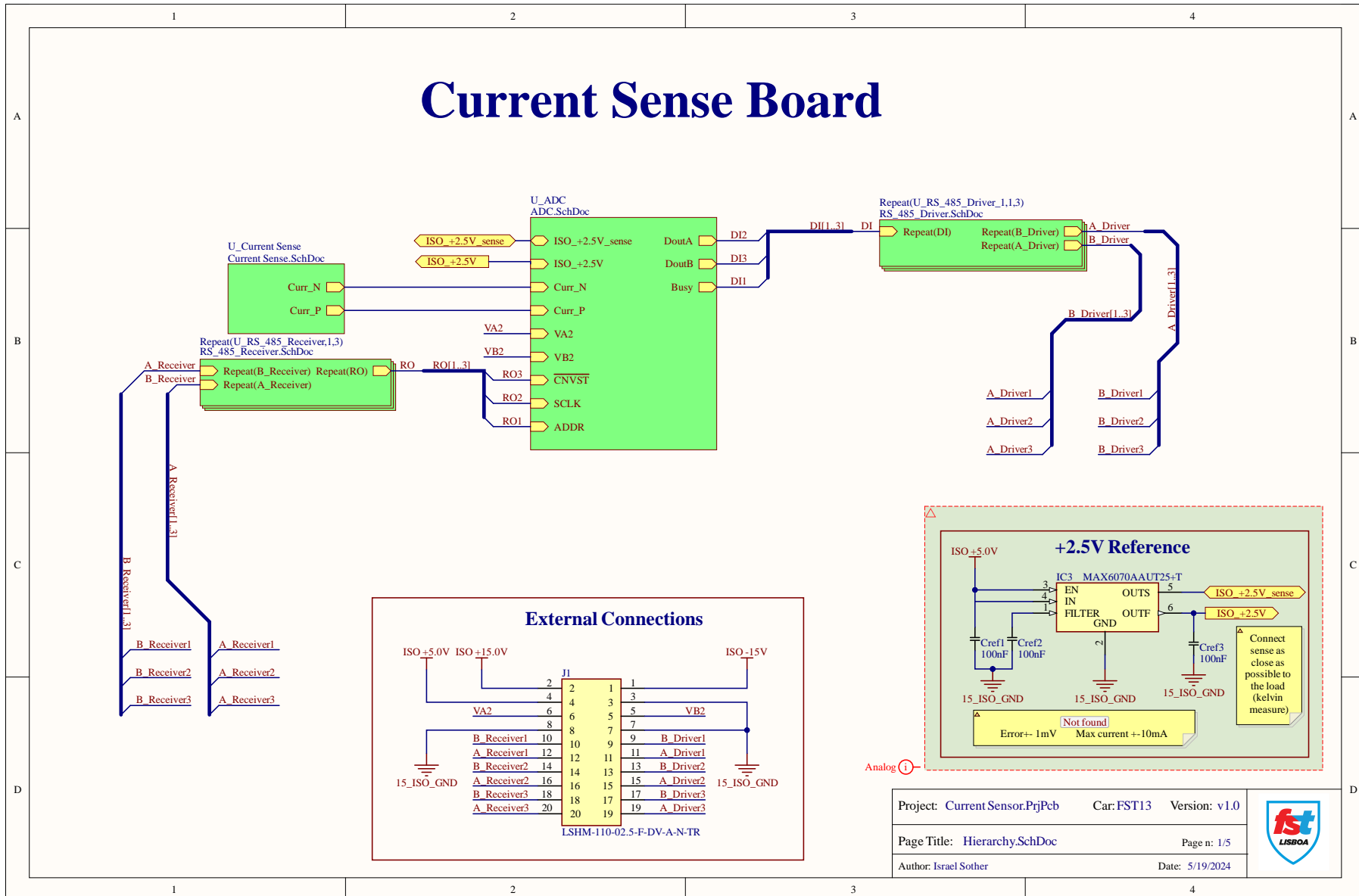
(c) Inner Layer 2.



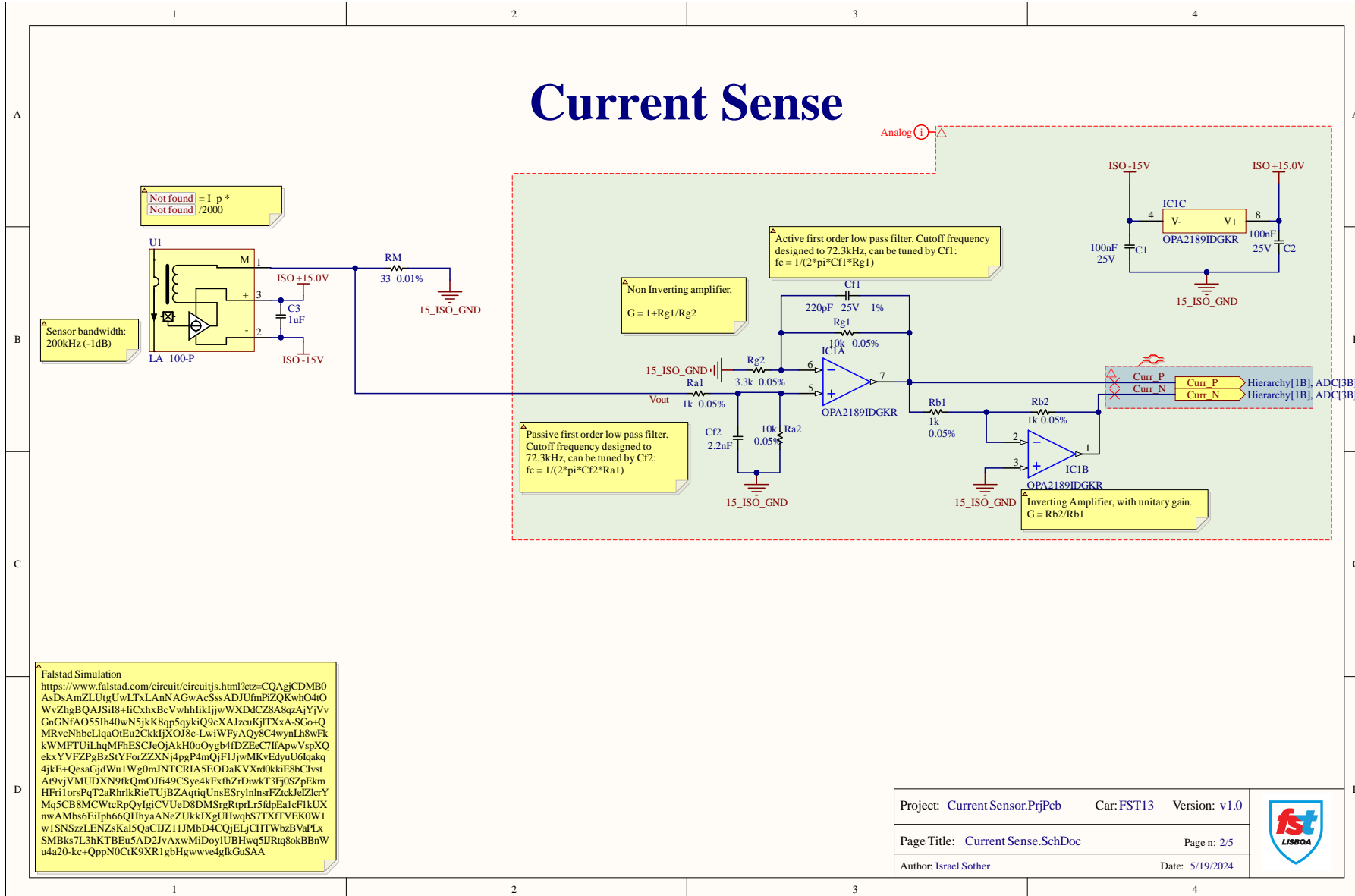
(d) Bottom Layer.

Figure D.9: Gate Driver Board Layers.

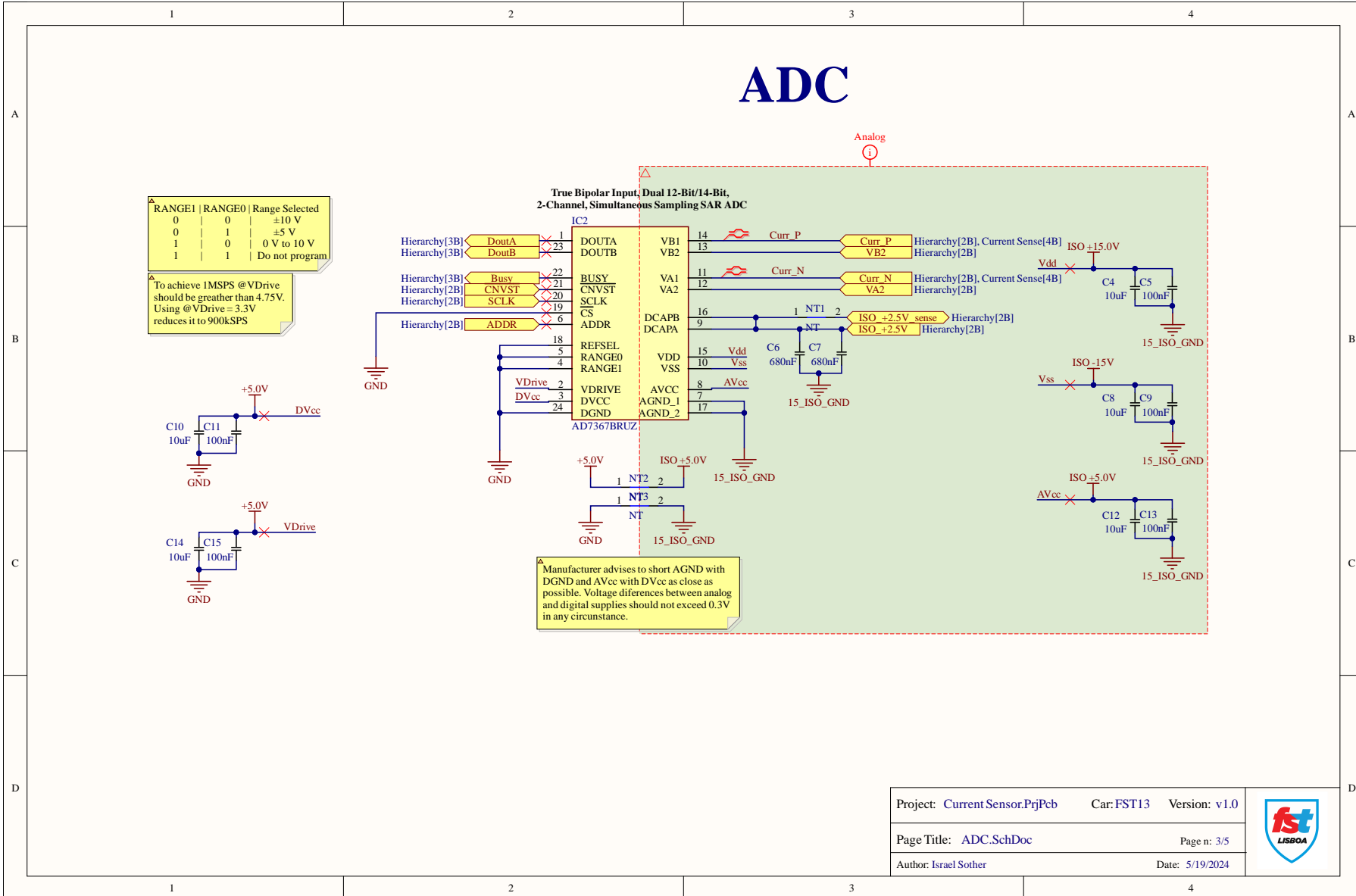
D.8.5 Current Sensor Board Schematic

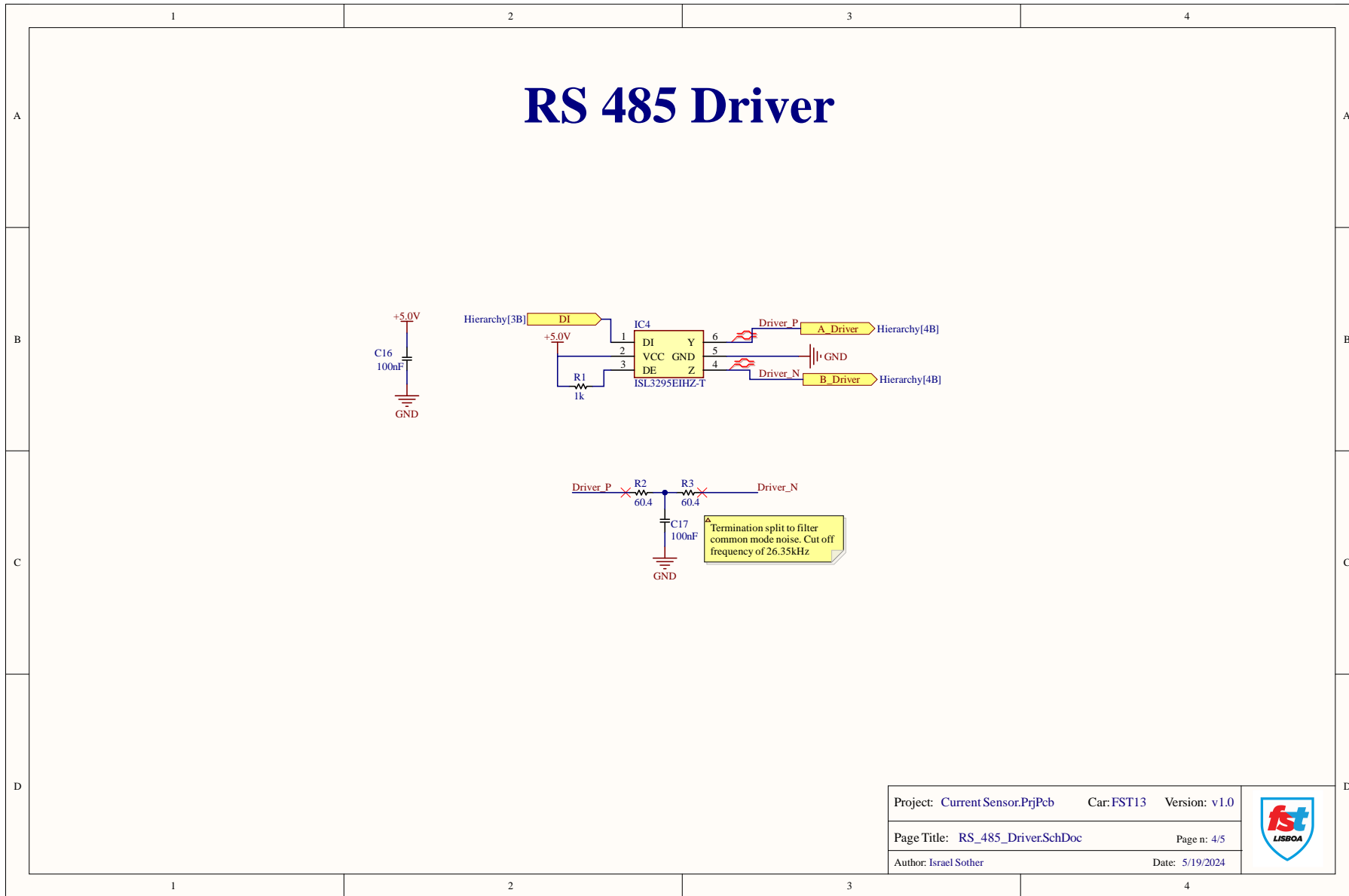


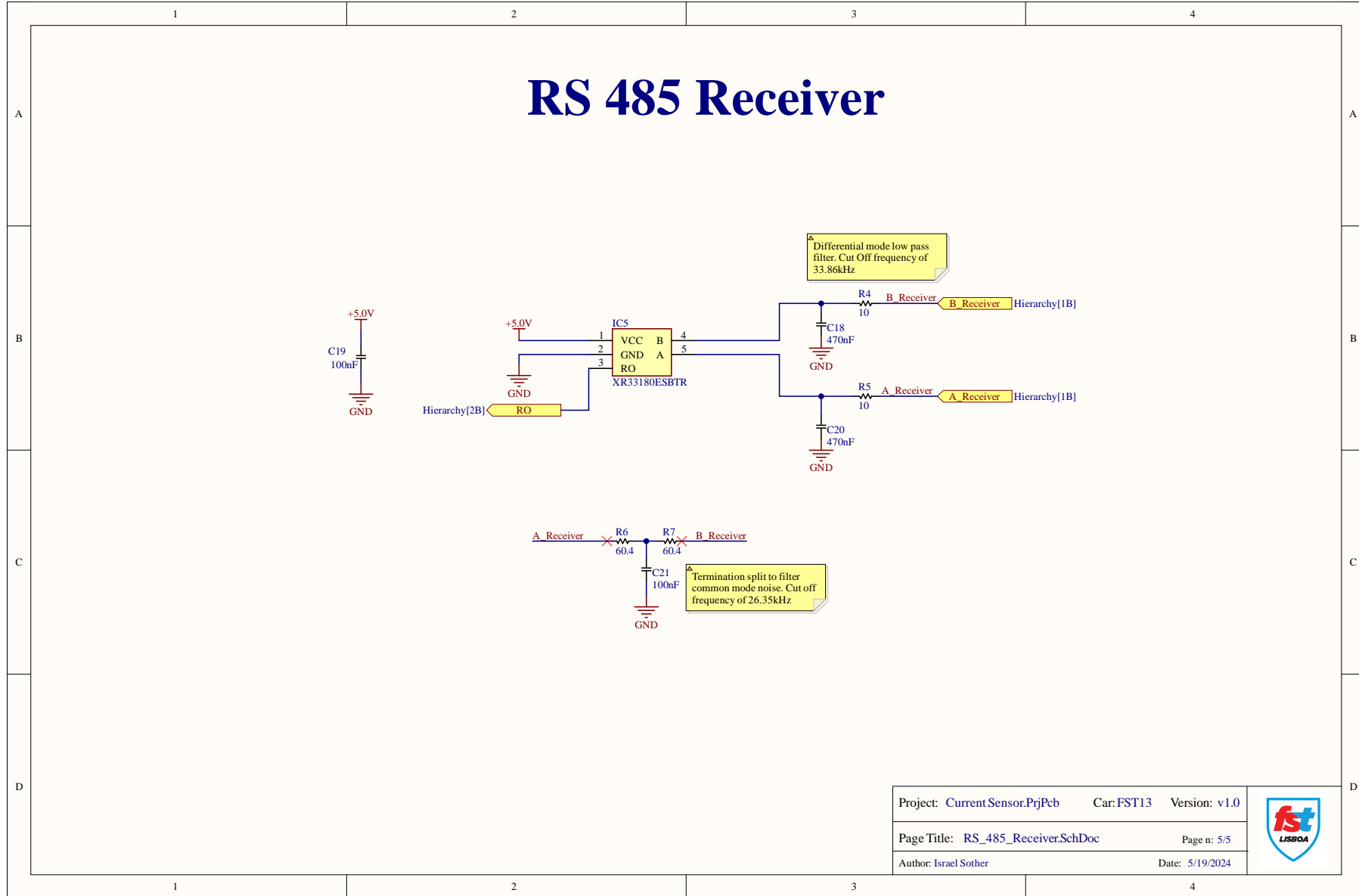
Current Sense



ADC





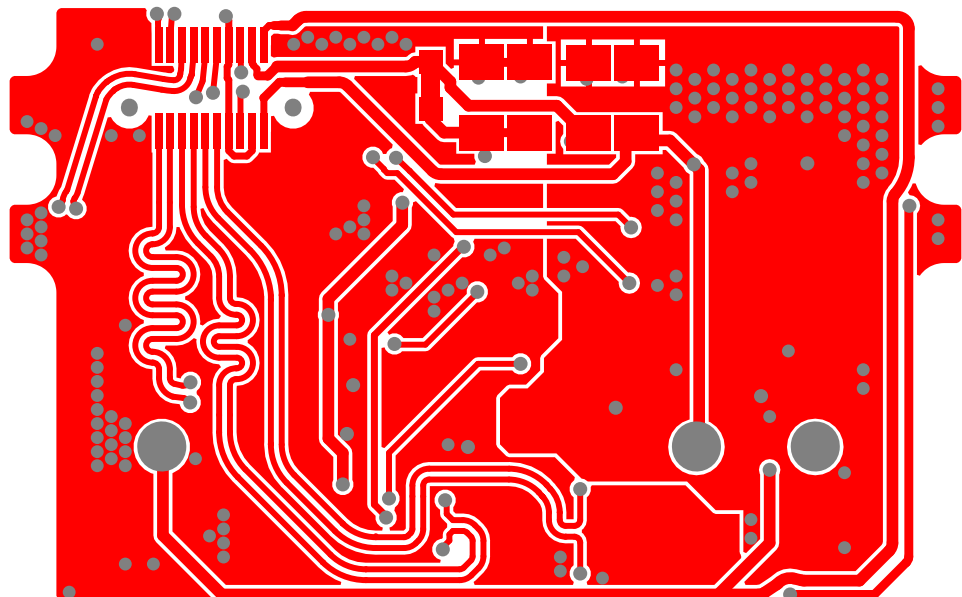


Project: Current Sensor.PrjPcb Car: FST13 Version: v1.0
 Page Title: RS_485_Receiver.SchDoc Page n: 5/5
 Author: Israel Sother Date: 5/19/2024



D.8.6 Current Sensor Board Layers

D.8.6.1 Top Layer



D.8.6.2 Bottom Layer

